Theoretical study of protonic conduction in Gd-doped BaCeO3 : an electrolyte for fuel cell

Jessica Hermet

THÈSE

présentée par

Jessica Hermet

pour l'obtention du

GRADE de DOCTEUR

Spécialité : Science des matériaux
Laboratoire d'accueil : Laboratoire Structures, Propriétés et Modélisation des Solides (SPMS)

Conduction protonique au sein d'un électrolyte pour pile à combustible : $BaCeO_3$ dopé Gd

Soutenue le 21 Octobre 2013

devant un jury composé de

Mme	Vannier	Rose-Noëlle	Présidente
M.	Wahnström	Göran	Rapporteur
M.	Villesuzanne	Antoine	Rapporteur
M.	Geneste	Gregory	Encadrant
M.	Dezanneau	Guilhem	Encadrant
M.	Jollet	François	Directeur de thèse

2013 – ECAP – 0058

École Centrale des Arts et Manufactures
Grand Établissement sous tutelle
du Ministère de l'Éducation Nationale
Grande Voie des Vignes
92295 Châtenay-Malabry Cedex
Tél : +33(0)1 41 13 10 00

Laboratoire Structures, Propriétés et Modélisation des Solides (SPMS)
UMR CNRS 8580, École Centrale Paris
Tél : +33(0)1 41 13 10 31
Fax : +33(0)1 47 02 80 35

Commissariat à l'énergie atomique et aux énergies alternatives (CEA)
Centre DAM-Île de France
Bruyères-le-Châtel
91297 Arpajon cedex
Tél : +33(0)1 69 26 40 00

Résumé

Cette thèse vise à étudier la diffusion protonique, et dans une moindre mesure anionique, au sein d'un matériau électrolyte pour pile à combustible $BaCeO_3$ dopé Gd, en adoptant une démarche multi-échelle.

Tout d'abord, des calculs *ab initio* ont été réalisés afin de déterminer les positions stables des défauts protoniques $OH_O^{\bullet}$ et des lacunes d'oxygène $V_O^{\bullet\bullet}$ dans le matériau. Puis, en utilisant toujours le formalisme de la théorie de la fonctionnelle de la densité, les barrières d'énergies pour les deux types de défauts entre deux positions stables ont été calculées. Enfin, ces barrières ont été utilisées dans un algorithme de Monte-Carlo cinétique afin de simuler des trajectoires de protons et de lacunes d'oxygène. Cette méthode permet d'accéder à des grandeurs macroscopiques, accessibles expérimentalement, telles que l'énergie d'activation, le coefficient de diffusion ou la mobilité, en se basant uniquement sur des données atomiques issues de simulations *ab initio*.

Ce travail montre que la surface d'énergie d'un proton dans une pérovskite orthorhombique s'avère très complexe. Bien que le gadolinium exerce une force attractive sur les protons, il se comporte seulement comme un piège peu profond. Les barrières d'énergies s'étalent sur une large gamme de valeurs et aucun mécanisme particulier n'apparait comme un processus limitant. Les sauts inter-octahédriques sont favorisés par rapport aux sauts intra-octahédriques pour le proton, et les barrières d'énergie sont systématiquement plus basse près des dopants, tandis que le phénomène contraire est observé pour les lacunes d'oxygène. L'effet d'une augmentation du taux de dopage sur le coefficient de diffusion protonique n'est finalement pas trivial.

Abstract

This thesis deals with the study of protonic diffusion, and to a lesser extent anionic, inside Gd-doped $BaCeO_3$, a possible electrolyte for fuel cell, using a multi-scale approach.

First of all, first principles calculations have been performed to determine stable positions for protonic defects $OH_O^{\bullet}$ and oxygen vacancies $V_O^{\bullet\bullet}$ in the material. Then, using the same formalism of density functional theory, energy barriers for both kinds of defects have been computed between every pair of stable positions. Finally, these barrier heights have been used in a Kinetic Monte-Carlo algorithm to simulate trajectories of protons or oxygen vacancies. This method allows to access macroscopic values, that can be measured by experiments,such as the diffusion coefficient and its activation energy, using only atomic data coming from *ab initio* simulations.

This work shows that the protonic energy surface is complex in orthorhombic perovskites. Although gadolinium attracts the protons, it constitutes only a shallow trap. There is a wide range of energy barriers and no specific mechanism appears to be rate-limiting. Some inter-octahedral protonic hoppings are favoured over intra-octahedral ones, and the barriers are systematically lowered close to dopants, while the opposite phenomenon is found for the oxygen vacancies. The effect of increasing the doping rate on the protonic diffusion coefficient is eventually non trivial.

Remerciements

First of all, I would like to thank the members of my committee for the time spent to review my thesis and for the relevance of their questions and comments: Göran Wanhström, Antoine Villesuzanne, and the president of the jury Rose-Noëlle Vannier. Since the other people I want to thank may not speak english, I will continue these acknowledgments in french.

Je tiens à remercier bien évidemment mon directeur de thèse François Jollet pour m'avoir acceptée au sein de son service pendant ces trois années.

Ma plus grande pensée va à Grégory Geneste qui m'a encadré au quotidien pendant ces trois ans avec dynamisme, rigueur et un immense optimisme. Toujours présent, toujours patient, et toujours positif, un vrai plaisir de travailler avec lui. Je lui suis aussi reconnaissante de tout ce qu'il m'a enseigné, de tous ces conseils et de toute l'aide qu'il m'a apporté.

Je remercie également Guilhem Dezanneau pour m'avoir donné goût à la recherche, et pour m'avoir aidé à bien démarrer dans ce monde, même si je ne l'ai vu que trop peu durant ces trois années.

Il y a encore tant de gens que je voudrais remercier au sein de mon laboratoire : tout d'abord François Bottin qui a fait preuve d'une grande disponibilité pour m'aider à régler des problèmes de calculs, et qui a beaucoup participé à cette thèse en proposant des idées et des solutions. Ensuite, mon chef de labo, Marc Torrent, qui lui aussi m'a aidé lors de certaines difficultés numériques.

De manière générale, beaucoup de membres du service m'ont aidé à m'intégrer dans ce petit monde :

- Nicolas, premier lien entre le monde des thésards et le monde des permanents, soucieux d'aider tout nouveau venu à se sentir bien ;
- Sandra, la merveilleuse secrétaire qui en plus d'une extrême compétence et efficacité se pare d'un certain talent quand il s'agit de discuter des petits problèmes du quotidien (choses ou personnes) ;
- Johann et Emeric pour leur sens de l'humour et leurs idées politiques ;

- Vanina, Joëlle et Agnès pour la douceur et l'intelligence féminine apportées dans ce monde de brutes ;
- Bernard pour les discussions culturelles et les promenades en voiture ;
- Noël pour son assistance et le vin ;
- Ronan pour son implication dans la vie du service, et ses discussions, même énervantes ;
- Laurent pour ses gâteaux et sa joie de vivre ;
- Emilien pour la gentillesse cachée sous les couches cynisme ;
- la flopée de stagiaires, thésards et postdoc que j'ai vu passé pendant trois ans avec une attention toute particulière aux deux adorables thésards qui m'ont accueillie, Laurent et Floriane ;
- Boris pour les compliments et les méchancetés ;
- évidemment Jordan pour son aide dans les scripts bash et les escapades à Torfou ;
- et plus généralement tout le service (pour inclure les gens que j'aurais potentiellement oubliés).

Je termine en remerciant aussi mes amies, ma famille et mon compagnon pour leur support permanent et leur optimisme, surtout sur la fin, et mes colocataires Florent et Alexandre pour leur présence et leur écoute de tous les jours.

Contents

List of Symbols and Abbreviations

Symbols

E_a	Activation energy
δ	Doping rate
μ	Mobility of the charged defects
μ_B	Bohr magneton, $\mu_B = \frac{e\hbar}{2m_e}$
ν_0	Attempt frequency or prefactor
σ	Conductivity of the charged defects
$\vec{E}_{def}$	Electric field due to charged defects, computed by Ewald summation
$\vec{E}_{ext}$	External electric field, applied to the simulation box
$\vec{E}_{loc}$	Local electric field, felt by the defects
n^i_{occ}	Occupation probability of a site of type i
E_{cut}	Cutoff Energy, controls the number of planewaves
Gd'_{Ce}	Gadolinium substituting cerium charged -1
N_k	Number of k points in the irreducible Brillouin zone.
$\mathrm{OH}^{\bullet}_{O}$	Protonic defect charged +1
$\mathrm{V}^{\bullet\bullet}_{O}$	Oxygen vacancy charged +2

Abbreviations

AFM	Antiferromagnetic
BCGO	Gd-doped barium cerate $\mathrm{BaCe}_{1-\delta}\mathrm{Gd}_{\delta}\mathrm{O}_{3-\frac{\delta}{2}}$
BCO	Barium cerate BaCeO_3

CPU	Central Processor Unit
DFPT	Density Functional Perturbative Theory
DFT	Density Functional Theory
DOS	Density of states
Exp.	Experiments
FFT	Fast Fourier Transform
FM	Ferromagnetic
GGA	Generalized Gradient Approximation
KMC	Kinetic Monte Carlo
LDA	Local Density Approximation
MEP	Minimum Energy Path
PAW	Projector augmented wave.
PCFC	Protonic Ceramic Fuel Cell
PIMC	Path Integral Monte-Carlo
PIMD	Path Integral Molecular Dynamics
inter	Inter-octahedral hopping
intra	Intra-octahedral hopping
reo	Reorientation

Latin abbreviations

e.g.	*exempli gratia*, for example
et al.	*et alii*, and others
i.e.	*id est*, in other words

Introduction

The awareness of global warming and the impending disappearance of fossil fuels have aroused a new enthusiasm for any kind of ecological and renewable energy. Neglected for a long time due to their high cost in terms of time and money, alternatives energies are getting more and more attention. Among them, fuel cells, which are not an alternative energy per se, but rather an ecological way of storage, are the topic of numerous studies.

0.1 Fuel cells

It has been nearly two centuries since the first model of fuel cell was made by William R. Grove in 1839 [1, 2], and yet the first large projects of applications are only flourishing since a decade. Apart from their use by NASA during space mission Apollo and Gemini in the sixties [3], fuel cells have been stuck at research stage for a long time. Such a duration of development can be explained by the high cost of fuel cell materials but above all by the development of other types of electric energy generators (coal, oil, nuclear). Fuel cells are now put forward due to the ecological context.

In addition to the environmental interest, fuel cells present a theoretical efficiency of 90%, much higher than the one of a Carnot process, used in thermal power station (with nuclear of fossil fuel). Even under real conditions, the electrical efficiency can reach 60%, to which we can add, depending on the application, a possible thermal efficiency through co-generation of 20-30%.

The operating principle is rather simple: the fuel cell looks like an electrochemical cell in which the electricity is generated by oxidation of a reducing fuel (usually hydrogen, sometimes methane) at the anode, and the reduction of oxygen at the cathode. Figure 0.1 shows the operating principle of such cell, on the case of a protonic conductor electrolyte (H^+).

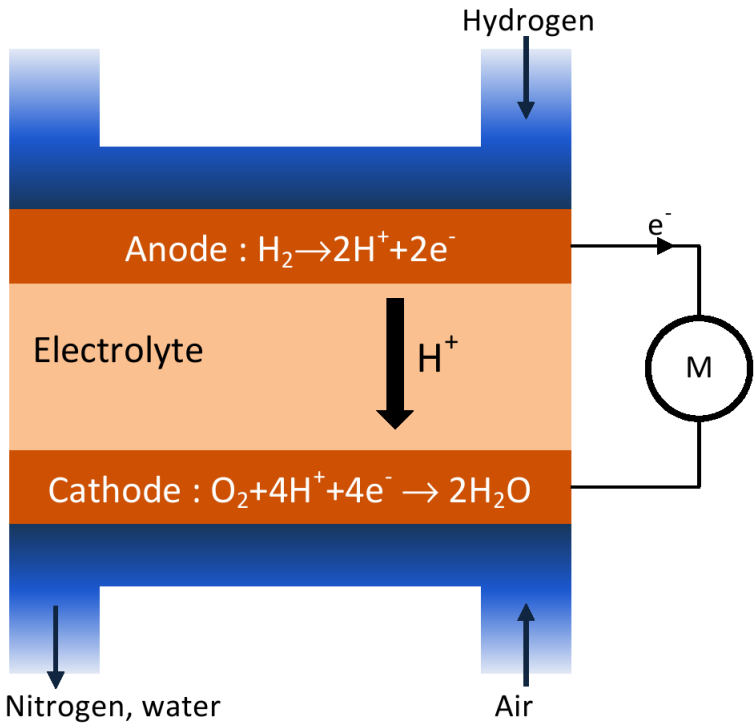

Figure 0.1: Operating principle of a protonic conducting fuel cell.

If we only look at the principle, fuel cells seem indeed ecological as the only emissions are water. But the production of hydrogen is still mostly based on fossil fuels: 95% of the current production comes from natural gas via a steam reforming process. These emissions of CO_2 and the use of fossil resources prevent fuel cells from being called « ecological and renewable ».

A proper use of these cells would be as energy storage devices rather than energy production systems, by coupling them with renewable sources such as solar or wind energy, whose electricity production is strongly dependent on weather. This is the goal of the MYRTE project(Mission hYdrogène Renouvelable pour l'inTégration au réseau Électrique [4]) in Corsica, which aims at creating solar energy on demand through fuel cells coupled with solar panels (see figure 0.2). Hence, hydrogen appears not as an energy source but rather as an energy carrier, allowing the conversion from one form of energy to another, from electrical to chemical energy, or vice versa. This principle can also be applied in residential sector: houses would benefit both from the heat and the electricity generated by fuel cells.

But stationary applications are far from being the only destiny of these cells, the transportation industry has launched their use with space shuttle, and is now starting to put out on the consumer market hybrid cars (Toyota: 2015, Mercedes: 2017).

Finally, the smallest scales are also a matter of interest: mobile technologies (from phone to computer) constitute a third possibility for applications, replacing a costly

Figure 0.2: MYRTE project in Ajaccio [5].

battery with a fuel cell. Moreover, fuel cells can store three times as much energy as a lithium-ion battery and thus have an excellent autonomy. They can handle strong temperature variations and can have a long life span [6]

For those last applications, preliminary hydrogen production is still an issue but new leads have recently appeared with the discovery of natural land-based sources of hydrogen, potentially workable, by IFPEN (French institute of oil and new energies) [7].

This wide range of applications also appears in the large variety of types of fuel cells. We can roughly distinguish two main classes:

- Protonic exchange membrane fuel cell (PEMFC) : proton conducting, low temperature (<120 °C), rather for mobiles technologies.
- Solid oxide fuel cell (SOFC) : oxygen ion conducting, high temperature (>700 °C because the activation energy of oxygen anion O^{2-} is high), rather for stationary applications.

PEMFC have the advantage of conducting protons, more mobile than oxygen, but they cannot work beyond boiling temperature of water in order not to dry out their membrane, therefore they need an expensive catalyst such as platinum for hydrogen dissociation. A new type reconciling both advantages of PEMFC and SOFC thus appears: the protonic ceramic fuel cell (PCFC). The working temperature range of PCFC goes from 300°C to 600°C.

0.2 Protonic conducting oxides

First high-temperature protonic conducting ceramics based on strontium cerate appeared in litterature thirty years ago [8]. Since then, numerous similar oxides

have also shown this protonic conducting characteristic, such as titanates, zirconates, stannates, and cerates. All of these oxides have a perovskite structure with formula ABO_3 shown on figure 0.3, in which the A-site is occupied by a divalent cation A^{2+} (Ba^{2+}, Sr^{2+}, Ca^{2+}) and the B-site, at the centre of an oxygen octahedron, is occupied by a tetravalent element B^{4+} (Ti^{4+}, Zr^{4+}, Sn^{4+}, Ce^{4+}).

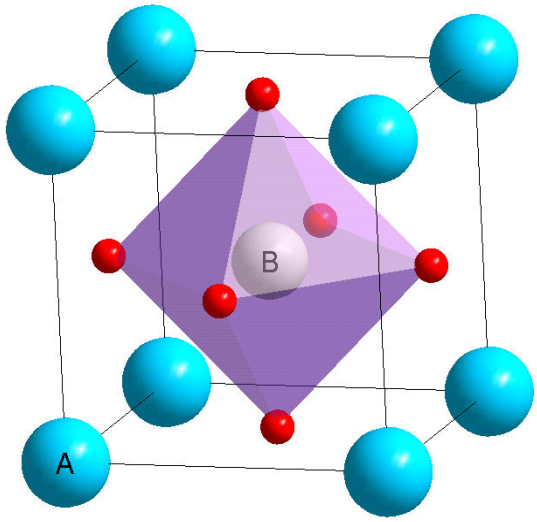

Figure 0.3: Primitive cell of an ideal (cubic) perovskite structure (5 atoms).

By substituting the tetravalent cation on B-site by a trivalent element M, a negatively charged defect is introduced, referred as M'_B using Kröger-Vink notations (a formal charge is labelled « $M^{'}$ » if negative and « $M^{\bullet}$ » if positive). Charge compensation will then promote the appearance of charged oxygen vacancies $V_O^{\bullet\bullet}$. Under wet atmosphere, these vacancies will be able to incorporate water molecules, creating protonic defects according to the following hydration reaction and enabling a possible protonic conduction:

$$H_2O + V_O^{\bullet\bullet} + O_O^x \Rightarrow 2OH_O^{\bullet}. \tag{1}$$

A very wide literature of experimental results exist on these materials, summarized many times in the papers from Kreuer and co-workers [9–11] and Norby and co-workers [12–14].

Among these materials, $BaCeO_3$ exhibit a particularly high protonic conductivity (see figure 0.4) and thus constitute a good possible electrolyte.

Numerical studies have also been performed on these protonic conducting perovskites such as BaZrO3 [15] or BaSnO3 [16], but most of these works only deal with the cubic structure. The treatment of orthorhombic structure, shared by lots of perovskites, is rather complex, that is why very few *ab initio* studies have tackled it, with the noticeable exception of the study on In-doped $CaZrO_3$ by Bilic and Gale [17].

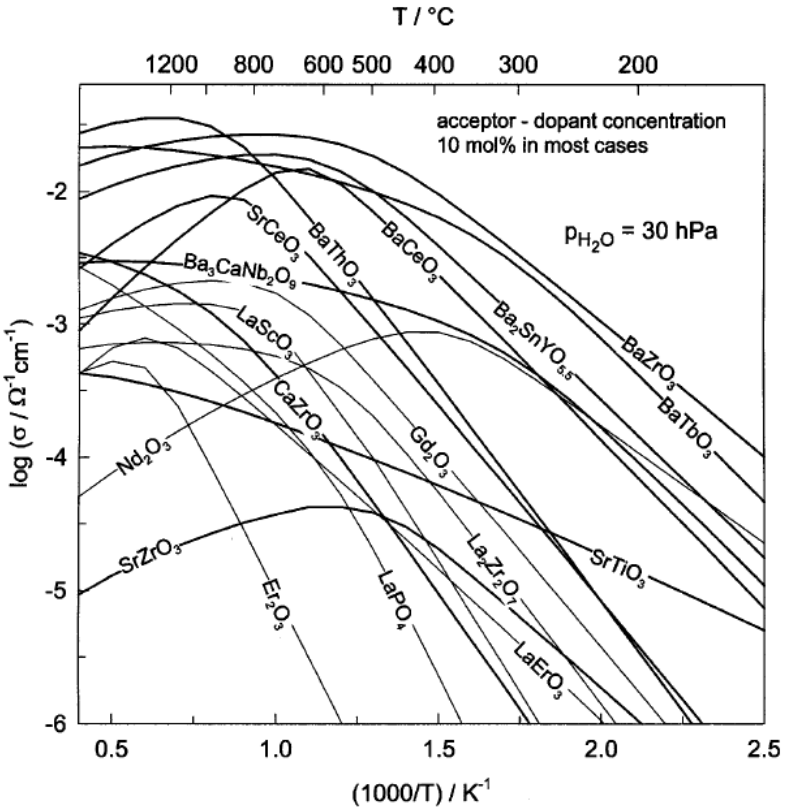

Figure 0.4: Protonic conductivity of various oxides (picture extracted from reference [9]).

Table 0.1 references some numerical studies for various perovskites, mostly made on cubic structure. The ground state structure of a perovskite is linked to its Goldschmidt tolerance factor: $t = \frac{r_A+r_O}{\sqrt{2}(r_B+r_O)}$. When the value of the tolerance factor is below 1 [18], oxygen octahedra have the tendency to tilt and distort the ideal cubic structure into an orthorhombic structure Pnma. This is the space group of the ground state of many perovskites. At high temperature, all perovskites end up in the cubic structure.

This thesis intends to present an extensive study of protonic conduction, and to a lesser extent anionic conduction, in gadolinium-doped $BaCeO_3$ in its orthorhombic structure. This material constitutes a possible electrolyte for PCFC: the presence of gadolinium atoms creates oxygen vacancies able to incorporate water molecules. The water molecules then dissociate to give rise to protonic defects. This work will examine the properties of these defects at the atomic scale (energy surface, migration barriers) and how these properties are modified under the influence of the dopant. Combining electronic structure calculations and KMC into a multiscale approach gives indications about the effect of doping on the macroscopic diffusion coefficient. The

Material	t	Structure	Reference
$SrCeO_3$	0.89	$Pnma$ (orthorhombic)	[19]
$CaZrO_3$	0.92	$Pnma$ (orthorhombic)	[20–23]
$BaCeO_3$	0.94	$Pnma$ (orthorhombic)	[19, 24, 25]
$SrZrO_3$	0.95	$Pnma$ (orthorhombic)	[20, 22, 26]
$CaTiO_3$	0.97	$Pnma$ (orthorhombic)	[23, 27, 28]
$BaZrO_3$	1.01	$Pm\bar{3}m$ (cubic)	[22, 23, 29]
$SrTiO_3$	1.01	$Pm\bar{3}m$ (cubic)	[27, 28]
$BaSnO_3$	1.03	$Pm\bar{3}m$ (cubic)	[30]
$BaTiO_3$	1.07	$P4mm$ (tetragonal)	[23]

Table 0.1: Link between structure at room temperature and Goldschmidt tolerance factor for some simple perovskites.

effects of dopant on proton conductivity are of prime importance: although dopants allow to increase the concentration of proton in $BaCeO_3$, they could significantly reduce the good properties of protonic mobility of the pure material. A good dopant should probably have a weak interaction energy with the proton in order to avoid the deterioration of the protonic conductivity.

Outline

At first, various methods used in our multi-scale approach will be explained. Then practical numerical aspects will be detailed with all hypothesis and approximations made, and preliminary studies will be presented. The third chapter will present two phenomena that can occur depending on thermodynamic conditions: oxidation and hydration, and will scrutinise the different configurations of the dry and hydrated compound. Afterwards, a fourth chapter will deal with mechanisms of protonic and anionic migration, and the computation of the associated barrier between every pair of stable positions. The diffusion and the conduction, studied by a Kinetic Monte-Carlo algorithm using results from *ab initio* calculations, will be presented in the fifth chapter, before finishing with an opening on a discussion of possible quantum effects associated to proton transport.

Chapter 1

Computational methods

In order to study protonic conduction and diffusion properties of our material, a multi-scale approach has been carried out. First, ab initio computations have been run to access stable positions and barrier energies for both protonic defect and oxygen vacancy. Then these barriers have been used in a kinetic Monte-Carlo algorithm. Finally, the quantum nature of nuclei has been taken into account with path integral molecular dynamics calculations. In this chapter, we will see the interest, the principle and the approximations of each of the methods we used.

Contents

The multi-scale approach consists of three main steps:

- *Ab initio* calculations based on Density Functional Theory (DFT) so as to get the energy landscape of stable positions for both hydrogen and oxygen vacancy in Gd-doped $BaCeO_3$ (on 80 atoms);
- Computations of energy barriers between two stable positions through String Method (also using DFT, on the same number of atoms);
- Kinetic Monte-Carlo simulations using these barriers for studying diffusion and conduction (on several thousands of atoms).

Moreover, few Path Integral Molecular Dynamics (PIMD) calculations have also been carried out on a smaller simulation box (20 atoms), still in the DFT framework, so as to treat the quantum effects on nuclei, and thus see what significance zero-point effects can have. This will be the subject of the last chapter of this thesis.

Such a multi-scale approach, based on *ab initio* results, allows to access macroscopic quantities that can be experimentally measured, such as the diffusion coefficient, the activation energy or even the protonic mobility. Indeed, all those different simulation methods can give access to different length and time scales of a system as shown in table 1.1. The given orders of magnitude are purely indicative, but may obviously vary according to the available computing power, the development of methods and algorithms, and the studied system.

Method	Time scale (s)	Length scale (m)	quantum treatment
PIMD	none [1]	10^{-10}-10^{-9}	nuclei and electrons
DFT+MD	10^{-15}-10^{-10}	10^{-10}-10^{-8}	only electrons
MD	10^{-13}-10^{-6}	10^{-10}-10^{-6}	classical treatment[2]
KMC	10^{-10}-1	10^{-9}-10^{-5}	(only electrons in our case[3])

Table 1.1: Application scales of different methods of numerical simulations. [31, 32]

1.1 Density functional theory

Purpose

Density functional theory (DFT) is a way of solving the Schrödinger equation in order to determine the ground-state electronic structure of a system.

1. Time does not have a physical meaning in PIMD.
2. However, inter-atomic potentials may be based on quantum computations.
3. The transitions rates come from DFT computations in our case. KMC simulations could also used barriers from PIMD computations and thus treat both nuclei and electrons with quantum effects.

1.1.1 Problem statement

We want to solve the Schrödinger equation for a system of N electrons and M nuclei. The Hamiltonian is

$$\hat{H} = \hat{T}_N + \hat{T}_e + \hat{V}_{ee} + \hat{V}_{eN} + \hat{V}_{NN} + \hat{V}_{app} \tag{1.1}$$

where we have (using atomic units):

$$\hat{T}_N = -\sum_{k=1}^{M} \frac{1}{2}\nabla_k^2, \text{ kinetic energy of nuclei}$$

$$\hat{T}_e = -\sum_{i=1}^{N} \frac{1}{2}\nabla_i^2, \text{ kinetic energy of electrons}$$

$$\hat{V}_{ee} = \frac{1}{2}\sum_{\substack{i,j \\ i\neq j}} \frac{1}{|\vec{r}_i - \vec{r}_j|}, \text{ interaction energy between electrons}$$

$$\hat{V}_{eN} = \sum_{i=1}^{N}\sum_{k=1}^{M} \frac{-Z_k}{|\vec{r}_i - \vec{R}_k|}, \text{ interaction energy between electrons and nuclei}$$

$$\hat{V}_{NN} = \frac{1}{2}\sum_{\substack{k,l \\ k\neq l}} \frac{Z_k Z_l}{|\vec{R}_k - \vec{R}_l|}, \text{ interaction energy between nuclei}$$

$\hat{V}_{app}$, a possible external potential applied to the system

Born-Oppenheimer approximation is used, meaning that the electrons are supposed to react instantaneously to any nuclei motion. Electrons move in a system in which nuclei are fixed : we then get $\hat{T}_N = 0$ et $\hat{V}_{NN} =$ constant and write $\hat{V}_{ext} = \hat{V}_{eN} + \hat{V}_{NN} + \hat{V}_{app}$.

Now, we have to solve the equation: $(\hat{T} + \hat{V}_{ee} + \hat{V}_{ext})\psi = E\psi$.

The main difficulty lies in the electron-electron interaction term: $\hat{V}_{ee}$. The equation will become easy to solve if the independent electron approximation could be made, that is to say replacing

$$\frac{1}{2}\sum_{\substack{i,j \\ i\neq j}} \frac{1}{|\vec{r}_i - \vec{r}_j|} \text{ with } \sum_{i=1}^{N} V_{eff}^{el}(\vec{r}_i)$$

.

The purpose of DFT is to replace $\hat{V}_{ee}$ with $\sum V_{eff}$ without any approximation.

1.1.2 Presages of DFT

1.1.2.1 The Hartree approximation

In order to simplify the electron interaction term, the Hartree approximation uses the following effective potential:

$$V_{eff,i}(\vec{r}) = \underbrace{V_{ext}(\vec{r})}_{\text{external potential}} + \underbrace{\int \frac{n(\vec{r}')}{|\vec{r}-\vec{r}'|}d^3r'}_{\text{Coulomb potential}} - \underbrace{\int \frac{n_i(\vec{r}')}{|\vec{r}-\vec{r}'|}d^3r'}_{\text{self-interaction}} \quad (1.2)$$

The resulting mono-electronic equations give a solution as a product of mono-electronic wavefunctions: $\psi(\{\vec{r}_i, s_i\}) = \prod_i^N \psi_{J_i}(\vec{r}_i, s_i)$. But these wavefunctions are not orthogonal and the solution does not respect the Pauli exclusion principle.

1.1.2.2 The Hartree-Fock equation

In order to respect the Pauli principle, the wavefunction is anti-symmetrised using a Slater determinant:

$$D(\{\vec{r}_i, s_i\}) = \frac{1}{\sqrt{N!}} \begin{vmatrix} \psi_{J_1}(\vec{r}_1, s_1) & \cdots & \psi_{J_N}(\vec{r}_1, s_1) \\ \vdots & \ddots & \vdots \\ \psi_{J_1}(\vec{r}_N, s_N) & \cdots & \psi_{J_N}(\vec{r}_N, s_N) \end{vmatrix} \quad (1.3)$$

By applying the variational method to Schrödinger equation under the constraint of orthonormalisation of mono-electronic wavefunction, the Hartree-Fock equation can be obtained [4]:

$$\left[-\frac{1}{2}\nabla^2 + V_{ext}(\vec{r}) + \int \frac{n(\vec{r}')}{|\vec{r}-\vec{r}'|}d^3r'\right]\psi_{i\sigma}(\vec{r}) - \left[\sum_j \int \frac{\psi^*_{j\sigma}(\vec{r}')\psi_{i\sigma}(\vec{r}')}{|\vec{r}-\vec{r}'|}d^3r'\right]\psi_{j\sigma}(\vec{r}) = \varepsilon_{i\sigma}\psi_{i\sigma}(\vec{r}) \quad (1.4)$$

The second term, called « Fock operator » or « Exchange potential » is a non-local potential. This term is analogous to the « self-interaction » term in the Hartree equation, but it takes into account interactions between all the electrons with parallel spin (and not only one electron with itself).

The Hartree-Fock approximation is accurate except for the fact that only one Slater determinant is considered instead of an infinite linear combination: **all that is missing is electronic correlation**.

1.1.2.3 Slater Theory

Slater [33] reinterpreted the Fock operator by multiplying and dividing it by $\psi^*_{i\sigma}(\vec{r})\psi_{i\sigma}(\vec{r})$. It then appears as a simple multiplicative operator, similar to Coulomb

4. The Hartree equation is obtained using the same method but under normalisation constraint only.

potential:

$$-\left[\sum_j \int \frac{\psi^*_{j\sigma}(\vec{r}')\psi_{i\sigma}(\vec{r}')}{|\vec{r}-\vec{r}'|}d^3r'\right]\psi_{j\sigma}(\vec{r}) \Longrightarrow \left[\int \frac{n^x_{i\sigma}(\vec{r},\vec{r}')}{|\vec{r}-\vec{r}'|}d^3r'\right]\psi_{i\sigma}(\vec{r}) \tag{1.5}$$

where $n^x_{i\sigma}(\vec{r},\vec{r}')$ is the charge distribution defined by:

$$n^x_{i\sigma}(\vec{r},\vec{r}') = -\sum_j \frac{\psi^*_{i\sigma}(\vec{r})\psi_{j\sigma}(\vec{r})\psi^*_{j\sigma}(\vec{r}')\psi_{i\sigma}(\vec{r}')}{\psi^*_{i\sigma}(\vec{r})\psi_{i\sigma}(\vec{r})} \tag{1.6}$$

But the new charge distribution depends on $\vec{r}$ and not only $\vec{r}'$ (dynamical effect), on the orbital i and the spin σ of the considered electron. It satisfies the condition $\int n^x_{i\sigma}(\vec{r},\vec{r}')d^3r' = -1$, which reminds of the « self-interaction » term of the Hartree equation.This characterises what is called the « exchange hole »: the electron in $\vec{r}$ creates a hole in the charge density when moving, he repels the other electrons.

To simplify Hartree-Fock equation, Slater made two approximations:

- In a first time, he averaged the exchange hole on all orbitals, weighting with the probability for one electron in $\vec{r}$ to be on the orbital $i\sigma$:

$$p_{i\sigma}(\vec{r}) = \frac{\psi^*_{i\sigma}(\vec{r})\psi_{i\sigma}(\vec{r})}{\sum_j \psi^*_{j\sigma}(\vec{r})\psi_{j\sigma}(\vec{r})} \tag{1.7}$$

  It gives us the equation $n^x_\sigma(\vec{r},\vec{r}') = \sum_i p_{i\sigma}(\vec{r})n^x_{i\sigma}(\vec{r},\vec{r}')$.

- Then, he went further in its simplification, making the approximation of an homogeneous electron gas (or **jellium model**):

  i/ periodic boundaries conditions are imposed (on a box with a volume V)

  ii/ wavefunctions are planewaves with a uniform density $n_\sigma = \frac{N_\sigma}{V}$

  iii/ states are occupied if $|\vec{k}| \leqslant k_{F\sigma} = (6\pi^2 n_\sigma)^{1/3}$

He computed the exchange hole with these wavefunctions to finally get a greatly simplified exchange potential:

$$V^{Slater}_\sigma(\vec{r}) = -\frac{3}{2}\left(\frac{6}{\pi}\right)^{1/3} n_\sigma^{1/3} \tag{1.8}$$

Later, Kohn and Sham [34] would make the homogeneous electron gas approximation then the variational method (the reverse of Slater approach) to find a slightly different potential:

$$V^{KS}_\sigma(\vec{r}) = -\left(\frac{6}{\pi}\right)^{1/3} n_\sigma^{1/3} \tag{1.9}$$

1.1.3 Principle

1.1.3.1 Hohenberg-Kohn theorems

Density functional theory is based on two fundamental theorems, formulated by Hohenberg and Kohn in 1964 [35] :

1) Density as a unique variable. *The ground state density is enough to determine all the properties of a system.*

In fact, the external potential $\hat{V}_{ext}(\vec{r})$ is unique for a given ground-state density $n(\vec{r})$. Since $\hat{V}_{ext}(\vec{r})$ determine the Hamiltonian, all the properties of the system can be determined in theory.

2) Variational principle. *The ground state density minimises the functional*

$$E_V[n] = F_{HK}[n] + \int V_{ext}(\vec{r})n(\vec{r})d^3r. \tag{1.10}$$

The universal functional F_{HK}, independent of external potential $V_{ext}(\vec{r})$, is defined by $F_{HK}[n] = \min_{\psi\to n}\langle\psi|\hat{T} + \hat{V}_{ee}|\psi\rangle$.

These theorems prove the existence of functionals of the density, but they do not give any information on the expression of these functionals.

1.1.3.2 Kohn-sham theory

The idea of Kohn and Sham [34] is to consider a fictitious system of N non-interacting electrons under an arbitrary potential $V_s(\vec{r})$. The Hamiltonian of such a system is separable and can thus be written as:

$$H_s = \sum_{i=1}^{N} h_s = \sum_{i=1}^{N}\left[-\frac{1}{2}\nabla^2 + V_s(\vec{r}_i)\right] \tag{1.11}$$

where h_s is the mono-electronic Hamiltonian: $h_s\psi_i = \varepsilon_i\psi_i$. From the mono-electronic wavefunctions, the ground state density can be built:

$$n(\vec{r}) = \sum_{i=1}^{N} n_i|\psi_i|^2 \text{ with } n_i \begin{cases} = 1 & \text{if } \varepsilon_i < \varepsilon_F \\ = 0 & \text{if } \varepsilon_i > \varepsilon_F \\ \in [0,1] & \text{if } \varepsilon_i = \varepsilon_F \end{cases} \tag{1.12}$$

The kinetic energy of the system of non-interacting electrons can then be defined:

$$T_s[n] = \langle\psi_s|\frac{1}{2}\sum_{i=1}^{N}\nabla_i^2|\psi_s\rangle \qquad (= F_{HK}[n] \text{ because } \hat{V}_{ee} = 0) \tag{1.13}$$

Now, let's consider a real system of electrons, with the same ground state density as the fictitious system. The exchange-correlation energy $E_{xc}[n]$ is defined by $F_{HK}[n] =$

$T_s[n] + J[n] + E_{xc}[n]$ where $T_s[n]$ is the non-interacting kinetic energy and $J[n]$ the Coulomb (or Hartree) energy:

$$J[n] = \frac{1}{2} \int \int \frac{n(\vec{r})n(\vec{r'})}{|\vec{r} - \vec{r'}|} d^3r d^3r' \tag{1.14}$$

Moreover, the universal functional $F_{HK}[n]$ is defined by :

$$F_{HK}[n] = \langle \psi_0 | \hat{T} + \hat{V}_{ee} | \psi_0 \rangle = T[n] + V_{ee}[n] \tag{1.15}$$

where ψ_0 is the ground state wavefunction.

Finally, the exchange-correlation energy has the following expression:

$$E_{xc}[n] = T[n] - T_s[n] + V_{ee}[n] - J[n] \tag{1.16}$$

The density n must minimise both the energy of the fictitious system $T_s[n] + \int V_s(\vec{r})n(\vec{r})d^3r$ and the energy of the real system $T_s[n]+J[n]+E_{xc}[n]+\int V_{ext}(\vec{r})n(\vec{r})d^3r$, we thus must have:

$$V_s(\vec{r}) = V_{ext}(\vec{r}) + \frac{\delta J}{\delta n} + \frac{\delta E_{xc}}{\delta n} \tag{1.17}$$

We can then find the same ground state density n_G for both systems. It is much easier to calculate it from the fictitious system, as it comes down to a system of mono-electronic equations:

$$\boxed{\left(-\frac{1}{2}\nabla^2 + V_{ext}(\vec{r}) + \frac{\delta J}{\delta n} + \frac{\delta E_{xc}}{\delta n} \right) \psi_i(\vec{r}) = \varepsilon_i \psi_i(\vec{r})} \tag{1.18}$$

These are the Kohn-Sham equations.

This theory is formally exact, except for the Born-Oppenheimer approximation and the non-relativistic approximation, but the (ψ_i, ε_i) do not have any physical meaning and, above all, the analytical expression of the exchange-correlation functional is unknown. Different ways of calculating it have been developed afterwards.

1.1.3.3 Exchange-correlation functional

(a) Local-density approximation (LDA)

The first idea to try to get an expression for this mysterious exchange-correlation potential is to consider a system with a slowly-varying density, so that the local approximation can be made:

$$E_{xc}^{LSD}[n] = \int \varepsilon_{xc}[n] n(\vec{r}) d^3r \tag{1.19}$$

Among local functionals, the easiest is obtained with the Jellium model, defined in section 1.1.2. We thus get the Slater exchange energy:

$$E_x^S[n] = -\frac{3}{4} \left(\frac{3}{\pi} \right)^{1/3} \int n^{4/3} d^3r \tag{1.20}$$

This exchange, when associated to the correlation of Vosko, Wilk and Nusair [36] (see appendix A.1) is commonly referred as the Local density approximation (LDA) (and can be generalised in LSDA, *Local Spin Density Approximation*, for magnetic systems by considering separately both spin densities).

The LSDA, despite its rough approximation, gives rather good results, in particular through a right compensation between the exchange energy error and the correlation energy error. Nevertheless, if we want to compute rather small quantities precisely such as barrier energies, we must use a more accurate functional.

(b) Generalized gradient approximation (GGA)

A correction depending on the gradient of the electron density is added to the exchange-correlation functional, which can hence be written as:

$$E_{xc}^{GGA}\left[n_{\uparrow}, n_{\downarrow}\right] = \int n(\vec{r})\varepsilon_x^{hom}\left[n\right] F_{xc}(n_{\uparrow}, n_{\downarrow}, \nabla n_{\uparrow}, \nabla n_{\downarrow}) d^3r \tag{1.21}$$

where F_{xc} is the enhancement factor and ε_x^{hom} the exchange energy density of an homogeneous electron gas, that is $\varepsilon_x^{hom} = -\frac{3}{4}\left(\frac{3}{\pi}\right)^{1/3} n^{1/3}$.

Among the most famous GGA functionals, we can cite the BLYP functional, which uses Becke exchange [37], and Lee-Yang-Parr correlation [38] or the Perdew, Burke and Ernzerhof (PBE) exchange-correlation functional [39]. **It is this last approximation PBE, detailed in appendix A.2, we will use in our case**, as it is a widely used functional in solid state physics.

1.2 Development of the wavefunctions

Let's put aside the purely theoretical aspects to treat a more practical question: how can we determine the wavefunctions solutions of the Kohn-Sham equations? In practice, we must choose a set of basis functions. Then, we will have to find the components of our wavefunction on this basis set, i.e. the coefficients in a linear combination of basis functions. This basis set is crucial, several options are available: plane waves, Gaussian orbitals, atomic orbitals, etc. The code we used in this thesis is a plane wave code called ABINIT [5][40].

1.2.1 Plane waves

The interest of plane waves is that they are very easy to treat mathematically and there is a systematic way to go towards the completeness of the basis by simply

5. http://www.abinit.org/

increasing the number of plane waves (it is not the case for localised orbitals such as gaussians). Besides, there are particularly well-fitted for periodic systems.

1.2.1.1 Bloch's theorem

In the case of periodic boundaries conditions, we have a periodic effective potential in Kohn-Sham equations (see equation 1.17): $V_s(\vec{r}+\vec{R}) = V_s(\vec{r})$ for all vectors $\vec{R}$ written as a linear combination of the cell vectors:

$$\vec{R} = n_1\vec{a_1} + n_2\vec{a_2} + n_3\vec{a_3}, \quad (n_1, n_2, n_3) \in \mathbb{Z}^3. \tag{1.22}$$

In the fictitious system, the wavefunction are solutions of Kohn-Sham mono-electronic equations 1.18. According to Bloch's theorem [41], we have the relation:

$$\psi_{n\vec{k}}(\vec{r}+\vec{R}) = e^{i\vec{k}\cdot\vec{R}}\psi_{n\vec{k}}(\vec{r}), \tag{1.23}$$

where n is the band index, and $\vec{k}$ is a vector of the reciprocal space, that can be restricted to the first Brillouin zone. For a given vector $\vec{k}$, there are several solutions to the monoelectronic Kohn-Sham equations corresponding to different discrete levels of energy indexed by n.

1.2.1.2 Development in plane waves

According to Fourier's theorem in one dimension, every periodical function with a period « a » can be represented by an infinite sum of complex exponentials: $\{exp(\frac{2i\pi n}{a}x)\}_{n\in\mathbb{Z}}$. The same can be applied in three dimensions, if we introduce the vectors of the reciprocal space $\vec{G}$:

$$\vec{G} = n_1\vec{b_1} + n_2\vec{b_2} + n_3\vec{b_3}, \quad (n_1, n_2, n_3) \in \mathbb{Z}^3. \tag{1.24}$$

We have the following relation between real and reciprocal vectors:

$$\vec{a_i} \cdot \vec{b_j} = 2\pi\delta_{ij}.$$

Therefore, the complex exponentials, or plane waves, $\left\{e^{i\vec{G}\cdot\vec{r}}\right\}_{(n_1,n_2,n_3)\in\mathbb{Z}^3}$ constitute a complete basis set for Kohn-Sham wavefunctions.

Practically, we cannot use an infinite number of exponentials: only wave vectors $\vec{G}$ with a modulus below a defined value G_{cut} are included. It is useful to note that this value G_{cut} can be related to a cutoff energy E_{cut} as a plane wave represents a free particle with kinetic energy $\frac{\hbar^2G^2}{2m}$. **Choosing a cutoff energy is enough to determine all the properties of the basis set**, *i.e.* all the plane waves $\exp(\vec{G}\cdot\vec{r})$ such as :

$$\frac{\hbar^2G^2}{2m} < E_{cut}. \tag{1.25}$$

1.2.2 Pseudopotential and projector augmented wave method

1.2.2.1 Frozen core approximation

In addition to the exchange-correlation approximation inherent in DFT, another approximation is often made in solid state physics: **the frozen core approximation**. This approximation consists in regarding the core electrons (to define according to the environment) as not participating in chemical bonds and reactions, as being insensitive to external variations, hence the term « frozen ». This hypothesis is related to two observations:

i/ In the vicinity of the nucleus, the wavefunction has rapid oscillations and thus needs a very fine grid to be accurately described (it means we need a lot of plane waves in our case), but the shape of the wavefunction is not very sensitive to chemical environment.

ii/ In the inter-atomic region, for external levels, the wavefunction is smoother and more regular, but also very sensitive to external variations.

This hypothesis allows to ignore the treatment of some electrons in order to be able to compute heavy elements at a lesser computational cost.

However, the core electrons implicitly appeared in the orthogonalisation of wavefunctions describing electronic states. Indeed, a wavefunction of a valence electron has to be orthogonal to all core electron wavefunctions. It constrains this wavefunction to have many nodes near the nucleus.

To avoid the touchy treatment of nodes, the potential created by the core ion (nucleus and core electrons) can be replaced by a softened effective potential, usually non local, called **pseudopotential**, associated to a nodeless pseudo-wavefunction. This effective potential corresponds to a new atom with a screened nucleus but the same valence properties. Figure 1.1 compares the shape of both the real and the pseudo wavefunctions.

The key parameter in a pseudopotential is its cutoff radius r_c beyond which both wavefunctions must be strictly equal. The larger the cutoff radius, the softer the pseudopotential and the faster the convergence (wavefunction easy to approach with few plane waves); but the less transferable the pseudopotential, that is to say less able to give good results whatever the chemical environment.

1.2.2.2 PAW method

Several methods exist to build pseudopotentials, each requiring particular conditions on the pseudo wavefunction $\tilde{\psi}$ in addition to the condition $\tilde{\psi} = \psi$ for $r > r_c$:

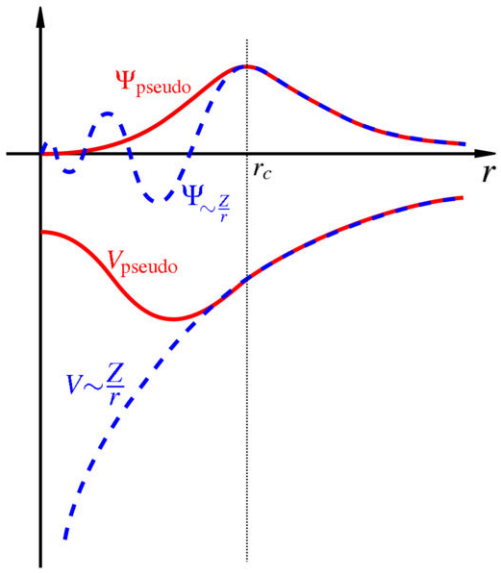

Figure 1.1: Comparison between real wavefunction (dashed blue line) – associated to the Coulomb potential of the nucleus – and the pseudo wavefunction (solid red line) – associated to the pseudopotential. Both wavefunctions are exactly identical beyond the cutoff radius ($r > r_c$).

- norm-conserving [42, 43] : $\int_0^{r_c} \tilde{\psi} = \int_0^{r_c} \psi$
- ultra-soft [44] : relax the previous condition to use a limited basis set.

More recently, **a method combining the low computational cost of pseudopotential and the accuracy of all electrons methods has been developed : the Projector Augmented Wave** (PAW) [45].

The main idea of the PAW method is to separate the wavefunction in two parts:

- below r_c, in a sphere around the nucleus, the wavefunction is developed on atomic orbitals to recover the correct oscillations (real wavefunction),
- beyond r_c, outside the sphere around the nucleus, the wavefunction is developed on plane waves (pseudo wavefunction).

Linear transformation

A pseudo wavefunction linked to the real one through a linear transformation $\mathcal{T}$ is introduced:

$$|\psi\rangle = \mathcal{T}|\tilde{\psi}\rangle. \tag{1.26}$$

We want $|\psi\rangle$ and $|\tilde{\psi}\rangle$ to be equal everywhere except in the spheres surrounding the atoms. We can decompose the linear transformation $\mathcal{T}$ as:

$$\mathcal{T} = 1 + \sum_R \hat{\mathcal{T}}_R,$$

where $\hat{\mathcal{T}}_R$ are local contributions, called PAW corrections, and only act inside the sphere enclosing atom R. This expression ensure that both wavefunction $|\psi\rangle$ and $|\tilde{\psi}\rangle$ coincide outside the atomic spheres. Inside the atomic spheres, corrections are added to the pseudo wavefunction $|\tilde{\psi}\rangle$. These corrections, $|\psi_{sphere}\rangle$ and $|\tilde{\psi}_{sphere}\rangle$, are the real and the pseudo wavefunction inside the spheres respectively.

The real wavefunction can then be expressed as:

$$|\psi\rangle = |\tilde{\psi}\rangle + |\psi_{sphere}\rangle - |\tilde{\psi}_{sphere}\rangle \tag{1.27}$$

The next step is to expand the wavefunction inside the sphere on partial waves: $|\psi_{sphere}\rangle = \sum_i c_i|\phi_i\rangle$. The $|\phi_i\rangle$ are atomic orbitals, built from the true atomic potential. The index i refers to the atomic site R, the angular momentum (l,m) and an additional number n to differentiate several partial waves with the same angular momentum and localised on the same atom. For the pseudo wavefunction, the $|\tilde{\phi}_i\rangle$ are built from a pseudopotential and must satisfy: $|\phi_i\rangle = \mathcal{T}|\tilde{\phi}_i\rangle$. This implies identical coefficients c_i in both expansions.

The total wavefunction can thus be expressed as:

$$|\psi\rangle = |\tilde{\psi}\rangle + \sum_i c_i(|\phi_i\rangle - |\tilde{\phi}_i\rangle). \tag{1.28}$$

Equation 1.28, represented in figure 1.2, is the main equation of PAW method.

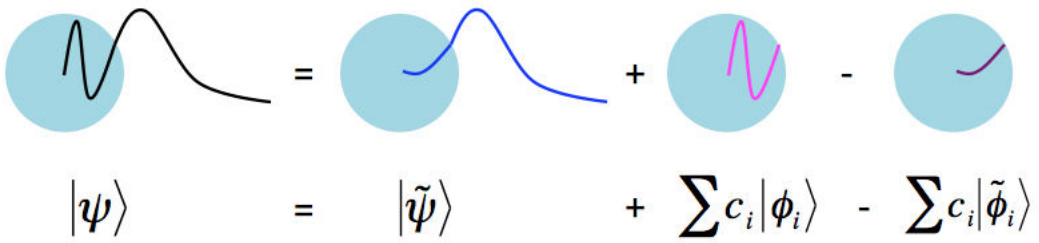

Figure 1.2: PAW transformation.

Once the linear transformation $\mathcal{T}$ is known, physical properties can be obtained. Indeed, to compute the expectation value $\langle A\rangle = \langle\psi|A|\psi\rangle$ of an observable A, we introduce a pseudo-operator $\tilde{A} = \mathcal{T}^\dagger A\mathcal{T}$ so that:

$$\langle A\rangle = \langle\tilde{\psi}|\tilde{A}|\tilde{\psi}\rangle.$$

If the frozen core approximation is right, and the basis set of projectors is complete, then the PAW method has the **same accuracy as an all-electron method**. This is the method we will use for all our calculations, unless specified otherwise. Since this method is not really a pseudopotential method but instead requires the knowledge of the coefficients $\{c_i\}$ for each atom, we will refer to the input file containing all the needed informations as « atomic data » and not « pseudopotential ».

1.3 String Method

Purpose

To find the energy variation along the reaction coordinate of a chemical reaction (protonic or oxygen transfer in our case), we need the energy of both initial and final stable positions, and the energy of the transition state, also called saddle state. This name comes from the shape of the surface in the vicinity of the transition state: along the reaction path, it is an energy maximum, but it is a minimum in the subspace perpendicular to the path (see figure 1.3). Several methods are available to localise the transition state of a chemical reaction through theoretical calculations. These methods often look for the minimum energy path (MEP). It is the case for the Nudge Elastic Band (NEB) or for the String Method. We will use the latter and explain it hereafter.

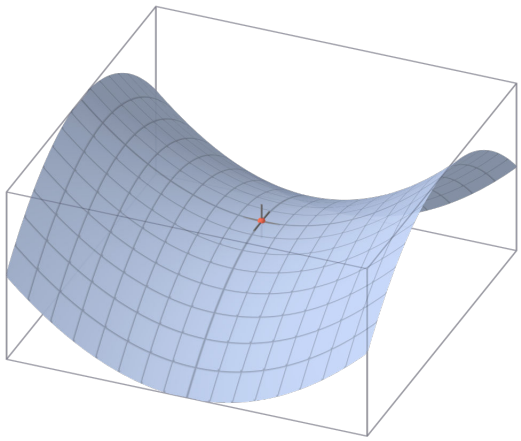

Figure 1.3: The red dot corresponds to the saddle point.

1.3.1 Principle

The String method allows the determination of the minimum energy path between two positions through an iterative algorithm [46]. The path – we can take a simple straight line at the beginning – is discretised in equidistant configurations called « images ». The choice of the number of images is crucial to get an accurate barrier energy. At each iteration, a two-step procedure is applied:

i/ Displacement of the images according to atomic forces perpendicular to the path.

ii/ Re-parametrisation in order to keep all images equidistant (in terms of length or of energy).

The algorithm stops when a convergence criterion is reached: for instance, when the total energy difference averaged over all images between one iteration and the previous one is below 10^{-5} Ha.

1.3.2 Simplified String method

The method we actually used is the Simplified String Method, which differs from the String Method by simply taking the total forces in the first step, instead of their projection. This method is faster and even more efficient that the String Method [47]. Figure 1.4 sums up the algorithm.

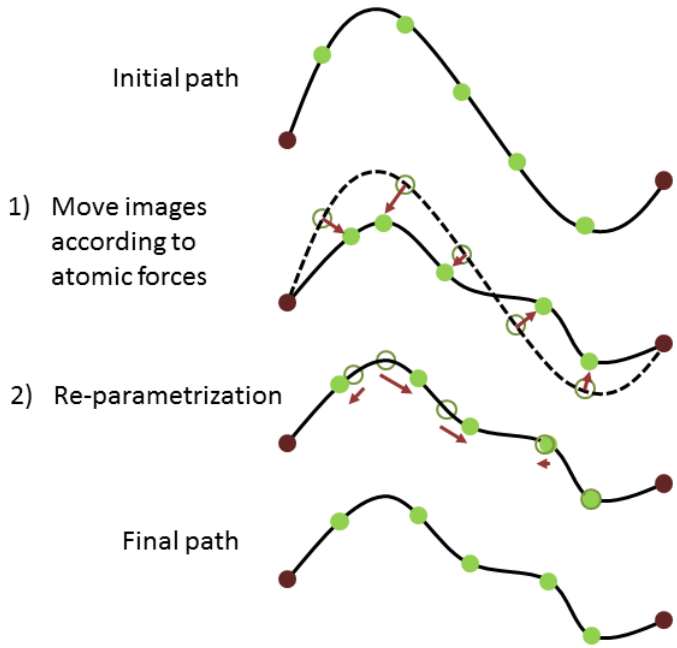

Figure 1.4: Principle of the simplified string method.

1.4 Kinetic Monte-Carlo

Purpose

The kinetic Monte-Carlo (KMC) method is a numerical stochastic method to simulate the time evolution of a system in which every process rate is known, under or out of thermodynamic equilibrium. Its main interest is to be able to treat simultaneously events with very different probabilities, and hence to study rare events [48] (which are problematic in molecular dynamics). KMC can simulate long trajectories – typically a few microseconds (or more depending on the temperature, the type of processes, etc.) – while (*ab initio*) molecular dynamics can hardly simulate

longer than a few picoseconds. It has been used to study bulk diffusion [49], reactivity at surfaces [50], crystal growth [51], etc.

1.4.1 Principle

The kinetic Monte-Carlo method follows the relatively simple algorithm (« residence-time algorithm »):

i/ Set the time t=0.

ii/ List all possible processes $i = 1 \dots n$ and their rates ν_i in the system.

iii/ Calculate the cumulative function $R_i = \sum_{j=1}^{i} \nu_i$ for every $i \in [1 : N]$. Let's set $R = R_N$.

iv/ Generate a random number $\rho_1 \in [0 : 1]$

v/ Find the event i such that $R_{i-1} < \rho_1 R < R_i$ and fulfil it.

vi/ Generate another random number $\rho_2 \in [0 : 1]$

vii/ Increment simulation time $t = t + \Delta t$ where $\Delta t = -\ln(\rho_2)/R$

viii/ Return to step ii and iterate until the desired number of steps is reached.

At each iteration, the probability to chose an event is proportional to its transition rate (see steps iii–v).

1.4.2 Events probability

1.4.2.1 Master equation

If $P_A(t)$ is the probability to find the system in the microscopic state A at time t, the time evolution of this probability $P_A(t)$ is governed by the **master equation** [48]:

$$\boxed{\frac{dP_A(t)}{dt} = -\sum_{B \neq A} \nu_{AB} P_A(t) + \sum_{B \neq A} \nu_{BA} P_B(t),} \tag{1.29}$$

where ν_{AB} is the probability per time unit (rate constant) to go from state A to state B.

Taking the master equation 1.29 at equilibrium leads to the condition for every state A:

$$\sum_{B \neq A} [\nu_{BA} P_B^{\infty} - \nu_{AB} P_A^{\infty}] = 0, \tag{1.30}$$

where P_A^{∞} is the time-independent probability, i.e. the solution of the master equation at equilibrium.

This equation simply states that the sum of all transitions into a given state A is equal to the sum of all transition out of this given state A.

In fact, one can show that the condition of equation 1.30 implies a stricter relation called the **detailed balance principle**, valid for an isolated system or a system in contact with a thermostat [52]:

$$\nu_{BA} P_B^{\infty} - \nu_{AB} P_A^{\infty} = 0 \tag{1.31}$$

It is possible to prove that **the canonical distribution is the equilibrium solution of the master equation** for a system in contact with a thermostat. This canonical distribution is given by:

$$P_A^{\infty} = \frac{1}{Z} e^{-E_A/k_B T}. \tag{1.32}$$

From equations 1.31 and 1.32, we get the following relation between both rate constants ν_{ij} and ν_{ji}:

$$\frac{\nu_{AB}}{\nu_{BA}} = \exp\left(-\frac{E_B - E_A}{k_B T}\right) \tag{1.33}$$

1.4.2.2 Transition state theory

The algorithm requires only the probability rates $\{\nu_{AB}\}$ associated to each elementary process.

The most commonly used approach to get the values of these rates comes from the transition state theory [53–55] :

$$\nu_{AB} = \nu_0 e^{-\frac{\Delta E_{AB}}{k_B T}} \tag{1.34}$$

where ΔE is the migration barrier between both initial and final positions, and the general expression of ν_0 is given, using the harmonic approximation, by [48] :

$$\nu_0 = \frac{k_B T}{h} \frac{Z\ddagger}{Z} \tag{1.35}$$

where $Z\ddagger$ is the partition function at the transition state and Z the partition function at the initial state A. The issue of the prefactor ν_0 will be discussed in section 5.2.3.

Using equations 1.33 and 1.34 for a transition between state A and state B (see notations in figure 1.5), provided that ν_0 is identical for both rate constants ν_{AB} and ν_{BA}, we must have:

$$\begin{array}{ccccc} \frac{\nu_{AB}}{\nu_{BA}} & = & \exp\left(-\frac{E_B - E_A}{k_B T}\right) & = & \exp\left(-\frac{\Delta E_{AB} - \Delta E_{BA}}{k_B T}\right) \\ & \Rightarrow & E_B - E_A & = & \Delta E_{AB} - \Delta E_{BA} \end{array} \tag{1.36}$$

In fact, this last equation is obvious if we look at the physical quantities behind: it simply states that the saddle point has the same energy whether the particle comes from initial state A or initial state B:

$$E_A + \Delta E_{AB} = E_B + \Delta E_{BA} \; (= \text{transition state energy}) \tag{1.37}$$

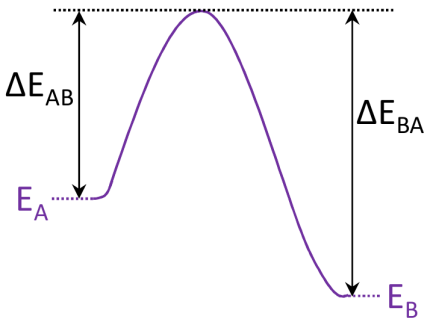

Figure 1.5: Energy barrier between two stables positions A and B.

It is necessary to have this strict equality 1.37 to recover the canonical distribution expected in kinetic Monte Carlo simulations. In section 5.1.2, we will make sure that the set of energy barriers ΔE_{AB} fulfils this condition.

1.5 Path Integral Molecular Dynamics

Purpose

Path Integral Molecular Dynamics (PIMD) aims at taking into account the quantum nature of nuclei, left out in standard *ab initio* molecular dynamics, by treating an equivalent system of an infinite number of classical particles.

1.5.1 History

Path Integral Molecular Dynamics (PIMD) or Monte-Carlo (PIMC) are based on a 30-years old idea [56] and use Feynman path integrals [57, 58]. But it has become practical since only a few years, with the advent of super-computers. In 1996, the algorithms of path integral coupled with Car-Parrinello molecular dynamics [59] or Born-Oppenheimer dynamics [60] have been detailed and discussed. The applications are still rare and restricted to small systems of light atoms (such as the superfluid transition of liquid helium at 2.17 K[61], or hydrogen bonding in water [62, 63]) because of its prohibitive cost. Nevertheless, a first paper of Zhang et al. [64] uses this method on 5 atoms to simulate proton motions inside the perovskite $BaZrO_3$.

1.5.2 Principle

In this section, the basic principles of *ab initio* PIMD formulated by Marx and Parrinello in 1996 [60] will be presented. Here is a demonstration in the simple case of a particle in a one-dimensional potential.

The starting point is the canonical density operator $\hat{\rho} = e^{-\beta\hat{H}} = e^{-\beta(\hat{T}+\hat{V})}$. The partition function can then be written as the trace of this operator in the position representation:

$$Z = Tr(e^{-\beta\hat{H}}) = \int dx \langle x|\hat{\rho}|x\rangle$$

We can then use the Trotter formula [65] :

$$e^{\alpha(A+B)} = \lim_{P\to\infty} \left[e^{\frac{\alpha}{2P}B} e^{\frac{\alpha}{P}A} e^{\frac{\alpha}{2P}B}\right]^P$$

We apply this theorem to $\hat{\rho}$ and get:

$$\langle x|e^{-\beta(T+V)}|x\rangle = \lim_{P\to\infty} \langle x| \left(e^{-\frac{\beta}{2P}\hat{V}} e^{-\frac{\beta}{P}\hat{T}} e^{-\frac{\beta}{2P}\hat{V}}\right)^P |x\rangle$$

Let $\Omega = e^{-\frac{\beta}{2P}\hat{V}} e^{-\frac{\beta}{P}\hat{T}} e^{-\frac{\beta}{2P}\hat{V}}$. The partition function can be written as:

$$Z = \lim_{P\to\infty} \int dx \langle x|\Omega^P|x\rangle$$

The insertion (P-1) times of the completeness relation $I = \int |x\rangle\langle x| dx$ leads to:

$$Z = \lim_{P\to\infty} \int dx_1 dx_2 \dots dx_P \langle x_1|\Omega|x_2\rangle\langle x_2|\Omega|x_3\rangle \dots \langle x_P|\Omega|x_1\rangle \tag{1.38}$$

We now need to compute:

$$\langle x_i|\Omega|x_{i+1}\rangle = \langle x_i|e^{-\frac{\beta}{2P}\hat{V}} e^{-\frac{\beta}{P}\hat{T}} e^{-\frac{\beta}{2P}\hat{V}}|x_{i+1}\rangle. \tag{1.39}$$

1.5.2.1 Potential energy

The potential energy operator action is easy because the eigenvectors of the position operator $|x\rangle$ are the eigenvectors of $\hat{V}$ (hence of $e^{-\frac{\beta}{2P}\hat{V}}$) so that: $e^{-\frac{\beta}{2P}\hat{V}}|x\rangle = e^{-\frac{\beta}{2P}V(x)}|x\rangle$. The previous expression 1.39 simply becomes:

$$\langle x_i|e^{-\frac{\beta}{2P}\hat{V}} e^{-\frac{\beta}{P}\hat{T}} e^{-\frac{\beta}{2P}\hat{V}}|x_{i+1}\rangle = e^{-\frac{\beta}{2P}(V(x_i)+V(x_{i+1}))}\langle x_i|e^{-\frac{\beta}{P}\hat{T}}|x_{i+1}\rangle. \tag{1.40}$$

The only thing left to determine is the kinetic energy term $\langle x_i|e^{-\frac{\beta}{P}\hat{T}}|x_{i+1}\rangle$.

1.5.2.2 Kinetic energy

Once again, we insert the completeness relation, but on eigenvectors of the impulsion operator $I = \int dk|k\rangle\langle k|$:

$$\langle x_i|e^{\frac{-\beta}{P}\hat{T}}|x_{i+1}\rangle = \int dk \langle x_i|k\rangle\langle k|e^{\frac{-\beta}{P}\hat{T}}|x_{i+1}\rangle.$$

$\hat{T}$ is a hermitian operator whose eigenvectors and eigenvalues are $|k\rangle$ and $\frac{\hbar^2k^2}{2m}$ respectively. Moreover, we have the relation $\langle x|k\rangle = \frac{1}{\sqrt{2\pi}}e^{ikx}$. We thus have:

$$\langle x_i|e^{-\frac{\beta}{P}\hat{T}}|x_{i+1}\rangle = \int e^{-\frac{\beta\hbar^2k^2}{2mP}}\langle x_i|k\rangle\langle k|x_{i+1}\rangle dk = \frac{1}{2\pi}\int e^{-\frac{\beta\hbar^2k^2}{2mP}}e^{ik(x_i-x_{i+1})}dk.$$

The substitution $u = \sqrt{\frac{\beta}{2mP}}\hbar k - \frac{i}{2\hbar}\sqrt{\frac{2mP}{\beta}}(x_i - x_{i+1})$, so that $du = \sqrt{\frac{\beta\hbar^2}{2mP}}dk$, finally gives:

$$\langle x|e^{\frac{-\beta}{P}T}|x'\rangle = \frac{1}{2\pi}e^{-\frac{mP}{2\beta\hbar^2}(x-x')^2} \times \sqrt{\frac{2mP}{\beta\hbar^2}} \times \int e^{-u^2}du = \left(\frac{mP}{2\pi\beta\hbar}\right)^{1/2} e^{-\frac{mP}{2\beta\hbar^2}(x-x')^2} \tag{1.41}$$

1.5.2.3 Partition function

Using the three equations 1.38, 1.40 and 1.41, the partition function is finally written:

$$\boxed{Z = \lim_{P\to\infty}\left(\frac{mP}{2\pi\beta\hbar}\right)^{P/2}\int dx_1\dots dx_P\ e^{-\frac{\beta}{P}\sum V(x_i)}e^{-\frac{mP}{2\beta\hbar^2}\sum(x_i-x_{i+1})^2}} \tag{1.42}$$

where $x_{P+1} = x_1$.

If we fix P, equation 1.42 appears as the partition function of a classical system of P particles (beads or imaginary time slices) connected by springs with a force constant $\frac{mk_B^2T^2P}{\hbar^2}$ and subjected to an interaction potential $\frac{V}{P}$ inside each slice. The key parameter to get the correct quantum partition function is thus the Trotter number P.

1.5.3 Limitations

Path Integral molecular dynamics approach possesses some limitations though:

- it is only valid for distinguishable particles, (possibly bosons in PIMC);
- practically, it only works for « not too low » temperatures (otherwise, P must tend to infinity);
- when P tends to infinity, the system behaves as a pure harmonic oscillator leading to the necessity to use specific thermostats to recover the ergodicity (risk of non-ergodic trajectories). In this work, a Langevin thermostat will be used to ensure ergodicity.

We presented here the theory behind density functional theory, kinetic Monte-Carlo and path integral molecular dynamics. The next chapter will explain some parameters needed for density functional theory. Then, in the following chapters, all these methods will be used to access thermodynamics, structural, diffusion and conduction properties.

Chapter 2

Numerical methodology

After describing all the theory behind the method we used, the DFT methodology – parameters, assumptions, choices – will be detailed.

This chapter will first present preliminary results on elements, binary compounds and pure barium cerate, and then describe how we built our supercell and how we chose to treat the defects.

Contents

2.1 Preliminary study – test of PAW atomic data

All DFT computations have been made with the periodic code ABINIT in the PAW framework. This code uses planewaves as the basis set for wavefunctions. We used the exchange-correlation functional GGA-PBE [39], but we also performed some tests with a LDA functional. The use of a periodic code with planewaves implies two parameters of convergence:

- the number of k-points to appropriately sample the Brillouin zone (for a non-periodic system, one k-point is enough).
- the cutoff energy E_{cut} which controls the number of planewaves (see section 1.2.1.2 and equation 1.25). The larger E_{cut}, the better converged the calculation.

As described in the section 1.2.2, the core electrons are considered as frozen, however the semi-core electrons of metals are explicitly treated using the PAW method. Table 2.1 shows the explicitly treated electrons for each studied element.

Element	Structure (number of treated electrons)
H	$1s^1$ (1)
O	$2s^2$ $2p^4$ (6)
Ba	$5s^2$ $5p^6$ $6s^2$ (10)
Ce	$5s^2$ $5p^6$ $4f^1$ $5d^1$ $6s^2$ (12)
Gd	$5s^2$ $5p^6$ $4f^7$ $5d^1$ $6s^2$ (18)

Table 2.1: Explicitly treated electrons in our simulations for each considered element.

The atomic data associated to these electronic structures have been generated with the code AtomPAW [66]. They have to be tested on pure materials and binary compounds to check their validity and define the suitable convergence parameters, before using them in more complex simulations with five different chemical elements (Gd-doped $BaCeO_3$ with a protonic defect).

This preliminary study has two goals:

- testing the numerical scheme on the simple systems (molecules, crystals) that will be used in the following as references for the calculation of various energies
- determining the numerical parameters (E_{cut} and k-point sampling) ensuring a very good convergence of the results, according to a chosen criterion.

We will carefully detail the methodology to choose atomic data in this section. The values of parameters are usually given in atomic units, i.e. length in bohr radius $1\,a_0$=0.529 Å and energy in Hartree 1 Ha=4.360×10^{-18} J=27.211 eV. The criterion that will lead us in this preliminary study is **an accuracy of 10^{-3} Ha (0.03 eV) per atom or formula unit on the total energy**. However, it is well known in

plane-wave DFT that an accuracy of 0.03 eV on total energies induces a much better accuracy on the total energy differences (bond energies, cohesive energies, formation energies, etc.). Therefore, **the accuracy on physical quantities, with the same parameters, will usually be much better than** 0.01 eV.

2.1.1 Light elements – Molecules

We started with the light elements O and H to see if we recover correctly the bond length and the binding energies of molecules O_2, H_2 et H_2O. Special attention is to be paid to this last molecule H_2O since this is the molecule that will incorporate inside our material, and the O-H bond will be fundamental in our study.

In order to choose perfectly appropriate atomic data, several cutoff radii have been tested:

- for oxygen: $r_{O1} = 1.1\ a_0$, $r_{O2} = 1.4\ a_0$, $r_{O3} = 1.5\ a_0$,
- for hydrogen : $r_{H1} = 0.8\ a_0$, $r_{H2} = 1.1\ a_0$.

For oxygen, we first tested a short (r_{O1}) and a large cutoff radius (r_{O3}), the intermediate cutoff radius (r_{O2}) was introduced afterwards, for reasons explained below. A large radius is usually said to be « soft » while a short radius is said « hard », as it requires more computations and gives a better accuracy. The cutoff radius is crucial for light element since their bond length is usually rather short. We must be careful to choose a cutoff radius short enough to prevent the overlap between PAW spheres, but not too short to get a rather low cutoff energy and have a reasonable computational cost.

Table 2.2 shows the typical overlap induced by the different PAW atomic data for H_2 and O_2 molecules, and for the usual O–H bond. By default, ABINIT tolerates an overlap of 5% between two PAW spheres.

Molecules	r_c	Overlap on length (Å)	Overlap on volume (%)
H_2	r_{H1}	0.1 Å	2%
(0.74 Å)	r_{H2}	0.4 Å	15%
O_2	r_{O1}	0.0 Å	0%
(1.21 Å)	r_{O2}	0.3 Å	5%
	r_{O3}	0.4 Å	8%
O–H bond	r_{H1} & r_{O2}	0.2 Å	11%
(0.96 Å)	r_{H2} & r_{O2}	0.4 Å	15%

Table 2.2: Overlap on length and volume for H_2, O_2 and O–H bond, according to different PAW atomic data.

Except for the atomic data of O with the shortest cutoff radius, overlaps of PAW spheres are unavoidable to keep the atomic data rather soft. Our final choice of

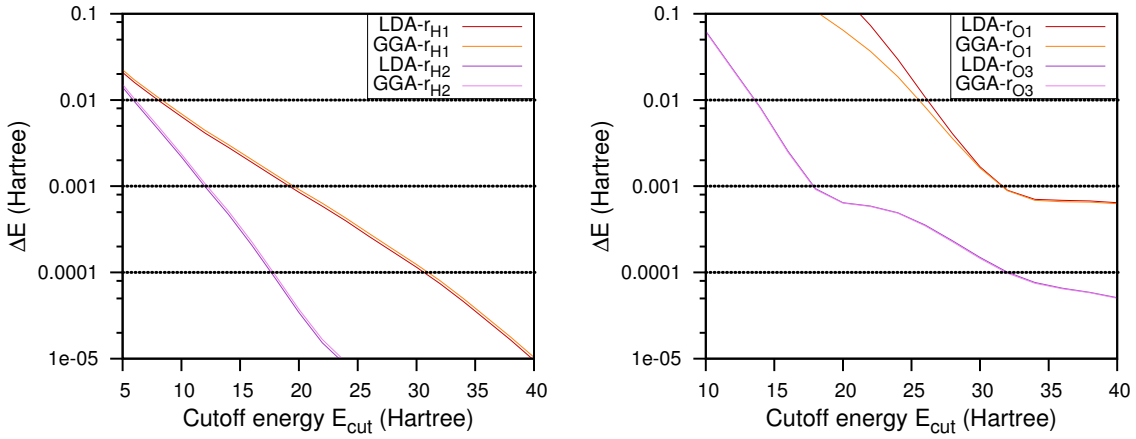

(a) Hydrogen

(b) Oxygen

Figure 2.1: Convergence curves of several atomic data for hydrogen and oxygen (free atoms).

atomic data will be a compromise with a small amount of overlap on the O–H bond while keeping a very good (and perfectly controlled) accuracy on the bond energy.

We also tested a LDA functional for the exchange-correlation. For such non-periodic system, we do not have to test the number of k-points, the sole parameter to converge is E_{cut}, providing the simulation box is large enough to prevent interactions between a molecule and its image in a different cell. We tried several values of cell parameters : 10 a_0, 20 a_0 and 30 a_0. It appeared that for both oxygen and hydrogen, 20 a_0 was enough to get an accuracy on total energy better than 10^{-3} Ha per atom, but 10 a_0 was too small. We then run several simulations with E_{cut} varying from 4 to 60 Ha with a step of 2 Ha.

Figure 2.1 shows the difference in total energy found between $\mathrm{E}_{tot}(E_{cut})$ and $\mathrm{E}_{tot}(E_{cut-max})$, with $E_{cut-max} = 62$ Ha, for the previously introduced atomic data for hydrogen and oxygen free atoms (except r_{O2}) for both LDA and GGA exchange-correlation functional.

These curves allow to determine the right plane-wave cutoff energy associated to each cutoff radius (according to the criterion previously defined). For instance, we found a cutoff energy of 20 Ha for the hard radius of hydrogen, and of 12 Ha for the soft one. For oxygen, the difference is even stronger, and a cutoff of 32 Ha is found for r_{O1} while the soft radius allows the system to be converged with $\mathrm{E}_{cut} = 16$ Ha. As expected, hard atomic data, with a short cutoff radius, require a larger cutoff energy than soft one, meaning a higher computational cost.

One should keep in mind that **the cutoff energy depends on the chemical environment**, and so the cutoff energy ensuring a given accuracy in an atomic system may be different in a bulk. Indeed, if a right cutoff energy for r_{O3} in atomic

system is found to be E_{cut} = 16 Ha, the oxygen molecule needs a cutoff energy of 26 Ha to get an error on the total energy below 10^{-3} Hartree per atom. This difference implies using the higher cutoff of 26 Ha to get the correct binding energy.

Finally, we can see that there is no noticeable difference in convergence for LDA or GGA, the difference will appear on the values of physical properties.

Once the cutoff energies have been determined, we have to look at physical properties found for each cutoff radius with the right E_{cut}. Table 2.3 summarises the results obtained for a cutoff energy so that the accuracy on the total energy is below 10^{-3} Hartree.

Molecules	E_{xc}	r_{Hc}	r_{Oc}	E_{cut} (Ha)	d_{eq} (Å)		E_{bind}
					H-H	O-H	(eV/molec.)
H_2	LDA	r_{H1}	–	20	0.770		-4.878
	LDA	r_{H2}	–	12	0.771		-4.849
	GGA	r_{H1}	–	20	0.756		-4.506
	GGA	r_{H2}	–	14	0.757		-4.481
	LDA [45]			15	0.773		-4.62
	GGA [67]			10	0.750		-4.58
	GGA [68]			13	0.750		-4.54
	Exp. [69]				0.741		-4.75
O_2	LDA	–	r_{O1}	32	1.209		-7.494
	LDA	–	r_{O3}	18	1.242		-7.066
	GGA	–	r_{O1}	32	1.222		-6.195
	GGA	–	r_{O2}	26	1.228		-6.262
	GGA	–	r_{O3}	26	1.249		-6.076
	LDA [45]			15	1.228		-7.33
	GGA [70]			37	–		-6.214
	Exp. [70]				–		-5.116
H_2O	LDA	r_{H1}	r_{O1}	32	1.543	0.973	-11.533
	LDA	r_{H1}	r_{O3}	28	1.555	0.977	-11.458
	LDA	r_{H2}	r_{O1}	32	1.549	0.978	-11.452
	LDA	r_{H2}	r_{O3}	26	1.562	0.983	-11.376
	GGA	r_{H1}	r_{O1}	32	1.533	0.972	-10.161
	GGA	r_{H1}	r_{O2}	26	1.539	0.974	-10.160
	GGA	r_{H1}	r_{O3}	28	1.545	0.977	-10.163
	GGA	r_{H2}	r_{O1}	32	1.538	0.979	-10.020
	GGA	r_{H2}	r_{O3}	26	1.552	0.984	-10.026
	GGA [70]			37	–	–	-10.134
	Exp. [70]				–	–	-10.104

Table 2.3: Binding energy and bond length for O_2, H_2 and H_2O from our calculations compared to other PAW calculations and experience. The O_2 molecule is computed in a spin-polarised scheme, its calculated magnetic moment is $2\mu_B$.

In this table, the difference between LDA and GGA clearly appears. We can see

that GGA gives better results both on the bond length and on the binding energies, as usually observed. This observation comforts us in the choice of GGA-PBE functional. To see whether the atomic data give good results, we can compare our values with previous ones computed in the same formalism: PAW method and GGA functional.

First of all, we see that both atomic data of H give the same results ($E_{bind} \approx -4.50 \pm 0.02$ eV and $d_{H--H} = 0.756 \pm 0.001$ Å in GGA), in excellent agreement with other GGA-PAW calculations [67, 68]. As the cutoff energy is low (compared to the cutoff for other elements such as oxygen) even for the hard atomic data, **we choose the hardest one, r_{H1}**, to get the best results.

For O_2, it is more complicated. We can see from the convergence curves of figure 2.1(b), that both atomic data are not really satisfactory. There is a plateau just below the 10^{-3} line meaning that a slight change in ΔE could result in a drastic increase of the cutoff energy: this is the case for r_{O3} where we need $E_{cut} = 26\ Ha$ for a molecule when $E_{cut} = 16\ Ha$ was enough for an atom. Furthermore, these atomic data tend to significantly overestimate the bond length and underestimate the binding energy, as shown in table 2.3. This is clearly due to the large overlap of PAW spheres which is forbidden by PAW formalism. On the other hand, the hard cutoff radius r_{O1} requires a very high cutoff energy and will have a great computational cost. This is why **we introduced an intermediate radius r_{O2} which gives almost as good results as the hard one, but needs a cutoff energy as low as the soft one. These are the atomic data we used in this thesis**, except for some tests with the hard one to confirm the validity of our results. These atomic data r_{O2} allow to treat the O_2 molecule at a reasonable cutoff energy and keep a very good binding energy of -6.26 eV (versus -6.20 eV for r_{O1}, *i.e.* less than 1% of error). The accuracy is even better on the binding energy of H_2O (-10.160 eV versus -10.161 eV, less than 0.01% of error). Finally, the overlap between PAW spheres existing in O_2 with r_{O2} completely disappears in the bulk oxides, where the interatomic distances are much larger than in O_2, which fully justifies the use of r_{O2}.

In light violet in table 2.3, we summarize the results obtained on H_2, O_2 and H_2O with the atomic data chosen in this thesis.

2.1.2 Metals and binary oxides

For metallic elements, we did not try several cutoff radii but we made sure the atomic data were accurate by looking at equilibrium volume, bulk modulus and cohesive energy for pure metals first, and for their oxides in a second time. The PAW radii are $2.8\,a_0$ for Ba, $2.5\,a_0$ for Ce and $2.5\,a_0$ for Gd, they ensure that there is no overlap at all between PAW spheres. Atomic data of cerium and gadolinium are

taken from the work of Amadon et al. [71]. We thus simulate the following materials in their most stable structure:

- Barium: body-centred cubic; BaO: rock salt;
- Cerium: face centred cubic; CeO_2: fluorite [1];
- Gadolinium: hexagonal (antiferro and ferromagnetic); Gd_2O_3: bixbyite.

The cerium being in the oxidation state 4+, its electronic structure loses four electrons so that f-orbitals are empty $5s^2\ 5p^6\ 4f^0\ 5d^0\ 6s^0$. Therefore we do not need to use a special treatment for strongly correlated electrons.

Here, we also have to test the k-point sampling to converge our results. As we have periodic materials, the electronic density is obtained by an integration in the reciprocal space. To get the good value we thus have to increase the number of k-points until the physical properties are converged.

Another parameter we need to converge for metallic compounds is the smearing temperature, it corresponds to the electronic temperature and so allows electrons to move from one orbital to another. It should be small as we want to find the ground state configuration. We will not discuss this parameter though, as it is of importance only for metallic elements, and our calculations will mainly focus on insulating oxides.

We present a convergence study for both cutoff energy and k-point sampling in the following.

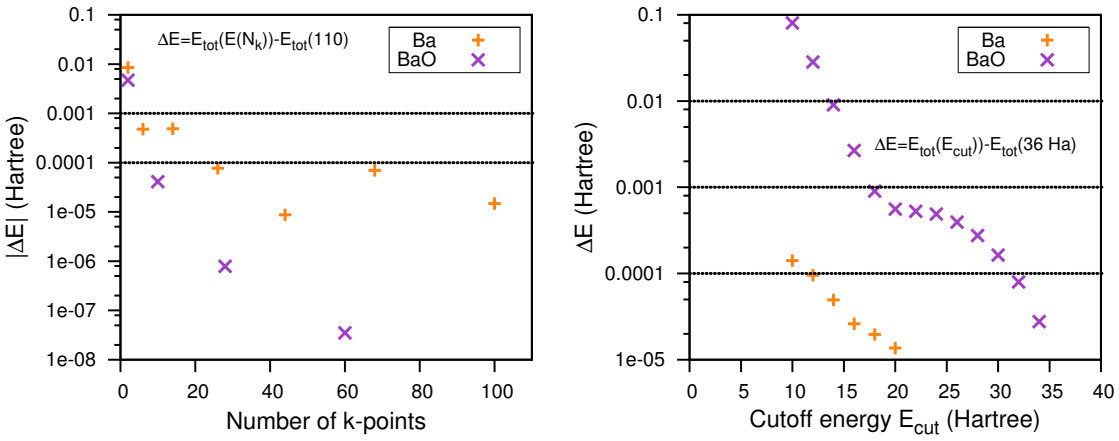

(a) k-point convergence

(b) E_{cut} convergence

Figure 2.2: Convergence curves on the number of k-points (in the irreducible Brillouin zone) and the cutoff energy for barium and barium oxide.

As mentioned in the previous section, the convergence speed can be very different in a pure metal and an oxide (the chemical environment is different but above all,

1. In our material, Gd-doped $BaCeO_3$, the cerium is always in oxidation state 4+, that is why, we are interested in CeO_2 only to test our method, and not Ce_2O_3, in which the cerium is trivalent and should be hence treated in DFT+U to recover a correct insulating behaviour.

there is the influence of the oxygen atomic data), this difference is illustrated on barium in figure 2.2, the same effect is found on cerium and gadolinium. In general, metals need a low cutoff energy but high k-point sampling, while insulating oxides need a much higher cutoff energy but very few k-points.

Note that nothing implies to decrease the energy when converging in k-points (it is not the variational method), that is why we plot the absolute value of ΔE. For the same reason, for the metal, we can see that |ΔE| does not regularly decrease with the increase of the number of k-points. However to achieve convergence with ΔE below 10^{-3} Ha per atom, 6 k-points (in the irreducible Brillouin zone) are enough, even for the metal. In fact this number corresponds to a k-point sampling 4×4×4, but the number of k-points is reduced thanks to the symmetry.

Once we found the accurate parameters (cutoff energy, number of k-points, and, for metals, smearing temperature), we run several calculations on each material varying the volume in order to plot the energy-volume curve. We then fit these curves with the Murnaghan equation of state:

$$E(V) = E_0 + \frac{B_0 V}{B_0'}\left[\frac{(V_0/V)^{B_0'}}{B_0' - 1} + 1\right] - \frac{V_0 B_0}{B_0' - 1} \tag{2.1}$$

where B_0 is the bulk modulus, B_0' the derivative of the bulk modulus, E_0 is the minimum energy and V_0 the equilibrium volume.

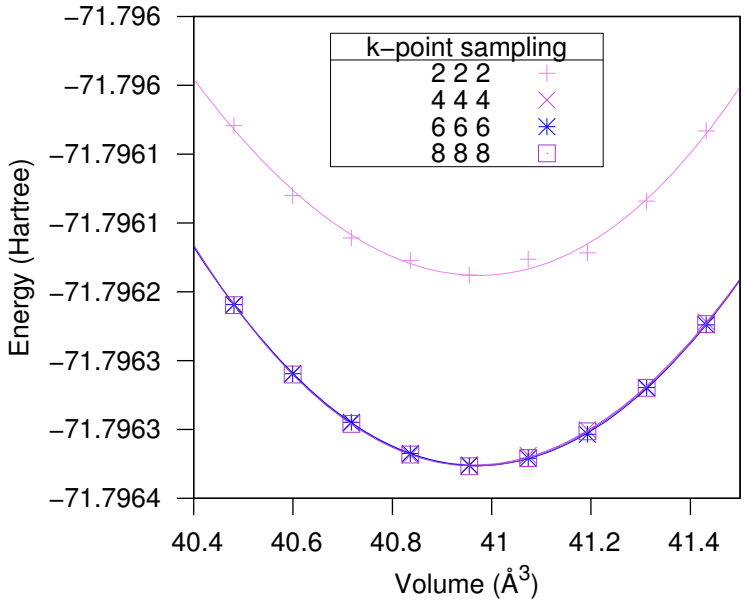

Figure 2.3: Birch-Murnaghan fit for CeO_2 for several k-points sampling.

From this fit, we can thus extract the equilibrium volume and the bulk modulus. Figure 2.3 shows an example of such curve for cerium oxide. Here we can see, that a

k-point sampling 2×2×2 is clearly not enough to get correct value for the equilibrium volume and the total energy.

We also compute the difference between the total energy of our compound and the total energies of isolated atom in order to get the cohesive energies. All these values are presented and compared to previous computed or experimental values in table 2.4. The oxygen atomic data are found to be the key parameter to determine the cutoff energy . It appears that we need a cutoff of 20 Ha to get a convergence on physical energy below 10^{-3} Ha per atom. For testing purpose, to achieve an extremely accurate convergence, we will sometimes use 30 Ha.

Element		V_0 (Å^3/f.u.)	E_{coh} (eV/f.u.)	B_0 (GPa)
Ba [bcc]		63.37	-1.89	8.2
	Exp. [72]	63.25	-1.90	10.3
	GGA [73]	62.98	-1.91	7.6
	LDA [73]	56.34	-2.23	7.9
	GGA All-electron [74]	63.72	–	–
Ce [fcc]		26.60	-4.64	42.5
	Exp. [72]	34.35	-4.32	23.9
	GGA [75]	26.05		48.7
	LDA [71]	23.09		59
Gd [hcp]		33.45	-3.95	35.9
(FM)	Exp. [72]	37.89	-4.14	38.3
	LDA [76]	32.60		40.9
BaO		43.68	-10.08	66.9
	Exp. [77, 78]	42.49		66.2
	GGA [79]	43.41		75.7
	LDA [79]	40.80		91.6
CeO_2		40.97	-21.32	173.5
	Exp. [80]	39.61		220
	GGA [81]	41.14		178.0
	LDA [81]	38.93		210.7

Table 2.4: Unit cell volumes for simple metals and oxides, cohesive energies (with respect to free atoms) and bulk moduli from our simulations, compared with experiments and other DFT calculations.

As expected, a very good agreement is found between our results and previous GGA calculations. We also add a value for the equilibrium volume of Ba computed with an all-electron computation performed by full potential linearised augmented plane waves (FLAPW) method [74]. It is interesting to note how close the result of our PAW computations is to an all-electron value. This is expected and confirms that the frozen core electrons do not participate in chemical bonds.

2.1.2.1 Gd_2O_3

Gd_2O_3 oxide deserves its own section because of its complexity. On the one hand, its bixbyite structure with a primitive cell of 40 atoms is very computationally demanding. On the other hand, magnetism in Gd_2O_3 is still a controversial topic. Both these difficulties have resulted in a weak number of studies on Gd_2O_3. Besides the few existing *ab initio* studies [82] mainly deal with the structures of higher symmetry, namely the hexagonal and the monoclinic structure with 5 and 30 atoms in the primitive cell respectively. However, since the phase transition between the bixbyite structure and the monoclonic one only occurs at 1425 K[83], it is crucial to treat correctly this cubic structure.

Another problem frequently met in rare-earth compounds is the touchy treatment of strongly-correlated electrons in the $4f$ electronic shell. In many correlated materials, standard GGA is not enough to recover the correct physicochemical properties because of a bad representation of $4f$ electrons. For instance, rare-earth oxides (Ce_2O_3 for example) are found to be metallic while there are in fact insulating. We thus wish to check that our theoretical approach can reasonably reproduce the crystal structure, the electronic structure and the magnetism of Gd_2O_3. We tried to optimise the ground-state structure – bixbyite – of Gd_2O_3 with simple GGA, instead of introducing a Hubbard parameter with GGA+U often used for this kind of material (but the GGA+U introduces metastable states in the electronic structure, which need subtle control to obtain the correct ground state [84]).

(a) Bixbyite structure

At room temperature and up to 1425 K, gadolinium sesquioxide Gd_2O_3 has a bixbyite structure (space group $Ia\bar{3}$, body-centered cubic) with a 40-atom primitive cell (see figure 2.4). It then undergoes two phase transitions: first, it becomes monoclinic at 1425 K and then hexagonal at 2443 K [83]. There are two inequivalent sites for Gd atoms in the cubic structure: four Gd^{3+} ions are on site $8b$ (C_2, six identical bonds with oxygen atoms) and 12 Gd^{3+} ions are on site $24d$ (C_{3i}, four short and two longer bonds with oxygen atoms). The bixbyite structure is in fact similar to a fluorite structure in which one fourth of the oxygen atoms have been removed.

A full optimization of lattice constants and atomic positions was performed in both type of magnetic order: first, we assume an antiferromagnetic order (AFM) for the Gd magnetic moments – with opposite spins – shown in figure 2.4, and then a ferromagnetic (FM) order where all spins are aligned. The convergence with the planewaves cutoff was tested by performing two calculations at 20 Ha and 30 Ha. 20 Ha corresponds to the cutoff needed in our previous calculations on oxygen and oxides to get an accuracy of 10^{-3} Ha per formula unit, and 30 Ha is used to check

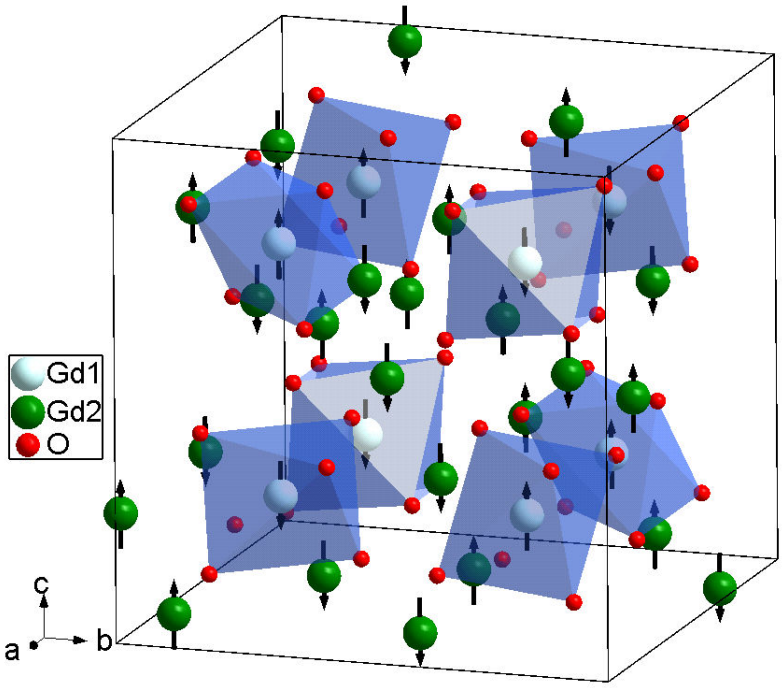

Figure 2.4: Representation of the bixbyite structure of Gd_2O_3 (conventional cubic unit cell – multiplicity = 2 – with 80 atoms) with the AFM order studied in this work.

our values.

Table 2.5 shows the structural parameters of Gd_2O_3 for our computations, previous ones, and experiments. A globally good agreement is observed, especially for structural parameters. The volume equilibrium we found is different by 2% from the one found also using GGA by Hirosaki et al. [82]. This slight discrepancy could be due to the difference in treating the $4f$ electrons: we explicitly treated them whereas they froze them in the core of the pseudopotential.

Up to the fifth decimal (not shown in the table), we found exactly the same structural parameters u, x, y, z whether we use a 20 or a 30 Ha cutoff energy . Therefore, the structural properties are fully converged with respect to the cutoff energy at 20 Ha.

	u	x	y	z	V (Å^3)
GGA (AFM)	-0.0316	0.3906	0.1507	0.3794	80.67
GGA (FM)	-0.0316	0.3907	0.1507	0.3794	80.71
GGA [82]	-0.0319	0.3909	0.1510	0.3793	78.99
LSD-SIC [85]					80.70
Exp. [86]	-0.0304	0.3913	0.1512	0.3811	79.02
	(±0.007)	(±0.0013)	(±0.0012)	(±0.0015)	

Table 2.5: Structural parameters of Gd_2O_3 in its bixbyite structure.

(b) Magnetism

As there is a possible uncertainty on the magnetic structure of gadolinium oxide, we computed both antiferromagnetic and ferromagnetic order. We found the same atomic parameters for both states (AFM or FM) so that the accuracy of structural parameters is not affected whatever the magnetism (see table 2.5).

Most of previous *ab initio* studies on Gd_2O_3 were dealing with clusters, and not crystal. The tendency of these calculations [87, 88] and experimental papers [86] is an antiferromagnetic state slightly more stable than the ferromagnetic one, except for the study of Pedersen and Ojamäe [89]. We found the same result in our calculations: the AFM state is found more stable, though the energy difference between the AFM and FM structures is very small, as shown in table 2.6. In both cases, a magnetic moment of 7 μ_B per gadolinium atom is found, leading to a total moment of 112 μ_B (16 Gd atoms per cell) for the FM state (and zero for the AFM state).

Our result is in the range with previous values, although the study of clusters instead of bulk may induce a difference on E_{FM}-E_{AFM}. We also run a simulation with a non-magnetic structure, imposing a half-filling of $4f$ bands to get occupation numbers identical to the FM case. The total energy of the structure is much higher than magnetic ones by almost 18 eV per formula unit, and so should not be stable.

	E(FM)-E(AFM)
Present work	0.012
$Gd_{12}O_{18}$ cluster [87]	0.001
Gd_2O_3 cluster [88]	0.02

Table 2.6: Energy difference between different magnetic states of Gd_2O_3 (in eV per formula unit).

(c) Electronic structure: need of GGA+U?

The electronic density of states (DOS) for both magnetic structures has been computed. Figure 2.5 confirms that we find an insulator whatever the magnetic order, with a Kohn-Sham band gap of 2.88 eV for the FM state, and 3.27 eV for the AFM state. This larger gap in AFM state has been previously found in small clusters by Ayuela *et al.* [88] and Ning *et al.* [87], using respectively PBE functional on Gd_2O_3 and B3LYP functional on $Gd_{12}O_{18}$. Experimental gaps can have very different values according to the method: conductivity measurements provide a gap of 2.64 eV [90] whereas optical measurements find a gap up to 5.44 eV [91, 92]. The gap we computed is closer to the one of conductivity measurements since we took the lowest point of the conduction band minus the highest point of the valence band (and not the vertical gap). Our results are consistent with all the previous computational

or experimental values, as summarised by Table 2.7. Our AFM value is in good agreement with SIC-LSD [85] (gap for A-type structure) and LDA+U results [93].

Subsequently, we will use a pure GGA as it is found to describe the electronic structure of Gd_2O_3 with reasonable accuracy, despite its usual poor description of strongly correlated electrons.

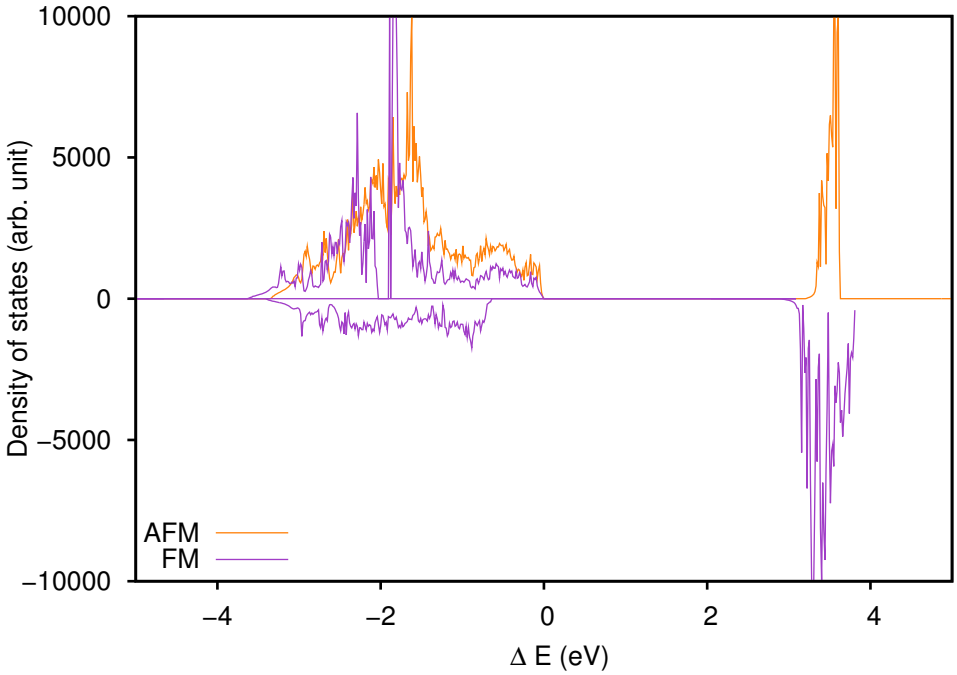

Figure 2.5: Density of states in arbitrary units for both AFM and FM state of Gd_2O_3. The Fermi level is set to zero and the density of states for spin down is shown in negative for the FM state.

Ref.	[90]	[94]	[91]	[95]	[85]	[93]	[88]		[87]		Present	
State	–	–	–	–	–	–	FM	AFM	FM	AFM	FM	AFM
Gap	2.64	5.3	5.44	3.60	3.13	3.9	2.03	2.25	4.03	4.19	2.88	3.27

Table 2.7: Experimental and theoretical values of the energy gap of Gd_2O_3 in eV for the cubic structure (except in Ref. [85]).

These rather good results are related to the fact that the $4f$ orbitals are exactly half-filled in the Gd^{3+} ion. PBE exchange strongly stabilises this electronic structure $4f^7$, in which all electrons have parallel spins. Indeed, the electronic repulsion is minimised – the Pauli principle applies to the orbital parts and electrons spatially exclude each other by filling the different $4f$ orbitals.

It is sufficient to open a wide gap of 5–6 eV between the occupied $4f$ states and the unoccupied $4f$ states. The $4f$ bands appear as two narrow peaks in figure 2.5: the occupied band in the middle of the valence band while the unoccupied one is at

the bottom of the conduction band. The narrow character of the $4f$ peaks proves that there is few hybridisation between the $4f$ orbitals of Gd and the $2p$ orbital of oxygen. We therefore expect a correct description of Gd-doped $BaCeO_3$ within the GGA-PBE functional.

2.1.3 Pure $BaCeO_3$

2.1.3.1 Structure: Pnma space group

Barium cerate has a perovskite structure, as many ternary oxides. At very high temperature, the structure is cubic with a primitive cell of 5 atoms shown on figure 0.3. The B-site – in the middle of the oxygen octahedron– is occupied by a cerium atom and the A-site by a barium atom. Under ambient pressure, $BaCeO_3$ (BCO) undergoes three phase transitions when increasing temperature [96–98].

At low temperature, the structure is orthorhombic with space group $Pnma$, then around 550 K, it keeps an orthorhombic structure but changes its space group to $Imma$. At 670 K, $BaCeO_3$ becomes rhombohedral $R\bar{3}c$ through a first-order transition. And finally, above 1170 K, it is cubic with space group $Pm\bar{3}m$.

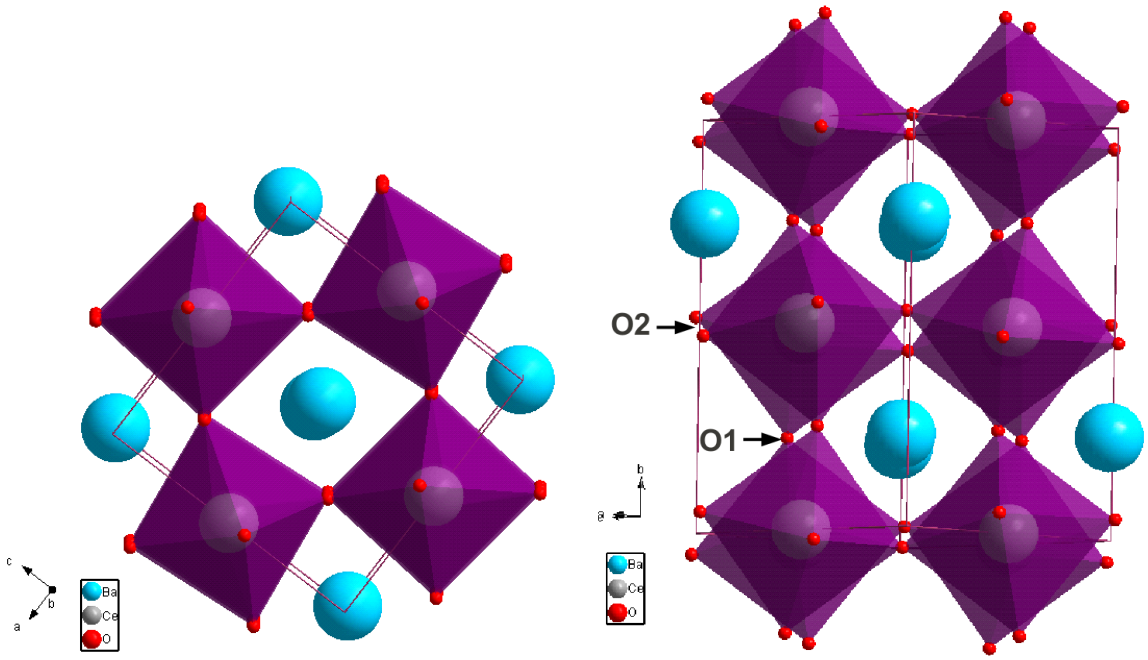

(a) In phase (b) Anti-phase

Figure 2.6: Structure of $BaCeO_3$ in its $Pnma$ space group with its two tilts: in phase along b-axis (left) and anti-phase along a and c-axis (right).

These phase transitions can also be expressed from the point of view of oxygen octahedral rotations, using Glazer's notations [99]. Indeed, oxygen octahedra, charac-

teristic of perovskite structure, have a tendency to tilt. If all the oxygen octahedra along an axis turn in the same direction, the tilt is said to be « in phase » and is noted a^+ (figure 2.6(a)), if they alternate turning in opposite direction, the tilt is said « in anti-phase » and is noted a^- (figure 2.6(b)). A tilt in phase corresponds to the freezing of a phonon mode localised at the M point of the first Brillouin zone of the parent cubic structure, while a tilt in anti-phase is associated to the R point. With these notations, the orthorhombic ground state structure *Pnma* is noted: $a^-b^+a^-$, with one tilt in-phase along the b-axis, and a tilt anti-phase along a-axis and c-axis (identical for both axis). The *Pnma* cell and its oxygen octahedra tilts are represented in Fig. 2.6. When heating, the tilt in-phase disappears so that we get a different orthorhombic structure $a^-b^0a^-$. The orthorhombic-rhombohedral transition implies a first order transition as a new tilt appears suddenly: the tilt structure is then $a^-a^-a^-$. Finally, the structure becomes cubic at high temperature with no tilt at all ($a^0a^0a^0$).

Around 900 K, the working temperature of a protonic ceramic fuel cell (PCFC), the structure of $BaCeO_3$ is rhombohedral. We thus first performed geometry optimisations in the $R\bar{3}c$ space group. But the material systematically went back in its ground-state *Pnma* structure: the rhombohedral structure does not constitute a local minimum and may be stabilised at high temperature by entropy through thermal vibrations. Therefore, we will only study $BaCeO_3$ – pure or with defects – in its ground state *Pnma*. The *Pnma* structure gives two non equivalent positions for the oxygen atoms: apical oxygen O1 and equatorial oxygen O2, shown in figure 2.6(b).

Structural and lattice parameters are shown in table 2.8 and compared to other data. The atomic positions are in very good agreement with previous calculations ($\Delta d < 0.005$), and even experiments ($\Delta d \leqslant 0.01$). As expected, lattice constants are slightly overestimated by the GGA calculations.

2.1.3.2 Determination of convergence parameters

Once again, we tested the three cutoff radii for oxygen, and get similar results to the ones obtained in binary oxides. To achieve a high accuracy with a reasonable cutoff energy, atomic data with the cutoff radius r_{O2} are the more appropriate. Note that there is absolutely no PAW sphere overlap with the chosen cutoff radii in $BaCeO_3$ and Gd-doped $BaCeO_3$.

Tables 2.9 and 2.10 show the total energy and the difference of total energy per formula unit between the considered parameter and the most accurate one. The lowest k-point sampling we tested, *i.e.* 3×2×3 k-points[2], is more than enough to

2. The number of k-points needed is inversely proportional to the lattice parameter: for the same material, if we double our lattice parameter, we will need twice fewer k-points. That is why the use of a k-point grid 2×2×2 is more than enough for a supercell.

Wyckoff positions	Element	Present	GGA [100]	Exp. [101]	Exp. [96]
	Ba(x)	0.0254	0.0273	0.0204	0.0123
4c	Ba(y)	0.2500	0.2500	0.2500	0.2500
	Ba(z)	-0.0080	-0.0077	-0.0085	-0.0038
	Ce(x)	0.0000	0.0000	0.0000	0.0000
4b	Ce(y)	0.0000	0.0000	0.0000	0.0000
	Ce(z)	0.5000	0.5000	0.5000	0.5000
	O1(x)	-0.0199	-0.0200	-0.0094	-0.0089
4c	O1(y)	0.2500	0.2500	0.2500	0.2500
	O1(z)	0.4204	0.4194	0.4287	0.4290
	O2(x)	0.2802	0.2833	0.2790	0.2707
8d	O2(y)	0.0431	0.0446	0.0384	0.0377
	O2(z)	0.7208	0.7186	0.7235	0.7302
lattice parameter					
a (Å)		6.293	6.28	6.214	6.227
b (Å)		8.867	8.81	8.774	8.791
c (Å)		6.280	6.30	6.233	6.252

Table 2.8: Atomic positions and lattice parameters of $BaCeO_3$ (*Pnma*) compared with previous GGA computations and experiences.

achieve an accuracy of 10^{-3} Ha per formula unit. For the cutoff energy, table 2.10 suggests that we need at least a value of 30 Ha. However, we are never interested in the total energy, but always in energy differences such as formation energy. We can thus look at the variation of cohesive energy (from single atoms) and formation energy (from binary oxides: CeO_2 and BaO) of $BaCeO_3$. Table 2.11 shows the results in eV per formula unit (1 Ha=27.211 eV). Note that this difference in energy does not have necessary a decreasing value when increasing the cutoff energy. The accuracy on the formation energy is already far below 10^{-3} Hartree with the lowest cutoff (16 Ha). A cutoff of 20 Ha gives also a very good accuracy (0.01 eV) on the cohesive energy.

In this thesis, we will preferentially use this cutoff of 20 Ha, but run some tests at 30 Ha to check the accuracy of our values.

Table 2.12 compares the results obtained with a cutoff of 20 Ha and a k-point sampling of 3×2×3 with previous experiments and GGA computations. The unit cell volume is slightly overestimated – as expected from a GGA simulation – and the formation energy is underestimated by about 9%.

Finally, in this material, cerium atoms are also in state 4+ (as in CeO_2), therefore we should not need GGA+U as there are no f-electrons. Considering the defect we will introduce, there is no possibility for cerium to become Ce^{3+}. However, if one

k-point	E_{tot} (Ha)	ΔE (Ha/ f.u.)
3×2×3	-455.559728	0.000028
4×3×4	-455.559832	0.000002
6×4×6	-455.559844	-0.000001
9×6×9	-455.559840	

Table 2.9: Total energy and error energy ($\Delta E=E_{tot}(N_k)-E_{tot}(9\times6\times9)$) of $BaCeO_3$ for different k-point sampling at fixed E_{cut}=30 Ha.

E_{cut}	E_{tot} (Ha)	ΔE (Ha/ f.u.)
16	-455.526707	0.013959
18	-455.562369	0.005044
20	-455.568696	0.003462
22	-455.569184	0.003340
24	-455.570303	0.003060
26	-455.572698	0.002461
28	-455.575597	0.001737
30	-455.578225	0.001080
32	-455.580129	0.000604
34	-455.581329	0.000304
36	-455.581950	0.000148

Table 2.10: Total energy and error energy ($\Delta E=E_{tot}(E_{cut})-E_{tot}(50\text{ Ha})$) of $BaCeO_3$ for different cutoff energies at fixed k-point sampling 3×2×3.

E_{cut}	E_{coh} (eV/f.u.)	Δ E_{coh} (eV/f.u.)	E_{form} (eV/f.u.)	Δ E_{form} (eV/f.u.)
16	-31.905	-0.022	-0.498	0.000
18	-31.897	-0.014	-0.499	-0.001
20	-31.894	-0.011	-0.498	0.000
22	-31.893	-0.009	-0.498	0.000
24	-31.889	-0.006	-0.497	0.000
26	-31.888	-0.004	-0.497	0.000
28	-31.886	-0.003	-0.497	0.000
30	-31.886	-0.002	-0.498	0.000

Table 2.11: Formation energy from binary oxides (BaO and CeO_2) and cohesive energy of $BaCeO_3$. The difference ΔE is given by $\Delta E=E_{tot}(E_{cut})-E_{tot}(36\text{ Ha})$.

wants to study other kinds of defects in $BaCeO_3$ that would lead to the presence of Ce^{3+}, the use of GGA+U may be necessary [105].

Summary

Consequently, we choose the hardest cutoff radius for hydrogen and an intermediate one, rather soft, for oxygen ($1.4\,a_0$). For this configuration, we will use a cutoff energy of 20 Ha, ensuring an accuracy better than 0.01 eV on physical energies (and around 0.01 eV for cohesive energies). To get an even better accuracy, some tests will be run at a cutoff of 30 Ha. If we needed a k-point mesh of 3×2×3 in the primitive *Pnma* cell of 20 atoms, 2×2×2 k-points for our 80-atoms supercell would be more than enough to get a very high accuracy. These two parameters ensure an error per atom below 10^{-3} Ha.

	V_0 (Å^3)	E^f (eV/f.u.)	B_0 (GPa)	Band Gap (eV)
Present	350.4	-15.97	107.37	2.20
Exp.	340.8 [102]	-17.52 [103]	103.7 [102]	3.2 [104]
GGA	348.58 [100]			2.6 [104]

Table 2.12: Equilibrium volume (per primitive cell), formation energy (*i.e.* with respect to Ba, Ce and O in their standard state), bulk modulus and band gap of $BaCeO_3$.

Once again, to be absolutely sure of the reliability of our results, some tests have been run with the hard cutoff radius of oxygen r_{O1}. These atomic data are supposed to be very accurate, but require a much higher cutoff energy (46 Ha for perfect accuracy – 10^{-3} Ha on total energies – or 36 Ha for relaxed criterion – 10^{-3} Ha on physical energies) to get results with the same accuracy. We have checked that it provides quasi-identical results as the radius r_{O2} we used for all our calculations.

Table 2.13 shows the results of these tests for formation enthalpies of some compounds. It appears that the « soft » cutoff radius tends to slightly overestimate formation energies by 1%. This difference seems rather acceptable considering the huge gain in computational cost.

This is even more true if we are computing difference of formation energies (as needed to study thermodynamic properties) : for instance the formation enthalpy of $BaCeO_3$ from $BaO+CeO_2$ is exactly the same (-0.49 eV) whatever the atomic data. Moreover, we can notice that the difference between formation enthalpies computed with soft and hard cutoff radius is exactly the same (0.17 eV) for pure $BaCeO_3$ and all the three phases of Gd-doped $BaCeO_3$. This error will thus disappear when we compute differences between these quantities.

	$r_O1 = 1.1\ a_0$ ($E_{cut} = 46$ Ha)	$r_O2 = 1.4\ a_0$ ($E_{cut} = 20$ Ha)	Error
O_2	-6.20	-6.26	1.0%
BaO	-5.00	-5.06	1.2%
CeO_2	-10.31	-10.42	1.1%
Gd_2O_3	-17.21	-17.39	1.0%
$BaCeO_3$	-15.80	-15.97	1.1%
	Gd-doped $BaCeO_3$		
dry	-15.47	-15.64	1.1%
oxidized	-15.52	-15.69	1.1%
hydrated	-15.71	-15.88	1.1%

Table 2.13: Formation enthalpy in eV of some compounds for two different calculations, and difference in percentage between both atomic data.

2.2 Supercell and defects

All calculations will be parallelized on three different levels : k-points sampling, number of bands (linked to the number of electrons), FFT grid (FFT meaning Fast Fourier Transform). Typical geometry optimizations were run on a thousand CPU cores.

2.2.1 Supercell

At first thought, we wanted to study $BaCeO_3$ at the working temperature of a fuel cell, i.e. in its rhombohedral structure $R\bar{3}c$. Calculations in this state have thus been done and we found a total energy only slightly higher than the orthorhombic state one by 0.017 eV per formula unit.

The primitive cell of rhombohedral state is a 10-atom cell with primitive vectors expressed on the cubic vectors:

$$\begin{aligned}\vec{a}_{rhombo} &= \vec{b}_{cubic} + \vec{c}_{cubic} \\ \vec{b}_{rhombo} &= \vec{c}_{cubic} + \vec{a}_{cubic} \\ \vec{c}_{rhombo} &= \vec{a}_{cubic} + \vec{b}_{cubic}\end{aligned}$$

We built an 80-atom supercell from this primitive cell 2×2×2. However, when breaking the symmetry by introducing a defect, we observed that the structure fell back to the orthorhombic ground state. Therefore, the study of the rhombohedral structure with defects is not possible by DFT. We chose to study instead the orthorhombic structure existing at room temperature up to 550 K.

We checked that this lattice was compatible with our 80-atoms supercell by expressing the supercell vectors as a linear combination of the orthorhombic vectors. The orthorhombic vector of the 20-atom $Pnma$ primitive cell can be expressed as:

$$\begin{aligned}\vec{a}_{ortho} &= \vec{a}_{cubic} + \vec{c}_{cubic} \\ \vec{b}_{ortho} &= 2\vec{b}_{cubic} \\ \vec{c}_{ortho} &= \vec{a}_{cubic} - \vec{c}_{cubic}\end{aligned}$$

and the supercell vectors are given by:

$$\begin{aligned}\vec{A} = 2\vec{a}_{rhombo} &= 2\vec{b}_{cubic} + 2\vec{c}_{cubic} \\ \vec{B} = 2\vec{b}_{rhombo} &= 2\vec{c}_{cubic} + 2\vec{a}_{cubic} \\ \vec{C} = 2\vec{c}_{rhombo} &= 2\vec{a}_{cubic} + 2\vec{b}_{cubic}\end{aligned}$$

Therefore, we have:

$$\begin{aligned}\vec{A} &= \vec{a}_{ortho} + \vec{b}_{ortho} - \vec{c}_{ortho} \\ \vec{B} &= 2\vec{a}_{ortho} \\ \vec{C} &= \vec{a}_{ortho} + \vec{b}_{ortho} + \vec{c}_{ortho}\end{aligned}$$

We can thus keep our initial 80 atoms supercell – 2×2×2 rhombohedral cell – even to study the orthorhombic state. All our work will be done in this supercell. We will also run a few test computations on another 80 atoms supercell – 2×1×2 orthorhombic cell – to check that another periodic arrangement of defects provides similar results.

2.2.2 Treatment of defects

Considering, the multitude of existing methods to correct the energy shift due to the treatment of charged cell, we favoured the use of neutral cell only. To do so, **we introduced systematically two compensating defects in our cells, exactly as a « real » system**. This approach has nevertheless the drawback to prevent the study of truly isolated defects.

We will use the Kröger-Vink notations to deal with defects. An atom M replacing an atom N will be denoted according to its charge:

- negative: $M_N^{'}$
- neutral: M_N^X
- positive: $M_N^{\bullet}$

In our compound we will have three kinds of atomic defects:

- a gadolinium atom Gd^{3+} replacing a cerium atom Ce^{4+}: $Gd_{Ce}^{'}$
- an oxygen vacancy instead of an oxygen atom O^{2-}: $V_O^{\bullet\bullet}$
- a protonic defect OH^- replacing an oxygen atom O^{2-}:$OH_O^{\bullet}$

As we want to consider only neutral cells, we will put two Gd dopants to study one oxygen vacancy and one Gd dopant to study one protonic defect. The charges of the point defects (-1 for $Gd_{Ce}^{'}$, +2 for $V_O^{\bullet\bullet}$, +1 for $OH_O^{\bullet}$) are formal values, they are different from the charge that would be obtained from examination of the electron density at the defective site and at the undefective site. In particular, the protonic defect $OH_O^{\bullet}$ is not a really bare proton and the O-H bond keeps an ionocovalent character.

Finally, the introduction of gadolinium, a magnetic element, in $BaCeO_3$, implies to run spin-polarised computations. When two dopants are introduced, we can choose opposite spin (antiferromagnetic order) or parallel spin (ferromagnetic order). This choice should not have any impact on total energy as both gadolinium atoms are placed as far as possible in the supercell. Note that we only use collinear magnetism, the possible spin-orbit coupling effects are ignored.

All the convergence parameters have been chosen after a very careful study of structural and energetic properties for simple elements, binary oxides and pure $BaCeO_3$. Several atomic data have been tested for light elements and the best compromise between accuracy and computational cost has been selected. The use of the exchange-correlation functional PBE, without a Hubbard term to treat f-orbitals, is justified by the special configuration of half-filling in gadolinium, and to the absence of f-electrons in Ce^{4+}. Finally, the treatment of defects is relatively simple as it does not imply any band alignment and other corrections: we will treat only neutral supercells containing charge-compensated defects.

Chapter 3

Thermodynamics aspects: hydration and oxidation

In this chapter, we will present a study of three possible states of Gd-doped $BaCeO_3$ (BCGO): dry, hydrated and oxidized compound. We will analyse in details the possible positions for proton and oxygen vacancies, and finally discuss the thermodynamics of hydration and oxidation in this material.

Contents

There is an infinite number of existing intermediate states, with only some oxygen vacancies filled, but we will only be interested in the three extreme states when all the oxygen vacancies are filled, with the same kind of molecules, or none:

- the dry compound ($BaCe_{1-\delta}Gd_{\delta}O_{3-\frac{\delta}{2}}$): this is the initially synthesised material, it contains oxygen vacancies (one for every two dopants) ;
- the fully hydrated compound ($BaCe_{1-\delta}Gd_{\delta}O_3H_{\delta}$): the material after all oxygen vacancies have been filled up with (dissociated) water molecules (one proton for one dopant);
- the fully oxidized compound ($BaCe_{1-\delta}Gd_{\delta}O_3$): the material after all oxygen vacancies have been filled up with (dissociated) oxygen molecules.

In order to compute the defect positions, we have fully optimized the geometry of the system (atomic positions and supercell vectors) using the efficient Broyden-Fletcher-Goldfarb-Shanno minimization scheme implemented in ABINIT, with an optimization criterion on atomic forces of 1.0×10^{-4} Ha/Bohr ($\approx 0.005\,\mathrm{eV\,\AA^{-1}}$).

3.1 Dry compound

This is the state we get when we synthesised Gd-doped barium cerate (BCGO) from binary oxides:

$$BaO + (1-\delta)CeO_2 + \frac{\delta}{2}Gd_2O_3 \rightarrow BaCe_{1-\delta}Gd_{\delta}O_{3-\delta/2}$$

In this material, the elements Ba, Ce and Gd keep the same oxidation degree they have in binary oxide : +2, +4 and +3 respectively. $BaCe_{1-\delta}Gd_{\delta}O_{3-\delta/2}$ can be seen as a compound of $BaCeO_3$ in which some cerium atoms have been replaced by gadolinium (dopant) creating negative defects Gd'_{Ce}. This leads to the removal of some oxygen atoms to compensate the missing charge, creating oxygen vacancy $V^{\bullet\bullet}_{O}$, one for every two dopants.

3.1.1 Doping influence on atomic and electronic structure

3.1.1.1 Atomic structure

Doping can affect the space group of perovskite oxide, or significantly modify their lattice parameters, especially at high dopant concentration. Nevertheless, previous experimental studies on Y-doped $BaCeO_3$ [106] and Gd-doped $BaCeO_3$ [107] have found that the substitution of Ce^{4+} by trivalent ions (Y^{3+} and Gd^{3+}) has almost no influence on the structure, but induces a shift in the phase transition temperatures. **BCGO would thus keep the *Pnma* structure at zero and room temperature.**

Indeed, experimentally, it is found that Gd-doped $BaCeO_3$ keeps its perovskite orthorhombic structure even for high value of doping up to $\delta = 20\%$ [108], as shown in table 3.1. In our calculations, we also found that the tilt system $a^-b^+a^-$, is preserved even though, in our supercell, the *Pnma* symmetry is broken due to the presence of defects. The change induced by doping in the lattice parameters is very small for both experiments and GGA calculations (around 1 ‰). This confirms that replacing Ce^{4+} by Gd^{3+} has little influence on the structural properties. This may be due to the fact that both Ce^{4+} and Gd^{3+} have very close ionic Shannon radii: 0.87 Å and 0.94 Å respectively [109]. The same argument can apply to Y^{3+} as its ionic radius is 0.90 Å.

Compound		Cell parameters (Å)		
		a	b	c
$BaCeO_3$				
	GGA [Present]	6.293	8.867	6.280
	GGA [100]	6.28	8.81	6.30
	XRD [96]	6.227	8.791	6.252
$BaCe_{1-\delta}Gd_\delta O_{3-\frac{\delta}{2}}$				
δ=0.125	GGA [Present]	6.292	8.865	6.282
	XRD [Present]	6.231	8.772	6.248
δ=0.10	XRD [110]	6.221	8.770	6.244
δ=0.15	XRD [108]	6.203	8.769	6.243
δ=0.20	XRD [108]	6.223	8.777	6.241

Table 3.1: Lattice constants of pure BCO and BCGO.

In our calculations, the possible values for the doping rate δ are limited: as there are only 16 Cerium in our 80-atom supercell, we can either have $\delta = 6.25\%$, $\delta = 12.5\%$ or $\delta = 25\%$. We simulate BCGO by introducing two gadolinium atom and one oxygen vacancy leading to a doping rate of $\delta = 12.5\%$. But experiments usually take round numbers such as 10 or 20%, that is why experimental data on BCGO at a level of doping of 12.5% are lacking in the literature.

In order to compare our simulations with experiments, we did a little experimental work and performed X-ray diffraction experiments on BCGO containing exactly 12.5% of Gd. This work was done at Centrale Paris, in the SPMS (Structure, properties and modelling of solids) laboratory. We synthesised this compound using freeze-drying method. After dissolving barium, cerium and gadolinium acetate powders in water in the stoichiometric ratio, the solution was homogenized and sprayed into liquid nitrogen to get frozen droplets. The solvent was then eliminated by sublimation and the resulting nanopowder was pre-calcined at 600 °C for 10 min. Finally, the greyish powder was calcined at 1200 °C for 4 h. X-ray diffraction was then performed

to check whether there were impurity phases or not and to determine the lattice parameters through Rietveld refinement. Table 3.1 shows that the parameters found when δ=0.125 are almost identical to the ones of previous experiments on $BaCeO_3$ doped with 10% of Gadolinium.

3.1.1.2 Band gap and magnetism

In our 80-atom supercell, we put one oxygen vacancy $V_O^{\bullet\bullet}$ and two dopants Gd'_{Ce} so that the electrical neutrality is achieved without introducing any electronic defects. However, both cerium and gadolinium are touchy elements because of their f-electrons, usually poorly treated by GGA. Even though Ce is supposed to be in oxidation state 4+, without f-electrons, and Gd^{3+} is well behaving in GGA (see section 2.1.2), we have to check that the insulating character of BCGO is not lost in GGA calculations. This insulating behaviour is fundamental for a good electrolyte.

We computed the electronic density of states for both BCO and BCGO with the GGA-PBE exchange-correlation functional. We found a band gap of 2.2 eV for $BaCeO_3$, lower than the experimental band gap of 3.2 eV [104], as expected. For Gd-doped $BaCeO_3$, the band gap is slightly smaller: 1.8 eV but still enough to get the insulating character.

Since gadolinium is magnetic, all our computations were spin-polarised, as previously explained. With two dopants in the supercell, we have two choices for the magnetic order: antiferromagnetic or ferromagnetic. As the dopants are far from each other ($\approx$ 9 Å), we expect to find no difference on total energies whatever the magnetic choice. Indeed, computing both magnetic structures, DFT calculations give a total energy difference of approximatively 10^{-7} Ha per formula unit. This is four orders of magnitude below the error bar: AFM and FM order can thus be considered as equivalent. Furthermore, we checked that the magnetic moment on gadolinium atom was not dependent on the magnetic structure. In oxidation state 3+, gadolinium has the electronic structure: $5s^2\ 5p^6\ 4f^7\ 5d^0\ 6s^0$, and hence should have a moment of 7 μ_B. A simple integration of the electronic density in the PAW sphere gives a moment of 6.91 μ_B for both AFM and FM order, very close to the expected value (the difference between the number of up and down electrons in the global supercell is equal to 0 and 14 μ_B respectively).

3.1.2 Energy landscape of oxygen vacancies

As explained, we substitute two Ce atoms by two Gd atoms, placed in the supercell such as their distance is maximal, and remove one oxygen atom. Where should we place the oxygen vacancy?

In pure barium cerate, there would be only two non-equivalent positions: O1 or O2. However, if we look at the B-O distances in the equatorial plane (ac) of a perovskite oxide ABO_3 in *Pnma* structure, there are two kinds of distances: d_1 and d_2. These distances, as shown in figure 3.1, alternate along the B-O chains (along a-axis and c-axis). The introduction of one dopant in the place of Ce breaks the symmetry, and the equivalence between the four equatorial oxygens O2 of its first coordination shell disappears. The set of the four O2 split into two sets called O2 and O2' in the following. The two oxygens of each set are symmetrically placed with respect to Gd, the d_1 and d_2 distances between them and Gd are almost alike: 2.295 Å and 2.296 Å after structural optimisation, and slightly larger than the Ce-O bond.

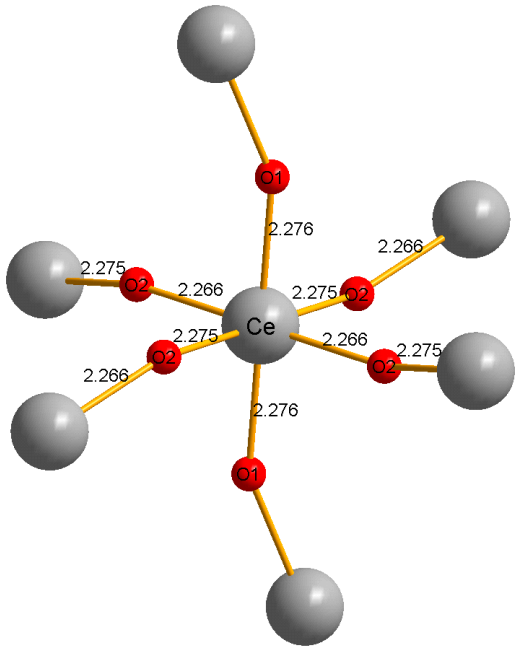

Figure 3.1: Ce–O different distances in the *Pnma* structure. The four equatorial oxygens O2 are equivalent but there are two different bond lengths Ce–O2. Therefore, if a dopant replace a cerium atom, the equivalence between oxygen would be broken, giving two different group of equatorial oxygens O2 and O2'.

To study all the possible positions of the oxygen vacancy, we first focus on the first coordination shell of Gd with three possible sites: O1, O2 and O2'. Calculations shows that O2 and O2' sites have very close energies ($\Delta E < 0.015$ eV, i.e. within the error bar of 10^{-3} Ha) and will thus be considered as one single site for the oxygen vacancy.

Therefore, we have only two positions near the dopant O1 and O2. We should now look at the difference in energy when the distance between oxygen vacancy and gadolinium increases. Since the difference – in energy and bond length – between O2

and O2' is insignificant near Gd, we can also consider that there are only two non equivalent oxygen atoms O1 and O2 beyond the first coordination shell. Considering the size of our supercell and the presence of two dopants in it, we can test three different distances (from 2.3 to 6.2 Å): 1st, 2nd and 3rd neighbour of the gadolinium. This leads to 6 possible positions shown in figure 3.2.

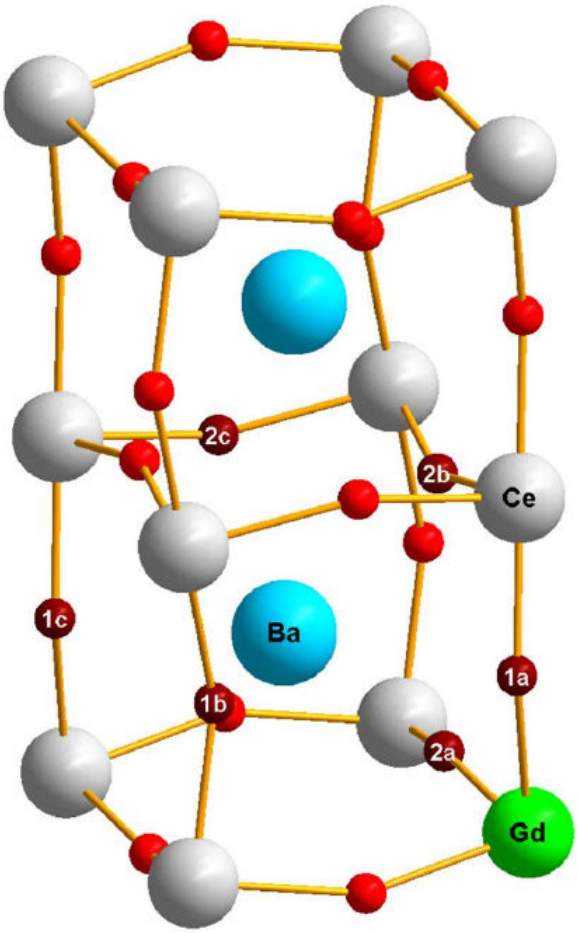

Figure 3.2: Possible positions for the oxygen vacancy in Gd-doped barium cerate. 1 and 2 stand for the oxygen type (O1 or O2), and the letter a, b, c represent a 1st, 2nd and 3rd neighbour of Gd.

The result of these six computations is represented in figure 3.3. The energy is plotted for the six positions, relative to the most stable one: O1 near Gd. The dopant and the oxygen vacancy are attracted to each other: indeed, the total energy of the oxygen vacancy is lower near the dopant than far from the dopant. This was expected since these defects have opposite formal charge. However, this interaction seems to be rather short-range: beyond the first coordination shell, the positions have very close total energies. From this observation, we can define an approximate interaction energy (sometimes called "association energy") as the mean value (on O1 and O2 sites) of the energy difference between the closest and the furthest positions, which

gives $E_{int}(Gd'_{Ce}\text{-}V^{\bullet\bullet}_O) \approx -0.18\,eV$.

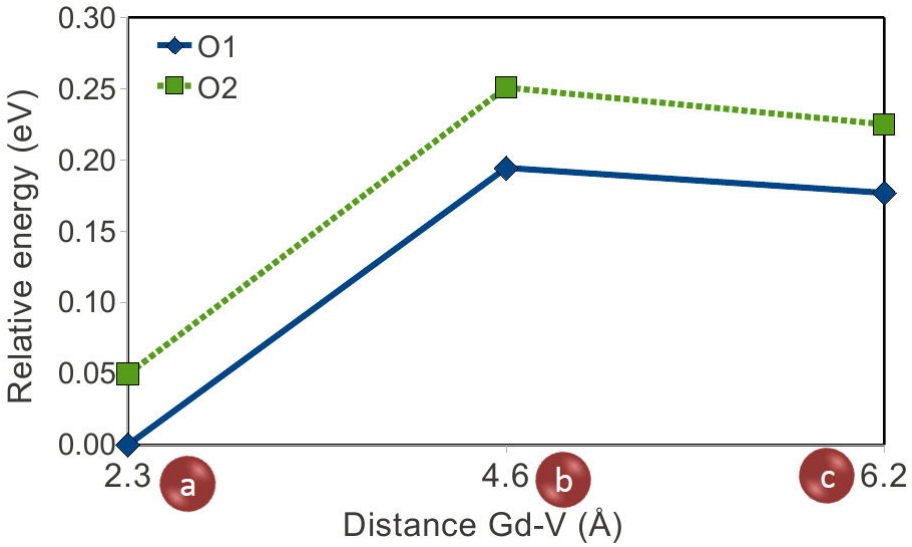

Figure 3.3: Energies of the different positions for the oxygen vacancy (eV), relative to the most stable one (O1 in the oxygen octahedron surrounding the dopant). The difference O2/O2' is ignored even in the first coordination shell due to the energetic proximity of the corresponding configurations.

3.2 Hydrated compound

Under humid atmosphere, the dry compound can incorporate water molecules. They dissociate in the oxygen vacancies to provide protonic defects (hydroxyl groups) $OH^{\bullet}_O$. This is the reaction of hydration:

$$H_2O + V^{\bullet\bullet}_O + O^X_O \rightarrow 2OH^{\bullet}_O \tag{3.1}$$

Once again the metallic elements keep their formal oxidation state. There is one dopant Gd'_{Ce} for one proton $OH^{\bullet}_O$ so that no electronic defect should appear. DFT calculations show that the band gap is very close to the one of the dry compound: 1.86 eV, hence keeping its insulating character.

After incorporation of a water molecule into an oxygen vacancy in the dry compound, we get an 80-atom supercell of the hydrated compound with two dopants and two protonic defects. We can reduce the doping rate from 12.5 % to 6.25 % to simplify the number of defects to treat. We will thus consider a supercell with one dopant Gd'_{Ce} and one proton $OH^{\bullet}_O$ to study the possible stable positions, but with two dopants and two protons to compute the hydration enthalpy. Both these structures correspond to the fully hydrated case, no oxygen vacancy is remaining.

3.2.1 Stable positions for the proton

3.2.1.1 Position of the O–H bond

We want to determine the possible positions for the proton. The hydroxyl group $OH_O^\bullet$ should point roughly along the [100] direction in the interoctahedral space. However some studies argue that they can differ from that position and lean towards the B-site, and even align along the oxygen octahedron edge [11, 111]. This alignment, leading to 8 possible positions per oxygen, would be due to the dipolar moment of the protonic defect $OH_O^\bullet$, preferring to point to neighbouring oxygen. In fact, the direction seems to strongly depend on the lattice parameter:

- along the octahedra edge, for perovskites with small lattice parameter such as $SrTiO_3$ [112, 113] or $LaMnO_3$ [112] ($a_0 = 3.91$ Å for both),
- along the pseudocubic axis, for perovskites with large lattice parameter such as $SrZrO_3$ [20] or $BaCeO_3$ [114, 115] ($a_0 = 4.14$ Å and $a_0 = 4.41$ Å respectively)

This phenomenon can easily be explained: when the lattice constant decreases, the nearest oxygen gets closer and closer to the proton, attracting it sufficiently to bend the O–H bond towards the octahedron edge. On the other side, if the lattice parameter is large, the distance between the proton and the oxygen belonging to the same octahedron will reduce this attraction. This is even more true in a distorted perovskite: as the oxygen octahedra tilt, the distance between two oxygens belonging to the same octahedron is kept constant, while two facing oxygens – belonging to different octahedra – may get closer or further.

In our case, the lattice parameter is large and we have a distortion, so we have to study 4 possible positions per oxygen atom, along the pseudocubic directions. This positions are denoted a, b, c and d: a and b positions correspond to a cus site while c and d positions are on a hollow site (see figure 3.4).

Introducing a dopant may also affect the orientation of the O–H bond, as shown in figure 3.4. The electrostatic interaction between dopant and protonic defect should be more pronounced if the proton is on an hollow site (c/d type) than on a cus site (a/b type). Angles between the pseudocubic direction and the actual bond O–H are shown in table 3.2 for the eight possible positions, described in the following section, near the dopant and far from the dopant. As expected when looking at figure 3.4, the cus site – far from B-site – bends less than the hollow site – closer to the B-site. Indeed, positions a and b are almost aligned along the pseudocubic direction (deviation less than 1 or 2°), while c/d type positions deviate slightly more ($\approx 5°$), especially when they are near the dopant. The dopant, defect with a negative charge, tends to attract the positive protonic defect.

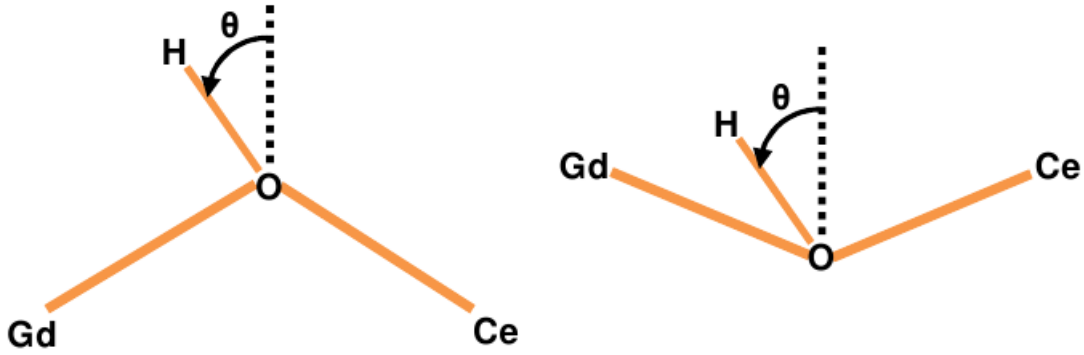

Figure 3.4: Angles between the pseudocubic direction and the actual O–H bond for the two subcategories of protonic sites (left: cus or a/b-type; right: hollow or c/d-type).

Position	θ near Gd	θ far from Gd
1a	-0.1°	0.2°
1b	-0.1°	0.2°
1c	5.3°	0.5°
1d	3.5°	0.5°
2a	-0.5°	0.6°
2b	1.6°	1.2°
2c	5.0°	2.1°
2d	8.2°	4.9°

Table 3.2: Values of the angle described in figure 3.4, for a proton near a dopant, and far from a dopant.

3.2.1.2 Energy landscape of protonic defect

Due to the low symmetry of *Pnma* space group, there are many possible non equivalent positions for the proton. In principle, in pure barium cerate, there are four possible directions per oxygen atom and two kinds of oxygen leading to 8 different positions.

When we introduce a dopant, as explained in section 3.1.2, we create two types of equatorial oxygens O2 and O2', that may not be equivalent. As we did for the oxygen vacancy, we have to see whether both oxygens give identical protonic sites or not. If we only focus on protons bonded to oxygen atoms first neighbor of the Gd dopant for now, we have 12 possible positions – four on each oxygen atom. The four sites on each oxygen atom are labelled a, b, c and d, they are represented in figure 3.5 on O1 and O2 only. Table 3.3 shows the energies of the 12 studied sites, relative to the most stable one (1a). It appears that almost no difference is found between O2 and O2' site (the largest difference,found for 2c and 2c', is still below the error bar: 0.013 eV$\approx 5 \times 10^{-4}$ Ha), whereas the four sites of O1 (1a, 1b, 1c, 1d)

have very different energies. Therefore, we can neglect the asymmetry induced by the introduction of Gd, and consider the sites on O2 and O2' to be analogous.

Site	O1	O2	O2'
a	(1a) 0.000	(2a) 0.165	(2a') 0.163
b	(1b) 0.008	(2b) 0.052	(2b') 0.052
c	(1c) 0.112	(2c) 0.147	(2c') 0.134
d	(1d) 0.003	(2d) 0.085	(2d') 0.088

Table 3.3: Energies (in eV) of the protonic sites in the first coordination shell of Gd, relative to the most stable one ($1a$).

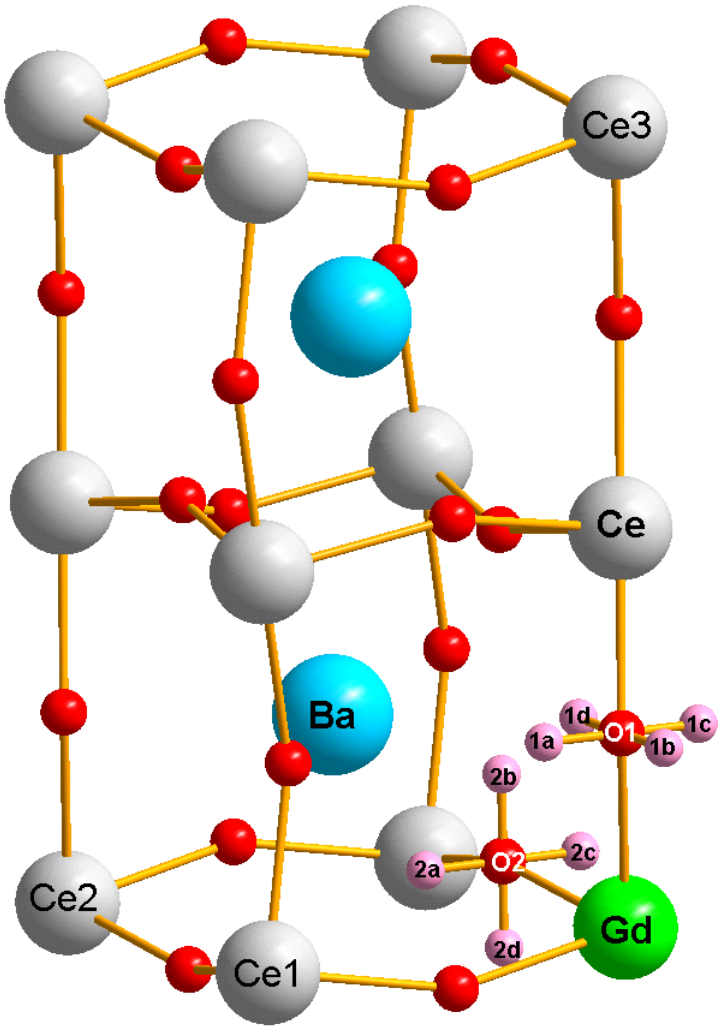

Figure 3.5: The eight possible positions for a proton bonded to an oxygen atom first-neighbor of a dopant.

Then, we examine the protonic sites beyond the first coordination shell of Gd on only two types of oxygen O1 and O2. The 8 sites shown on Fig. 3.5 near Gd are computed near Ce1, Ce2 and Ce3. Ce1 is a cerium first neighbour of the gadolinium,

Ce2 is a second neighbour and Ce3 is the furthest cerium from gadolinium that we can choose considering the size of our supercell. The energies of the 32 computed positions are plotted in figure 3.6 relative to the most stable one, 1a near gadolinium.

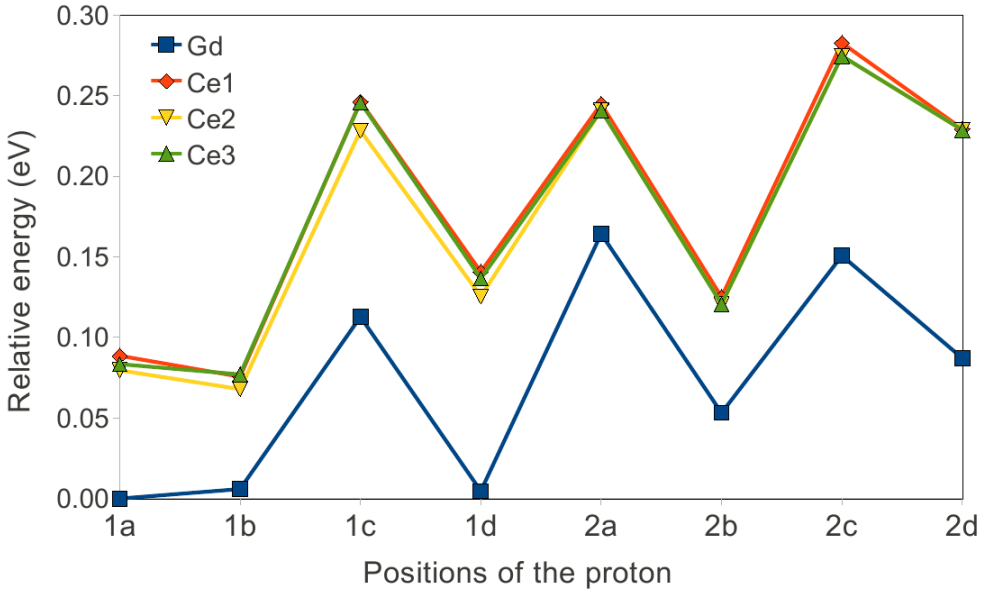

Figure 3.6: Energies of the 8 possible positions for the proton near different B-sites, relative to the most stable one (i.e. 1*a* position near Gd).

Several observations are noteworthy:

- the energy landscapes near Ce1, Ce2 and Ce3 look very much alike, suggesting that the interaction energy between gadolinium and protonic defect is confined to the oxygen 1st coordination shell of Gd.
- The energy landscape near Gd is almost a simple shift towards lower energy of an energy landscape far from Gd. The proton is more stable near Gd than far from Gd because of their opposite formal charge.
- Some positions close to Gd are, however, higher in energy than other ones far from the dopant. For instance, 2*a* near Gd is less stable than 1*d* and 2*b* far from Gd. This suggests that, under certain circumstances, protons would rather be far from Gd than close to Gd, contrary to the traditional picture in which sites close to the dopant act as traps for protons [116] .

Computations on a charged supercell of pure $BaCeO_3$ with one proton have also been carried out to check whether we recover the same relative energies for the 8 positions. We used the same cutoff of 20 Ha and the same k-point sampling of 2×2×2 than in the case of BCGO, and performed an optimisation of all atomic positions. The undoped supercell – with no gadolinium atom but one hydrogen atom inside – has a charge +1 compensated by a uniform background (or jellium) as classically done to simulate isolated charged defects. No particular correction such as Makov-Payne

or band realignment needed to be performed as we are interested in differences of total energies only.

Table 3.4 shows the energies of the 8 positions for pure $BaCeO_3$ (charged +1) and for Gd-doped $BaCeO_3$ far from the dopant. The results are almost identical, except maybe for the $2a$ position, but the difference is still below 10^{-3} Ha= 0.027 eV. This proves that we have areas free of any dopant influence in our supercell of 80 atoms, and that the site near Ce1, Ce2 and Ce3 can indeed be considered as « far » from a dopant.

Position	pure BCO	« far » BCGO
1a	0.000	0.000
1b	-0.007	-0.013
1c	0.151	0.159
1d	0.054	0.054
2a	0.162	0.141
2b	0.037	0.034
2c	0.194	0.195
2d	0.139	0.141

Table 3.4: Energies of the 8 protonic positions relative to the energy of position 1a for a charged supercell of $BaCeO_3$ and Gd-doped $BaCeO_3$,far from the dopant.

Finally, with reasonable approximations, we can distinguish only two families of sites: proton are either close to the dopant – bonded to an oxygen first-neighbour of a dopant – or not. This conclusion leads to a simplified protonic energy landscape of 16 local minima. These 16 positions will be hereafter labelled with:

- a number (1 or 2) corresponding to the oxygen type (apical and equatorial, respectively),
- a letter (« a », « b », « c » or « d ») corresponding to the O-H direction (shown in figure 3.5),
- and another letter, « n » for a site **near** the dopant, or « f » for a site **far** from the dopant.

As we did with the vacancy, we calculate an approximate dopant-proton interaction energy or association energy, by averaging (over the possible positions) the energy difference between the values around Gd and the values far from Gd, which provides -0.11 eV. This is roughly half the interaction energy between dopant and oxygen vacancy. If we consider only electrostatic interactions, this was expected as the dopant-proton interaction corresponds to the interaction of charges -1 and +1, while the dopant-vacancy interaction represents the interaction of charges -1 and +2. This value of association energy is rather low compared to the one of other materials and other dopants: for instance, Yamazaki and co-workers [117] found an association

energy of $-0.3\,\text{eV}$ in Y-doped $BaZrO_3$. This suggests that **gadolinium in $BaCeO_3$ has not a strong power of attraction on the protonic defect and constitutes a shallow trap**.

3.2.2 Hydration enthalpy

From the computations of hydrated and dry compound we can compute the hydration enthalpy, associated to reaction 3.1. This reaction can be rewritten as:

$$H_2O + BCGO_{dry} \rightarrow BCGO_{hydrated} \tag{3.2}$$

We have to take configuration with the same doping rate for the initial and final state: $\delta = 12.5\%$. We perform a calculation of the supercell with two protons and two dopants (at the same positions as for the calculation of the vacancy). Both protons are taken in their most stable position ($1a$), close to each dopant. For the oxygen vacancy, we also consider the most stable state: O1 first neighbour of the dopant. The hydration enthalpy is then simply estimated using the relation:

$$\Delta H_{hyd} = E_{tot}(BCGO_{hydrated}) - E_{tot}(BCGO_{dry}) - E_{tot}(H_2O), \tag{3.3}$$

in which $E_{tot}(BCGO_{hydrated})$ is the total energy of the (fully relaxed) supercell containing 2 dopants and 2 protons, $E_{tot}(BCGO_{dry})$ is the total energy of the (fully relaxed) supercell containing 2 dopants and one oxygen vacancy, and $E_{tot}(H_2O)$ is the total energy of an isolated water molecule.

Since the system is fully relaxed and the defects are in their most stable positions, the computed quantity ΔH_{hyd} is the hydration enthalpy at zero pressure and zero temperature.

An hydration enthalpy of $-1.34\,\text{eV}$ per H_2O molecule is found, showing that hydration of Gd-doped $BaCeO_3$ is an exothermic process, favoured at low temperature. Even if we consider less stable positions for the proton or the vacancy, we will still obtain an absolute value for the hydration enthalpy above 1 eV.

This high value is in agreement with experimental studies on acceptor-doped $BaCeO_3$ as shown in Tab. 3.5. Cerates are known to have very strong hydration enthalpy, twice as much as zirconates or stannates. Looking at this fact alone, it seems that cerates are much more interesting candidates for electrolyte. However, the protonic concentration does not depend only on the hydration enthalpy but also on the hydration entropy. Indeed the equilibrium constant K of hydration reaction (3.1), can be directly linked to standard entropy and enthalpy: $k_B T ln K = -\Delta H^0_{hydr} + T\Delta S^0_{hyd}$. Figure 3.7, from the work of Kreuer [10], shows that hydration entropy varies almost linearly with the hydration enthalpy for perovskite oxides. A high absolute value of enthalpy would be compensated by a high absolute value of entropy.

Work	B-site	Dopant	Rate(%)	ΔH_{hyd}(eV)
Present	Ce	Gd	12.5	-1.34
Ref. [118]	Ce	Gd	15	-1.78
Ref. [9]	Ce	Y	10	-1.68
	Sn	Y	50	-0.92
	Zr	Y	10	-0.78

Table 3.5: Present theoretical results compared to experimental hydration enthalpies of acceptor-doped $BaCeO_3$, with various dopants (Gd, Y). Values measured in Y-doped $BaZrO_3$ and Y-doped $BaSnO_3$ are shown for comparison.

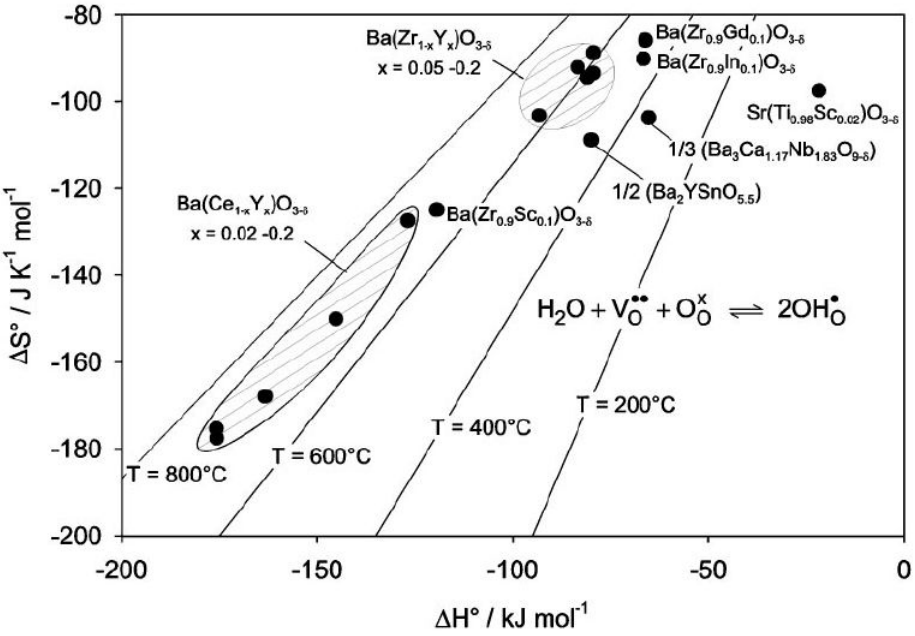

Figure 3.7: Hydration entropy and enthalpy for some protonic conductors, figure from Ref. [10]

3.3 Oxidized compound

Under an oxygen atmosphere, charged oxygen vacancies can be filled up with oxygen so that electronic defects may appear [119] according to the following process:

$$V_O^{\bullet\bullet} + \frac{1}{2}O_2 = O_O^X + 2h^{\bullet} \tag{3.4}$$

Here we study the fully oxidized state: instead of having a vacancy $V_O^{\bullet\bullet}$ for two dopants Gd'_{Ce}, there are only two dopants in the supercell, providing two holes. The charge compensation of point defect is therefore no longer fulfilled in this state. Such process would not result in an effective oxidation of metallic elements Ba^{2+},Ce^{4+} and Gd^{3+}, as they are already in their maximal oxidation state. In particular, cerium and gadolinium keep the oxidation states studied in their binary oxides in section 2.1.2,

so that they will not become problematic. But the appearance of holes may affect the electrical properties of the system and deteriorate the insulating character of the electrolyte. Therefore, this state has to be avoided to prevent a possible short circuit in devices.

3.3.1 Oxidation enthalpy

For the fully oxidized state, the oxygen vacancy has been filled up and there is no protonic defect: the only defect remaining are the two dopants. We have only one configuration to compute: dopants are put in the same positions as in the dry compound to compute the oxidation enthalpy, associated to reaction 3.4. The oxidation enthalpy for one oxygen vacancy filled is given by:

$$\Delta H_{ox} = E_{tot}(BCGO_{oxidized}) - E_{tot}(BCGO_{dry}) - \frac{1}{2}E_{tot}(O_2). \tag{3.5}$$

in which $E_{tot}(BCGO_{oxidized})$ is the total energy of the (fully relaxed) supercell containing 2 dopants and 2 protons, $E_{tot}(BCGO_{dry})$ is the total energy of the (fully relaxed) supercell containing 2 dopants and one oxygen vacancy, and $E_{tot}(O_2)$ is the total energy of an isolated oxygen molecule.

The same remarks made for hydration can be applied here: the system is fully relaxed and the defect (oxygen vacancy only) is in its most stable position, so we obtain the oxidation enthalpy ΔH_{ox} at zero pressure and zero temperature. This process is also found exothermic, as hydration, with an enthalpy $\Delta H_{ox} = -0.70$ eV per O atom. It should thus be favoured at low temperature, except if kinetically blocked.

This oxidation process has previously also been found exothermic by DFT calculations in other acceptor-doped perovskites such as barium zirconate [15, 120] and barium stannate [120]. Oxidation leads to the emergence of hole polarons and a metallic character.

Experimentally, hole conduction had indeed been observed in these materials under oxygen atmosphere, but at high temperature only. It is not measured at low temperature, the reason could be a kinetic blocking. To incorporate into the perovskite, the O_2 molecule has to dissociate at the surface and then diffuse throughout the material via oxygen vacancies. The latter process is associated to a high activation energy barrier (typically ≈ 0.8 eV), and hence requires a rather high temperature. This kinetic blocking is not observed in the case of hydration as the associated energy barrier for proton diffusion is smaller, usually around 0.4–0.5 eV.

3.3.2 Characteristic of the hole polaron

We plot the electronic density of states of the oxidized system for spin down (negative values) and spin up (positive values) for both oxidized and dry compound in figures 3.8 and 3.9. After oxidation, unoccupied states appear at the top of the valence band. This observation reflects the metallic character of the oxidized system and the appearance of holes subsequent to oxygen incorporation. The empty states have a spin up polarisation as shown by figure 3.8. Computation of the magnetic moment of the system confirms that a moment of $2\mu_B$ is missing: it is only 12 μ_B in the oxidized system while it was 14 μ_B (two gadolinium with parallel spin of 7 μ_B on each) in the dry material. Therefore, the two holes have the same spin $+\mu_B$ and constitute magnetic defects. The same magnetisation associated to hole polarons has been found in oxidized barium stannate and barium zirconate [120]).

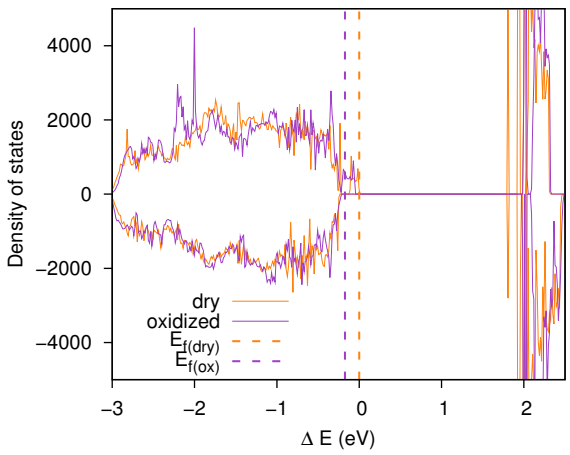

Figure 3.8: Density of state of the dry (orange line) and oxidized (green line) compounds.

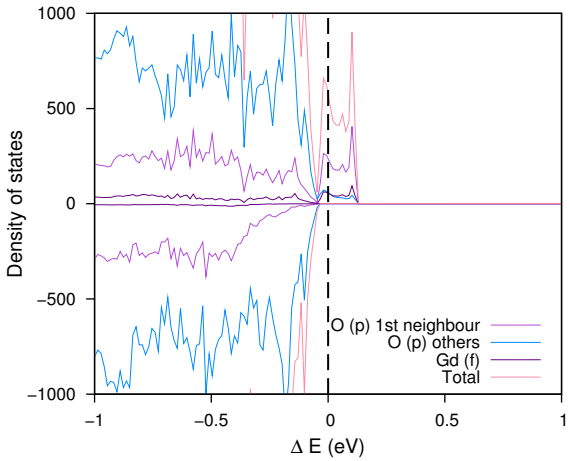

Figure 3.9: Projected density of state of the oxidized compound, on p orbitals of Oxygen and f orbitals of Gadolinium.

We now want to characterise more precisely these unoccupied states by determining where there are located, whether the hole polaron is well localised or not. In order to do so, we plot the partial density of states (projection of the density of states on different orbital momentum) for every atom. Figure 3.9 shows the projection of the DOS on the p orbitals of oxygen and the f orbitals of Gd. It distinguishes the oxygen atoms 1st neighbour of a dopant (12 atoms because there are 2 Gd in the supercell) and the oxygen atoms far from the dopants (36 atoms). It clearly evidences that the hole is mainly localised on the oxygen atoms first-neighbors of Gd, supporting the picture of a small polaron.

3.4 Competition between hydration and oxidation

Hydration and oxidation are both strongly exothermic processes. The state of the material – dry, hydrated or oxidized – depends on the thermodynamics conditions: temperature and atmosphere (pressure and content).

To check the accuracy of the enthalpy values for both processes, we run calculations with a higher cutoff, and more accurate PAW atomic data (see table 3.6). The chosen cutoff energies – 36 Ha for r_{O1} and 20 Ha for r_{O2} – are enough to get an error of 5 meV or less (far below 10^{-3} Ha= 0.027 eV), compared to higher cutoff. The soft pseudopotential we used, r_{O1}, is also enough to get accurate results, especially on the hydration enthalpy. The oxidized material being more complex, the accuracy is a little deteriorated – due to the reference O2 for which the overlap between PAW spheres is not negligible – but the error is only about 6%.

	r_{O1} E_{cut} = 36 Ha	r_{O1} E_{cut} = 46 Ha	r_{O2} E_{cut} = 20 Ha	r_{O2} E_{cut} = 30 Ha
ΔH_{hyd} (eV/$V_O^{\bullet\bullet}$)	-1.321	-1.321	-1.337	-1.332
ΔH_{oxi} (eV/$V_O^{\bullet\bullet}$)	-0.652	-0.650	-0.697	-0.692

Table 3.6: Hydration and oxidation enthalpies for different oxygen pseudopotentials and cutoff energies, to check the accuracy of our results.

From the enthalpies, we calculated grand potentials of our three states: dry, hydrated and oxidized. This allowed us to study the stability of these three phases in the simultaneous presence of oxygen and water, as done in previous studies on other proton-conducting perovskites [121–123]. This section deals with the respective stability of these three phases. The stability of BCGO (i.e. the dry compound) with respect to its chemical elements and their oxides is detailed in appendix B, using the same method of grand potential.

The grand potential is defined in a general way by

$$\Omega = E - TS - \sum_j N_j \mu_j, \tag{3.6}$$

where E is the internal energy, N_j and μ_j are respectively the number of atoms and the chemical potential of the j chemical species. The deviation of chemical potential of a species is defined as $\Delta\mu_j = \mu_j - E_j$ and the formation energy of a phase as $E^f = E - \sum_j E_j$, E_j being the internal energy of the j species in its standard phase (*i.e.* molecule O_2, body-centred cubic Ba, face-centred cubic Ce and hexagonal Gd).

The formation energies of the three phases are given in the previous chapter in table 2.13. The three grand potentials can then simply be expressed as a function of

$\Delta\mu_O$ and $\Delta\mu_{H_2O}$:

$$\Omega_{dry} = E^f_{dry} - c + \frac{\delta}{2}\Delta\mu_O \quad (3.7)$$

$$\Omega_{oxi} = E^f_{oxi} - c \quad (3.8)$$

$$\Omega_{hyd} = E^f_{hyd} - c - \frac{\delta}{2}(E^f_{H_2O} + \Delta\mu_{H_2O} - \Delta\mu_O) \quad (3.9)$$

where c is a function of $\Delta\mu_{Ba}$, $\Delta\mu_{Ce}$, $\Delta\mu_{Gd}$ and $\Delta\mu_O$, identical for each of the three compounds: $c = \Delta\mu_{Ba} + (1-\delta)\Delta\mu_{Ce} + \delta\Delta\mu_{Gd} + 3\Delta\mu_O$.

The expression of Ω_{hyd} is obtained from $\Omega_{hyd} = E^f_{hyd} - c - \delta\Delta\mu_H$, where we have replaced $\Delta\mu_H$ in order to get the dependency on $\Delta\mu_{H_2O}$, using $\Delta\mu_{H_2O} = \Delta\mu_O + 2\Delta\mu_H - E^f_{H_2O}$.

We can then plot stability domain for the three extreme states as a function of $(\Delta\mu_{H_2O}, \Delta\mu_O)$, i.e. as a function of external conditions since the chemical potentials can be directly related to the partial pressure and the temperature. For an ideal gas, we have:

$$\Delta\mu_O = \frac{1}{2}(\mu_{O_2}(T, P^0) + k_B T ln(\frac{P_{O_2}}{P^0})) \quad (3.10)$$

where P^0 is the reference pressure of 1 bar and $\mu_{O_2}(T, P^0)$ is taken from experimental values [124].

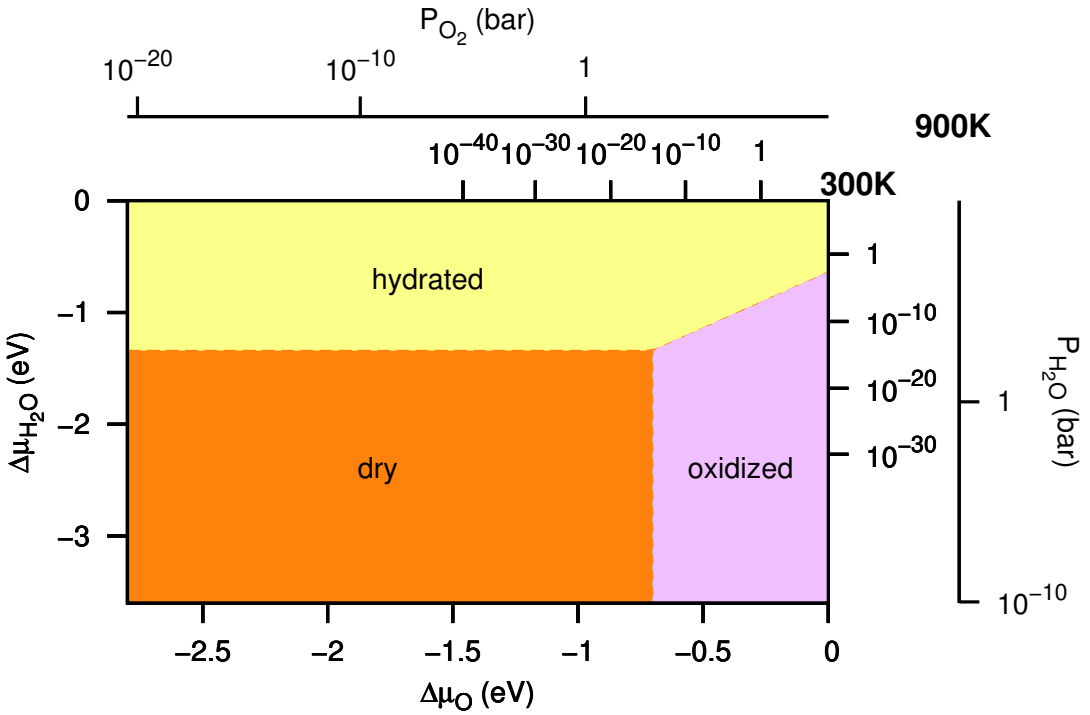

Figure 3.10: Stability of BCGO in its three phases (dry, hydrated, oxidized), as a function of $(\Delta\mu_{H_2O}, \Delta\mu_O)$. $\Delta\mu_i$ can be related either to the partial pressure P_i at fixed temperature (which is done hereabove), or to the temperature T at fixed partial pressure.

Figure 3.10 illustrates the competition between hydration and oxidation. At high oxygen partial pressure P_{O_2} , the presence of water may prevent the oxidation, and so extend the electrolyte-like behaviour. This is why the oxidized phase is probably absent in the operating conditions of fuel cells. At T=300 K, if we maintain a water pressure around 25 mbar or above, the compound should be hydrated rather than oxidized, which is in qualitative agreement with experiments (predominance of protons at low T while holes are usually dominant at high T).

However, we should remember that this stability diagram neglects the entropy (configurational and vibrational). Moreover, we only consider the extreme states: fully hydrated, fully oxidized or dry. The line delimiting the three zones in the diagram should in fact be blurry regions where the compound is partially hydrated and/or oxidized. This limit may spread over a wide range of water and oxygen partial pressures. The present approach, with its approximations, shows that **BCGO compound is likely to be hydrated at room temperature.**

Two main ideas should be remembered from this chapter:

- *due to the low symmetry of barium cerate, the protonic defects evolve in a very complex energy landscape, approximated by a structure of 16 local minima.*
- *both oxidation and hydration are strongly exothermic and thus compete, depending on the experimental conditions.*

Chapter 4

Migration barriers

Once all the stable positions for defects have been computed, we need to compute the energy barriers between each pair of neighbouring positions. First, we define the diffusion mechanisms that allow protons and oxygen vacancies to move. Then, we use the string method to compute the energy barrier between two stable positions related by a given mechanism. Finally, the results will be discussed regarding especially the agreement with Bell-Evans-Polanyi principle and with a previous study on a similar material.

Contents

4.1 Mechanisms

In the previous chapter, all stable sites for the proton and the oxygen vacancy have been extensively identified. We now have to analyse how defects move from one position to another.

4.1.1 Protonic

In a cubic perovskite, there are two kinds of processes for the proton motion: reorientation and transfer (or hopping) [29]. In this ideal structure, each process is associated to a single barrier, provided the proton is far enough from any dopant. For instance, Gomez et al. [23] found in $BaZrO_3$ (respectively $BaTiO_3$) a reorientation barrier of 0.14 eV (respectively 0.19 eV) and a transfer barrier of 0.25 eV for both materials. In such simple systems, there is only one kind of stable position for the proton (without considering the presence of a dopant for now). In this position, the proton has four possibilities to move: two reorientations and two hoppings. This possible hopping is named « intra-octahedral hopping » as both oxygens to which the proton is linked in initial and final positions belong to the same octahedron (see figure 4.1(b)).

In distorted perovskites, when there is a set of tilts of oxygen octahedra, a third mechanism may appear: the inter-octahedral hopping. Indeed, the facing oxygen, which does not belong to the same octahedron as $OH_O^\bullet$, can become very close to the protonic defect and possibly form a hydrogen bond. This mechanism is possible only for one site out of two: the cus position (a/b type) shown in figure 4.1(c). The hollow site (c/d type) is too far from the facing oxygen to be able to feel its attraction. Looking at figure 4.1(b) and 4.1(c), one interoctahedral hopping appears to be equivalent to two intraoctahedral hoppings in terms of distance. This direct jump to another octahedron might fasten the diffusion in *Pnma* structure compared to cubic perovskites.

As evoked in the introduction, many perovskites have tilted oxygen octahedra, it depends on their tolerance factor:

$$t = \frac{r_A + r_O}{\sqrt{2}(r_B + r_O)}. \tag{4.1}$$

Table 4.1 recalls the values of tolerance factor, already given in table 0.1, and the possibility of interoctahedral transfer or not according to several studies. The correlation between tolerance factor t< 1 and the *Pnma* structure is clearly evidenced, as well as the one between *Pnma* structure and interoctahedral hopping. Note however that some studies found a possible inter-octahedral transfer in small cubic perovskites

such as $SrTiO_3$ [9, 27, 28] or even in cubic perovskites with large lattice constant such as $BaZrO_3$ [125], in contradiction with other works [23, 28].

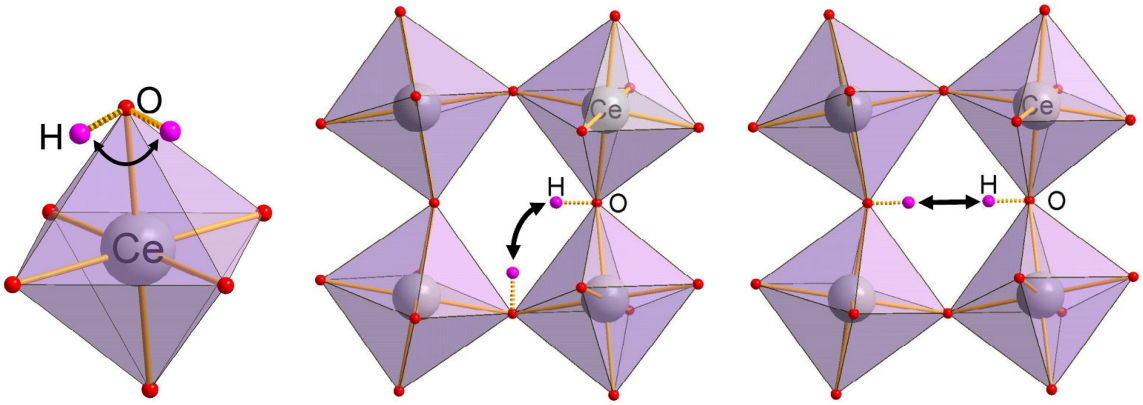

(a) Reorientation (b) Intra-octahedral hopping (c) Inter-octahedral hopping

Figure 4.1: Possible motions of the proton in a perovskite with space group *Pnma*.

Perovskite	a_0 (Å)	t	Structure	Flip	Inter	Reference
$CaTiO_3$	3.85	0.97	*Pnma*	yes	yes	[23, 27, 28]
$SrTiO_3$	3.91	1.01	$Pm\bar{3}m$ ($I4/mcm$)	yes	no	[27, 28]
$CaZrO_3$	4.04	0.92	*Pnma*	no	yes	[20–23]
$BaTiO_3$	4.06	1.07	$Pm\bar{3}m$ ($R3m$)	no	no	[23]
$SrZrO_3$	4.14	0.95	*Pnma*	no	yes	[20, 22, 26]
$BaSnO_3$	4.16	1.03	$Pm\bar{3}m$	no	no	[30]
$BaZrO_3$	4.25	1.01	$Pm\bar{3}m$	no	no	[22, 23, 29]
$SrCeO_3$	4.29	0.89	*Pnma*	no	yes	[19]
$BaCeO_3$	4.41	0.94	*Pnma*	no	yes	[19]

Table 4.1: Pseudo-cubic lattice constant a_0 from DFT calculations (GGA), tolerance factor t calculated from Shannon ionic radii, crystal space group of different perovskite oxides, and whether flip or inter-octahedral hopping can occur or not. For $BaTiO_3$ the high-temperature cubic structure is considered, which is the one simulated in Ref. [23]. The cubic structure (room temperature structure) is also considered for $SrTiO_3$, rather than the low-temperature tetragonal structure. The ground-state space group for both cases is given between parentheses.

A fourth mechanism has been mentioned in previous works, although sporadically, under different names: « flip » [126], « bending » [127] or « inter-octahedron hopping » [113]. It correspond to the situation described in section 3.2.1.1: there could be two possible positions for the protonic defect for each pseudocubic direction, slightly bend towards either neighbouring oxygen atoms (up to being aligned along the octahedra edge), instead of being equidistant from both of them. In that case, the proton can move from « bending towards one oxygen » to « bending to the other »,

staying bound to the same oxygen through a slight reorientation. That is why « interoctahedral reorientation » should be a better name for that mechanism, especially if the protonic defect $OH_O^\bullet$ is aligned along octahedron edge. This mechanism seems to only happen in perovskites with a small lattice constant (≤ 4.0 Å), as illustrated by table 4.1. The energy barrier of the flip is usually rather low ($\lesssim 0.1$ eV [113]) and hence most of the time neglected. It can also be seen as a part of the intra-octahedral transfer mechanism: before jumping from one oxygen to another, there is a little reorientation of the proton in order to get an O–H·O alignment. The intra-octahedral transfer would thus be a two-step mechanism with bending (flip) then stretching (hopping). This will be detailed later in section 4.2.1. In this work, only the three mechanisms: reorientation, intra-octahedral hopping and inter-octahedral hopping will be considered.

4.1.2 Anionic

The mechanism of oxygen vacancy are easier to list, as their sites are better defined and fewer than the possible positions of protonic defect. A vacancy can only move from one oxygen site to another, belonging or not to the same octahedron. Therefore, there are *a priori* two possible mechanisms: intraoctahedral hopping or interoctahedral hopping for oxygen vacancy.

Only few works have studied oxygen vacancy migration in such material since perovskites are usually more interesting for their protonic conduction ability. Besides, these numerical studies are usually achieved using classical molecular dynamics [128, 129], less computationally demanding, since oxygen is easier to treat with empirical potentials than hydrogen. However, the noticeable exception of Ammann et al. [130] studies both mechanisms – intra and interoctahedral transfer – in $MgSiO_3$.

4.2 Results

Once mechanisms and stable positions have been determined, the only thing remaining is the computation of the minimum energy path (MEP) using the string method described in section 1.3. These computations are using the DFT framework with the same parameters mentioned in the previous chapter (3), namely a 2×2×2 k-point grid, a 20 Ha energy cutoff, on the same 80-atom supercell. Typical simulations were done on 3000 cpu cores using four levels of parallelization: k-points, bands, FFT grid, and images.

The only two parameters needed for using the string method are: the number of images, and a convergence criterion. For all our simulations, the optimisation is

stopped when the total energy difference – averaged over all the images – between one iteration and the previous one is lower than 1×10^{-5} Ha. The number of images is trickier to choose: we first run all simulations with 10 images, and then with 19 images. For some barriers, discrepancies between both number of images were found, they will be discussed in section 4.2.1.1.

4.2.1 Energy Barrier for protonic defects

4.2.1.1 Importance of the number of images

The minimum energy path has to be correctly sampled to get the correct associated energy barrier, *i.e.* to determine the saddle point with accuracy. The number of images needed is strongly dependent on the shape of the MEP: a very smooth barrier would need few images to get the right transition state energy, while a sharp peak could need more images to be accurately described.

After all calculations with 10 images were over, we tested 19 images on some barriers[1]. It appears that for some of them we were indeed missing the real peak. Figure 4.2 shows the minimum energy path for 10 and 19 images for one smooth barrier and one sharp one. A 10-image simulation seems enough to recover perfectly a smooth path, while the sharp peak requires 19 images to find the right transition point. Consequently, all the barriers have been computed again with 19 images.

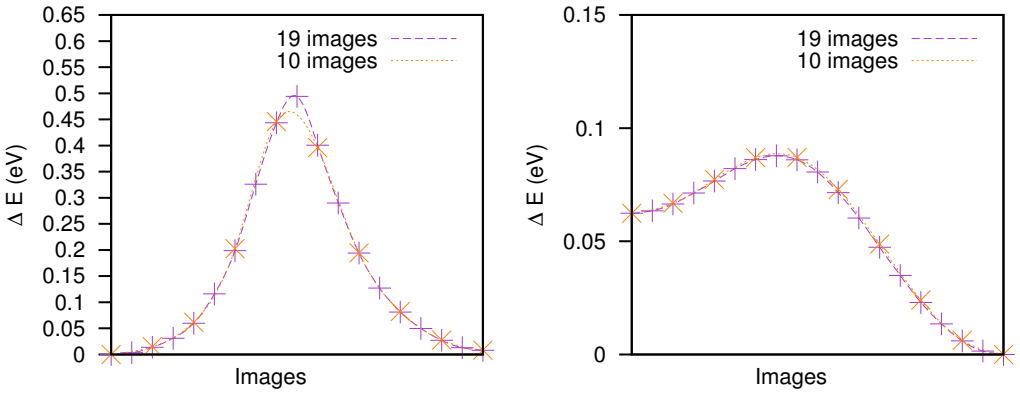

(a) Sharp path

(b) Smooth path

Figure 4.2: Examples of one sharp (a) and one smooth (b) minimum energy paths computed with 10 and 19 images.

4.2.1.2 Barrier values

Depending on the initial position, there are four or five possible mechanisms:

1. This number of 19 images was chosen to be almost the double of what we used at first. An odd number might capture a saddle point missed by an even number of images.

- if the starting site is a cus site (a/b), there are two reorientations, two intraoctahedral hoppings and one interoctahedral hopping;
- if the starting site is a hollow site (c/d), there are only two reorientations and two intraoctahedral hoppings [2].

	Reorientation				Intra				Inter	
From	To	ΔE	To	ΔE	To	ΔE	To	ΔE	To	ΔE
1an	1bn	0.50	1dn	0.10	2dn	0.37	2df	0.58	1bf	0.24
1bn	1cn	0.30	1an	0.49	2dn	0.32	2df	0.48	1af	0.24
1cn	1dn	0.05	1bn	0.20	2bn	0.29	2bf	0.43		
1dn	1an	0.09	1cn	0.16	2bn	0.36	2bf	0.52		
2an	2bn	0.31	2dn	0.15	2cn	0.22	2cf	0.40	2af	0.25
2bn	2cn	0.28	2an	0.43	1cn	0.35	1cf	0.51	2bf	0.21
					1dn	0.31	1df	0.47		
2cn	2dn	0.03	2bn	0.18	2an	0.23	2af	0.45		
2dn	2an	0.23	2cn	0.09	1an	0.29	1af	0.44		
					1bn	0.24	1bf	0.39		
1af	1bf	0.54	1df	0.14	2df	0.50	2dn	0.44	1bf	0.19
									1bn	0.16
1bf	1cf	0.33	1af	0.54	2df	0.45	2dn	0.40	1af	0.20
									1an	0.16
1cf	1df	0.06	1bf	0.18	2bf	0.36	2bn	0.32		
1df	1af	0.08	1cf	0.15	2bf	0.42	2bn	0.39		
2af	2bf	0.36	2df	0.17	2cf	0.39	2cn	0.36	2af	0.21
									2an	0.17
2bf	2cf	0.33	2af	0.49	1cf	0.47	1cn	0.42	2bf	0.16
					1df	0.44	1dn	0.39	2bn	0.13
2cf	2df	0.02	2bf	0.17	2af	0.36	2an	0.28		
2df	2af	0.20	2cf	0.08	1af	0.37	1an	0.34		
					1bf	0.31	1bn	0.28		

Table 4.2: Energy barriers (eV) for proton reorientation, intra-octahedral hopping (« intra ») and inter-octahedral hopping (« inter »).

Considering the number of stable sites and the four or five mechanisms associated to each site, we get a total of 84 values to determine. Obviously, the number of simulations to run is much smaller (around half) since most computed barriers give two values – back and forth – except for symmetric cases (for example, 2af – 2af gives only one value). Each simulation of 19 data points has then been fitted with a spline to find the minimum energy path, and thus the energy barrier. These energies are provided in table 4.2. The list presented in this table is complete provided there is

2. In that case, the interoctahedral hopping is assumed to have a too large energy barrier, owing to the very large distance separating the protonic defect $OH_O^{\bullet}$ from the facing oxygen

only one dopant considered. The only missing configurations are the one in which two dopants are 1st or 2nd neighbours. These barrier heights are given with an uncertainty of ±0.02 eV due to the approximation made in section 3.2.1.2 considering that beyond the 1st coordination shell of the dopant, a position is « far ». As shown by figure 3.6, there may be a slight energy difference between two equivalent positions « far », inducing an uncertainty on the energy barrier.

We can notice that reorientation barriers between two « near » sites or two « far » sites are similar (difference $\leqslant$ 0.05 eV). The energy surface of proton bonded to an oxygen 1st neighbour of the dopant is indeed approximately shifted by 0.1 eV compared to the surface far from the dopant (see figure 3.6). The case of hopping is more complicated though: the Coulomb interaction between H and Gd prevents hydrogen from easily escaping from the dopant. Hopping barriers from a « near » site towards a « far » sites have higher values than those of the backward motion, as expected.

Barrier	pure $BaCeO_3$		« far » $BaCeGdO_3$	
Reorientation	→	←	→	←
1a-1b	0.54	0.54	0.54	0.54
1b-1c	0.33	0.18	0.33	0.18
1c-1d	0.06	0.15	0.06	0.15
1d-1a	0.09	0.14	0.08	0.14
2a-2b	0.36	0.49	0.36	0.49
2b-2c	0.33	0.17	0.33	0.17
2c-2d	0.03	0.08	0.02	0.08
2d-2a	0.20	0.17	0.20	0.17
Hopping	→	←	→	←
1a-2d	0.50	0.37	0.50	0.37
1b-2d	0.45	0.31	0.45	0.31
1c-2b	0.36	0.47	0.36	0.47
1d-2b	0.42	0.44	0.42	0.44
2a-2c	0.39	0.36	0.39	0.36
1a-1b	0.19	0.20	0.19	0.20
2a-2a	0.21	–	0.21	–
2b-2b	0.16	–	0.16	–

Table 4.3: Comparison of barriers values “far” from the dopant in BCGO and in pure charged $BaCeO_3$.

Using an undoped supercell, as we did in the previous chapter for the stable positions in table 3.4, the barriers occurring far from the dopant have been recomputed in pure $BaCeO_3$. The charge of the proton is here compensated by a uniform charged background (homogeneous electron gas or jellium) instead of a gadolinium atom. In that simple case, an exhaustive list of the possible motions gives 30 barrier values

associated to 16 different motions: 8 reorientations, 5 intra-octahedral hoppings and 3 inter-octahedral hoppings. Table 4.3 compares these energy barriers with the one obtained in Gd-doped $BaCeO_3$, far from the dopant. The energy barriers obtained are, as expected, very close: they are identical within 0.01 eV. This corroborates, once again, that our 80-atom supercell is large enough to contain regions that are sufficiently far from the dopant to be considered as pure $BaCeO_3$. It also shows that jellium model only induces a systematic shift in total energies, and has thus no impact on energy differences.

4.2.1.3 Barrier shapes

The computation of minimum energy paths does not give only the barrier value but also the shape of the path. Figure 4.3 gives an example of energy profiles for each of the three kinds of mechanisms, as well as the evolution of the O-H distance and angle during the motion. Figure 4.3(a) illustrates a complete reorientation around an oxygen O1 near the dopant ($1an \Rightarrow 1bn \Rightarrow 1cn \Rightarrow 1dn \Rightarrow 1an$). It clearly evidences the fact that reorientation processes are not alike. In addition to very different barrier heights, the angle between two stable sites varies from 60° to 120° instead of being set to 90° (like in a cubic perovskite). It also proves that the O–H bond is never broken during a reorientation process as the O–H distance is kept constant around 1 Å.

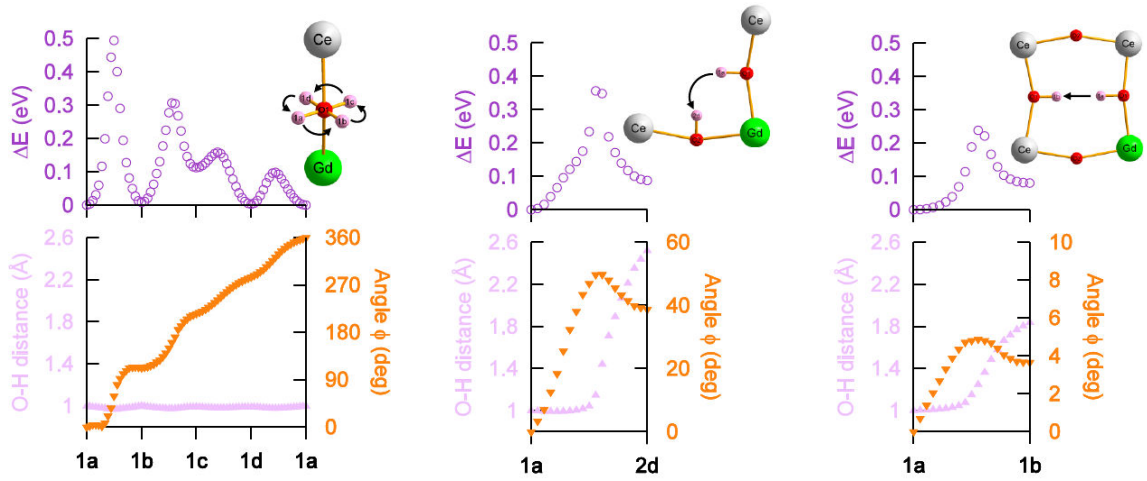

(a) Reorientation (b) Intraoctahedral hopping (c) Interoctahedral hopping

Figure 4.3: Energy profiles and evolution of the O–H distance and the angle ϕ along typical MEP. The angle ϕ is between the initial and current O–H direction (H_{init}–O–H).

Figure 4.3(b) and 4.3(c) present the same information for transfer. The evolution of the O–H distance and the angle between initial and current O–H position show that both processes are in fact two-step motions: first a reorientation in order to get

O–H–O aligned, then a jump between oxygen atoms. The reorientation is only slight for the interoctahedral hopping ($\approx 5°$) but significant for intraoctahedral hopping ($\approx 50°$). This reorientation could be related to what was previously mentioned as « flip » (see section 4.1.1).

4.2.2 Energy Barrier for oxygen vacancy

The oxygen vacancies have in fact more possibilities than the proton to move: each oxygen belongs to two octahedra and has four oxygen nearest neighbours on each octahedron leading to eight intraoctahedral transfers. Besides, there are four second neighbours enabling four interoctahedral hoppings. However, even if each oxygen vacancy has 12 possible motions, most of them are alike and should have the same barrier values. In pure $BaCeO_3$, there will be four kinds of barriers:

- two intraoctahedral hoppings: O1↔O2 and O2↔O2;
- two interoctahedral hoppings: O1↔O1 and O2↔O2.

The presence of dopant distinguishes four kinds of oxygen vacancy positions: O1n, O2n, O1f and O1f, using the same notation as for the proton: n stands for « near » the dopant and f for « far » from the dopant. This leads to 18 barrier values, presented in table 4.4.

	Intra				Inter			
From	To	ΔE	To	ΔE	To	ΔE	To	ΔE
O1n	O2n	0.64	O2f	0.62			O1f	1.10
O1f	O2n	0.33	O2f	0.57	O1n	0.90	O1f	1.12
O2n	O1n	0.59	O1f	0.48	O2f	1.14		
	O2n	0.53	O2f	0.49				
O2f	O1n	0.37	O1f	0.53	O2n	0.93	O2f	1.07
	O2n	0.31	O2f	0.39				

Table 4.4: Energy barriers (eV) for oxygen vacancy intra-octahedral hopping (« intra ») and inter-octahedral hopping (« inter »)

Contrary to the protonic case, this list is not completely exhaustive as several barriers can hide under the label « O1↔O2 » or « O2↔O2 ». Indeed, even if the initial and final position of several barriers are equivalent and the mechanisms (*e.g.* interoctahedral hopping) identical, the path to go from one type to another can slightly change because directions $\vec{a}$, $\vec{b}$ and $\vec{c}$ are not equivalent. A complete study will imply to compute the eight possible intraoctahedral and four interoctahedral hoppings for a given initial position. However, owing to the very small anisotropy in the equatorial plane (see the lattice parameters in table 2.8), the barrier values

behind « O2↔O2 » or « O1↔O2 » will probably be alike. Therefore, we decided to compute only one barrier for a given pair of initial and final positions.

The oxygen vacancy does not constitute our major focus. Their migration barrier energies are calculated to roughly know their behaviour and compare it with the protonic motion. That is why they are computed with only nine images [3]. Because of the uncertainty in energy for one given oxygen vacancy positions, all barrier values have an error bar of $\pm 0.02\,\mathrm{eV}$.

4.3 Discussion

As our main interest lies in protonic conduction, we will mainly comment on the protonic barriers, and just say a few words concerning oxygen vacancy barriers.

4.3.1 Assumptions and approximations

A few assumptions and approximations inherent to our calculations should be kept in mind when discussing the result.

First of all, the computation of energy path through the string method gives « fully-relaxed » static barriers, as opposed to « dynamical » barriers obtained in molecular dynamics though the counting of occurrences of events. Static barrier might neglect collective and recrossing effects. Besides, there is the issue of relaxing or not the whole structure. One may argue that the lattice has no time to relax instantaneously during proton hopping as the hydrogen moves quickly compared to other atoms. The computations of proton motions in unrelaxed environment would naturally lead to higher barriers (up to a factor 6 [15, 29]). But this process can be considered in a reverse way: the proton is most likely to transfer when other atoms are in specific relaxed positions – randomly happening according to their vibrations. That is why all our barriers were computed in a fully-relaxed lattice.

Secondly, quantum contributions from zero-point motions were not taken into account. This approximation is valid if the nuclei can be considered as classical particles, *i.e.* for heavy atoms and for high temperature. At the operating temperature of PCFC , this approximation may be true for barium, cerium, gadolinium and possibly for oxygen, but not for the hydrogen (the characteristic temperature associated to the stretching mode of OH is ≈ 3000–4000 K). The barrier height could be significantly decreased by proton tunnelling, by $\frac{\hbar\omega}{2} \approx 0.15\,\mathrm{eV}$. This change would principally affect

3. If the barrier is assumed to be more or less symmetric, an odd number should be more appropriate to capture the transition point, lying at mid-distance between the initial and final positions.

the transfer barrier, while reorientation barriers should not be shifted since the O–H bond is not broken during this process [64].

However, another approximation that could counterbalance this overestimation of the barrier is the generalised gradient approximation. Indeed, GGA has the tendency to overstabilise the configuration in which a proton is equally shared between two electronegative atoms [131], leading to an underestimation of the activation energy for proton transfer of 0.10 eV to 0.15 eV.

4.3.2 Comparison with In-doped $CaZrO_3$

The present study of protonic migration in Gd-doped $BaCeO_3$ can be compared with an analogous study in In-doped $CaZrO_3$ [17, 21, 132]. Both materials have the same *Pnma* structure and should thus have similar protonic energy landscapes with small differences due to different lattice parameters and tolerance factors. $BaCeO_3$ has a Goldschmidt factor of 0.94, while the one of $CaZrO_3$ is slightly smaller: 0.92. Consequently, we expect $CaZrO_3$ to be more distorted than $BaCeO_3$ whose tolerance factor is closer to one (cubic structure). Table 4.5 compares structural parameters of both materials with a fictitious ideal cubic structure. It confirms that structural distortions are smaller in $BaCeO_3$ than in $CaZrO_3$. The deviation σ on A–O and B–O bond length is due to the different distances existing in a *Pnma* structure, while there is only one in a cubic perovskite.

	$BaCeO_3$	$CaZrO_3$ [17]	cubic
a_c (Å)	4.44	4.06	–
a/a_c	1.42	1.44	1.41
b/a_c	2.00	2.00	2.00
c/a_c	1.41	1.39	1.41
$\overline{\text{A-O}}/a_c$ ($\pm\sigma$)	0.71($\pm$0.21)	0.72($\pm$0.22)	0.71
$\overline{\text{B-O}}/a_c$ ($\pm\sigma$)	0.51($\pm$0.00)	0.52($\pm$0.00)	0.50
B-O1-B (deg)	153.85	144.74	180.00
B-O2-B (deg)	156.45	145.49	180.00

Table 4.5: Structural parameters (lattice parameters, cation-oxygen distances and angles) for $BaCeO_3$, $CaZrO_3$ and a fictitious cubic perovskite.

These stronger distortions in $CaZrO_3$ should facilitate the interoctahedral hopping. On the other hand, the larger lattice parameter of $BaCeO_3$ could lower the energy barriers (the proton has more space to move). In fact, the barriers of $CaZrO_3$ are found globally higher than our values. For reorientation, we found values between 0.02 and 0.54 eV while Bilić and Gale[17] found values up to 0.89 eV. For intraoctahedral hopping, the same phenomenon is observed: our values are in the range 0.22–0.58 eV

with an average value of 0.38 eV, while transfer barriers in In-doped $CaZrO_3$ can reach 0.89 eV with an average value of 0.45 eV. The contrary is found for interoctahedral hopping, as expected considering the strong distortions of $CaZrO_3$: this process has an average value of 0.15 eV, lower than the one in $BaCeO_3$ of 0.19 eV. The smaller barrier found in interoctahedral hopping compared to intraoctahedral hopping comes from the tilting of oxygen octahedra in the orthorhombic structure. This tilt can bring two facing oxygens very close to each other while the rigidity of an octahedron will keep constant the distance between its oxygen atoms, preventing an easy intraoctahedral transfer (even though a little distortion is observed, also found in previous studies [112]).

Overall, both materials exhibit the same tendency with a very large range of possible values over almost al two orders of magnitude. The very small barrier we found in $BaCeO_3$ between c and d sites might explain why the work of Bilic and Gale consider only 7 different positions (and not eight). One of the stable site here considered, namely 1*c*, does not exist in $CaZrO_3$.

From these common observations, we can assume that all orthorhombic perovskites exhibit similar behaviour:

- rather low barriers for interoctahedral hopping ($\lesssim$ 0.2 eV) – the bigger the distortion, the smaller the barrier;
- relatively high barriers for intraoctahedral hopping ($\approx$0.3–0.6 eV);
- a very wide range of values for reorientation (from $\approx$ 0.01 eV up to nearly 1 eV)

The last thing to comment is the dopant effect: it seems harder to escape from Indium in $CaZrO_3$ than from Gd in $BaCeO_3$. If we compare the barrier to escape from the dopant to the one towards the dopant, we find a factor 3 for Indium in $CaZrO_3$, and 1.5 for Gadolinium in BCO. Dopants can have different power of attraction, as described by Björketun et al. [133] in $BaZrO_3$, according to their size and the size of A and B cation in the perovskite. This is in agreement with a recent study [134] that observed that $BaSnO_3$ possesses an ideal radius of dopant for which the proton-dopant attraction is minimal. The weak proton-dopant interaction in Gd-doped $BaCeO_3$ is a positive point and shows that the trapping effect in BCGO is weak. This suggests that gadolinium may have a nearly ideal radius in $BaCeO_3$, as yttrium in $BaZrO_3$ or indium in $BaSnO_3$.

4.3.3 Rate-limiting events

The rate-limiting or rate-determining process is defined as the slowest step in reaction. In our case, it is the slowest mechanism in the diffusion pathway. The energy barriers E_a we computed are however not enough to ascertain the frequency

of a process. Indeed, using transition state theory, the rate is given by $\nu = \nu_0 e^{-\frac{E_a}{k_B T}}$ where ν_0 is an attempt frequency to determine. A possible way, though approximate, to find this attempt frequency is to compute phonon modes in the initial and saddle point, and then use the classical harmonic approximation to transition state theory. This method will be displayed in the next chapter in section 5.1.4.2. Full phonon computations have not been carried out because of their computational cost. Some example of phonon computations in the hydrated state will be further discussed in the next chapter 5. But the attempt frequency effect on the speed of a process is secondary compared to the energy barrier effect (exponential factor). We will therefore mainly focus on the difference in barrier height.

4.3.3.1 For the proton

While a common view in cubic perovskites [135] is to consider transfer as rate-limiting and reorientation as very fast, this does not apply any more to orthorhombic structure. The reorientation does not appear to be faster than hopping in our simulations. The proton hoppings have been found to be indeed rate-limiting in $BaCeO_3$ by Münch and co-workers [19], but to be similar to reorientation in $SrCeO_3$. The activation energy value they computed for reorientation in $BaCeO_3$ is of 0.07 eV for a proton bonded to O1 and 0.11 eV for one bonded to O2, analogous to our results for the lowest barrier.

If we want to go further and include the attempt frequency in our estimations – without doing phonon calculations – we can settle for approximate values, using for instance the one found in In-doped $CaZrO_3$ by Bilic and Gale [17]. Averaging all the different value, we get a frequency ν_0 around 3000 cm^{-1} for transfer and 1000 cm^{-1} for reorientation. This allows us to compute the time scale for a process: $\tau = \nu^{-1}$. These values lead to a maximum uncertainty factor of 3 on the time scale, while the difference in barrier height can change the time scale over orders of magnitude. If we take the lowest (0.02 eV) and the highest barrier (0.54 eV) of reorientation process, the associated time scale at 900 K, for instance, are respectively 4.3×10^{-14} s and 2.1×10^{-11} s. For a hopping process with a value around 0.3 eV, the associated time scale is 5.3×10^{-13} s. Therefore the limiting process is not necessarily the hopping in general. In previous computational studies, the rate-limiting process in orthorhombic structure seems to be the intra-octahedral transfer [26], in agreement with our results. Nevertheless, the proton does not need intraoctahedral transfer to diffuse, a succession of interoctahedral hopping and reorientation is enough. In that case, the reorientation would be the rate-limiting step.

4.3.3.2 For the oxygen vacancy

Table 4.4 strikingly shows that interoctahedral hopping ($\approx 1\,\text{eV}$) is twice more costly in term of energy than intraoctahedral hopping ($\approx 0.5\,\text{eV}$), contrary to the protonic case. The oxygen vacancy will always prefer the intraoctahedral path over the interoctahedral one. In contrast to the protonic case, the final site is closer to the initial one in the case of intraoctahedral hopping than interoctahedral hopping. The same effect was previously found in a material with same *Pnma* space group: MgSiO3, by Ammann et al. [130]. However in this material with a very small lattice parameter ($a_0 = 3.5\,\text{Å}$), the diffusion barrier are higher: around 0.8 eV for intraoctahedral hopping. These large difference in both mechanisms will bring us to neglect interoctahedral hopping in the following chapter. This process is indeed not necessary as two intraoctahedral process are equivalent to a interoctahedral hopping.

4.3.4 Bell-Evans-Polanyi principle

We want to see if the set of energy barriers we get, apparently chaotic with a wide range of values, can be unified through a general relationship. We decide to confront our results to a concept, very useful in physical chemistry: **Bell-Evans-Polanyi principle**. It states that there might be a linear relation between the barrier height E_a of similar chemical processes and their reaction enthalpy ΔH [136, 137]:

$$E_a = E_a^0 + \alpha \Delta H, \tag{4.2}$$

E_a^0 is a reference barrier height for a class of processes and α is a a constant between 0 and 1, supposedly close to 0.5 [137]. The value of 0.5 can be recovered by assuming a parabolic form for the potential energy surface with the same curvature in initial and final positions, and finding the crossing point along a reaction coordinate.

This principle is illustrated on figure 4.4: starting from an identical initial position, the higher energy the final position has (ΔH), the higher energy the transition point has (E_a).

This principle reflects the intuitive fact that if a reaction becomes more exothermic, the activation energy decreases, while if it becomes more endothermic, the activation energy will increase.

Does this principle applied to our defects? This principle has first been observed by Bell [136] in the case of proton transfer, and then by Evans and Polanyi [137] in the more general case of chemical reactions of type A + BC = AB + C. It is thus expected to apply pretty well in the case of proton hopping, while it is not clear whether it should apply to oxygen vacancy or not. The trick is always to define precisely what exactly means « similar processes ».

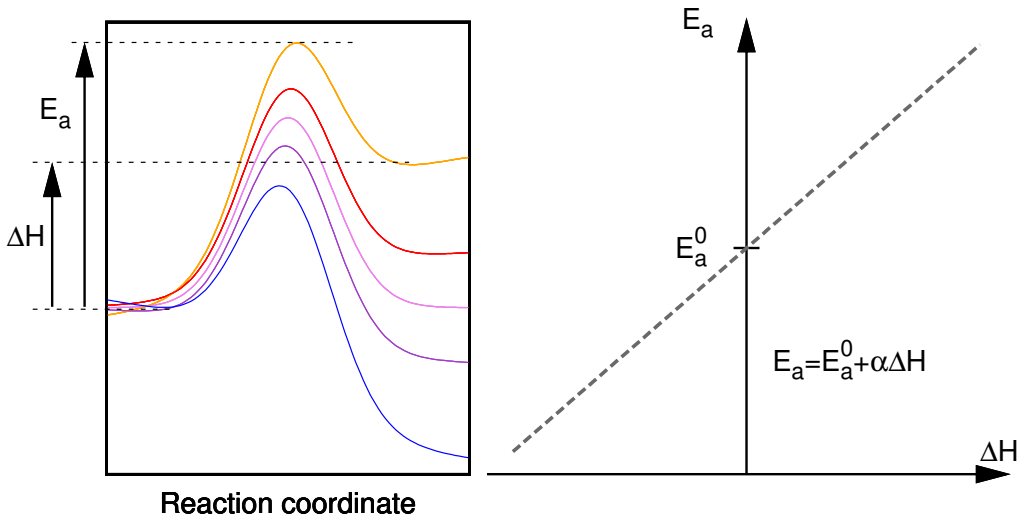

Figure 4.4: Illustration of the Bell-Evans-Polanyi principle: enthalpy profile along a reaction coordinate for similar processes (left), evolution of the activation energy (or barrier height) as a function of the reaction enthalpy (right).

4.3.4.1 For the proton

In order to see if the BEP principle applies to our energy barrier, we have to plot the activation energy as a function of the enthalpy reaction for a set of similar processes. In our case, what is called « activation energy » in BEP principle corresponds to the the barrier height, and the « enthalpy reaction » is in fact an energy reaction – since our computations are performed at constant volume – it is simply the energy difference between the final and initial positions. We will keep the notation E_a for the energy barrier in the following (and not ΔE like in previous sections) in order to avoid confusion with the energy difference between final and initial positions, which will be noted ΔE (replacing ΔH in BEP principle).

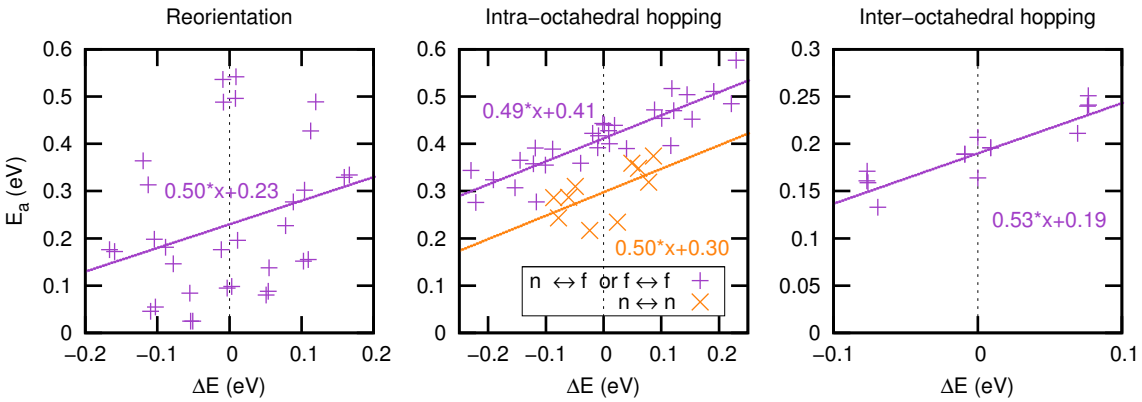

Figure 4.5: Activation energy versus reaction energy of protonic barrier for the three kinds of mechanisms.

The first idea is to separate the three mechanisms in three different plots presented in figure 4.5 with a linear fit. Since intra-octahedral hoppings occurring around a dopant (n↔n) have activation energy significantly lower than other transfers, we chose to plot them apart.

Several comments can be made about this figure:

- first of all, the reorientations do not obey Bell-Evans-Polanyi principle at all, there is no correlation between ΔE and the energy barriers E_a. This is not surprising considering the fact that a reorientation is not a true chemical process: the bond between oxygen and hydrogen is not broken during this mechanism.
- On the other hand, BEP principle seems to apply reasonably well to both types of transfers.

For the inter-octahedral transfer, the linear fit is rather good and give a reference energy E_a^0 of 0.19 eV.

If we take a closer look at barrier values for proton transfers of table 4.2, especially intra-octahedral hoppings , all the energy barriers satisfy, for every pair of initial and final positions (i, j), the inequalities:

$$E_a(in \to jn) < E_a(if \to jn) < E_a(if \to jf) < E_a(in \to jf). \tag{4.3}$$

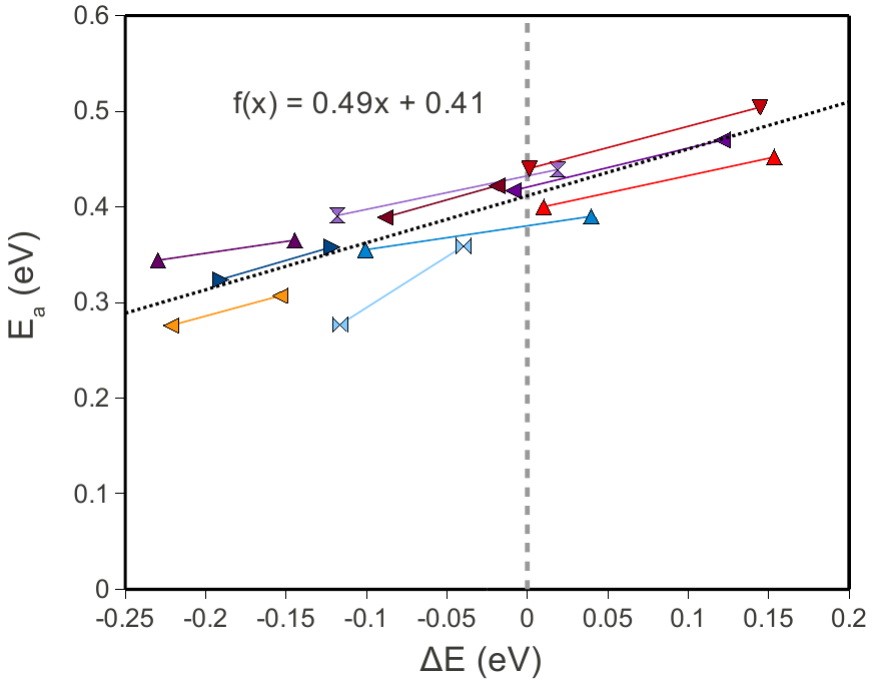

Figure 4.6: Activation energy E_a as a function of reaction energy ΔE for intra-octahedral transfer considering only two processes per category: $if \to jn$ and $if \to jf$. The dashed line is a linear fit of all the data.

The middle inequality of equation 4.3 is simply the characterisation of BEP principle if we restrict the meaning of « similar processes » to processes between same

types of positions. In that case, we consider only two barriers per class: $if \rightarrow jn$ and $if \rightarrow jf$. Figure 4.6 shows the BEP plot for the 10 different class of intra-octahedral transfer. This choice ensures that the processes are really « similar »: they start from the same initial position if and arrive to a position low in energy near the dopant jn or high in energy, far from the dopant jf. Since there is only two processes per class, we can hardly claim that there is a linear relation between activation energy and reaction enthalpy. However, we can note, that the activation energy is indeed always higher for a mechanism $if \rightarrow jf$ than for $if \rightarrow jn$, and the slope between this two points is very close to 0.5 for every class. Hence, BEP principle is very well satisfied for intra-octahedral transfer, with an energy reference of 0.41 eV and a factor α of 0.49.

The last inequality of equation 4.3 can also be understood through BEP principle: the energy differences between n-type and f-type positions are usually higher than between two f-type positions, leading to a higher activation energy.

Concerning the intra-octahedral hopping of type $in \rightarrow jn$ shown in figure 4.5, the linear fit is not very good but a global increase of E_a as a function of ΔE is evidenced.

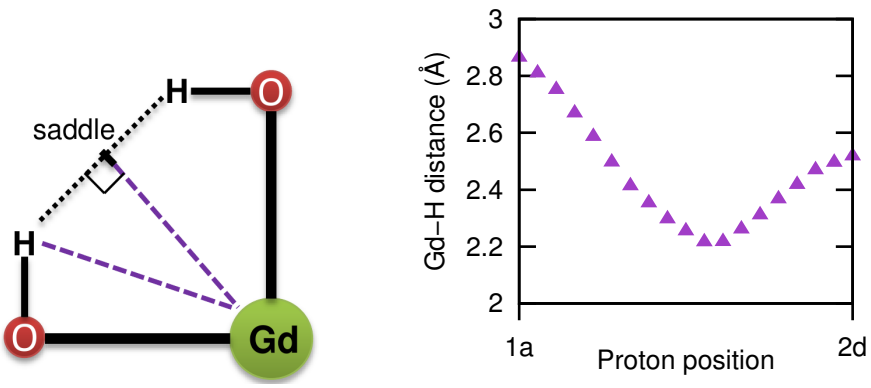

(a) Simple representation (b) Computed values

Figure 4.7: Distance between gadolinium and hydrogen during an intra-octahedral mechanism close to the dopant.

The fact that all barriers near a dopant ($in \rightarrow jn$) are lower than barriers far from a dopant ($if \rightarrow jf$) – as implied by the inequalities 4.3 – can be justified with very simple geometric considerations. Since there is almost a simple shift in energy between positions « near » and « far » from the dopant, one could expect the energy barriers to be almost identical. But if we consider the saddle point for an intra-octahedral transfer (shown in figure 4.7), assuming the transfer is simply a straight line between initial and final positions, it appears that it is closer to the dopant than the initial and final positions. It is confirmed if we look at the evolution

of the Gd-H distance during an intra-octahedral transfer near Gd: figure 4.7(b) proves that, at the transition point, the distance is indeed shorter than in initial and final states. By simple electrostatic considerations, we can infer that the saddle point is more stabilised than the initial and final positions, leading to a lower energy barrier.

Note that the value of α – found to be nearly 0.5 in all cases – is to be considered with caution: there is an artefact due to the fact that most barriers give two points on the graphic: one for the forward motion, one for the backward motion (except for barrier between two identical sites such as « 2b↔2b »). Indeed, if we consider a barrier between state A and state B, we will extract two pairs (ΔE, E_a). If we note E_A, E_B and E_t, the energies of the initial, final and transition point respectively, we have $\Delta E_1 = E_B - E_A$, $\Delta E_2 = E_A - E_B$, $E_{a1} = E_t - E_A$ and $E_{a2} = E_t - E_B$. Therefore, the slope of the line joining both points (ΔE, E_a) is given by:

$$\frac{E_{a1} - E_{a2}}{\Delta E_1 - \Delta E_2} = \frac{E_B - E_A}{2(E_B - E_A)} = 0.5. \tag{4.4}$$

However, the values of E_a^0 are perfectly meaningful and give a good average energy for each kind of mechanism. Moreover the value of figure 4.6 are free from this artefact. E_a^0 is an intrinsic energy barrier, the one that is obtained when the initial and final positions have the same energy. Protonic inter-octahedral transfers ($E_a^0 \approx$ 0.19 eV) are favoured (when possible, *i.e.* when the initial and final protonic sites are made closer by the octahedral tilts) over intra-octahedral hoppings (excluding $n \to n$) ($E_a^0 \approx 0.41$ eV). The intra-octahedral transfer close to dopants ($n \to n$) is also favoured, with a low energy barrier of ≈ 0.30 eV.

4.3.4.2 For the oxygen vacancy

If we plot the activation energy versus the reaction enthalpy for intra-octahedral and inter-octahedral transfers in figure 4.8, we see that the fit is not as good as the protonic one. Because of the previously mentioned artefact, we also find a value of $\alpha \approx 0.5$ for both mechanisms. The intrinsic energy barrier is found to be 0.48 eV for the intra-octahedral hopping and much higher, with a value of 1.06 eV for the inter-octahedral hopping. For the intra-octahedral case, the points are very scattered: this suggests that either the BEP principle does not apply or these processes can not be considered as « similar ».

In order to see if we can define other categories of processes, we draw the same plot as figure 4.6 for the oxygen vacancy (see figure 4.9): each segment correspond to a couple of barriers ($if \to jn$,$if \to jf$).

Even if the common tendency is less clear than for the protonic case, we recover the part of inequality 4.3 corresponding to the BEP principle for every type of barriers:

$$E_a(if \to jn) < E_a(if \to jf). \tag{4.5}$$

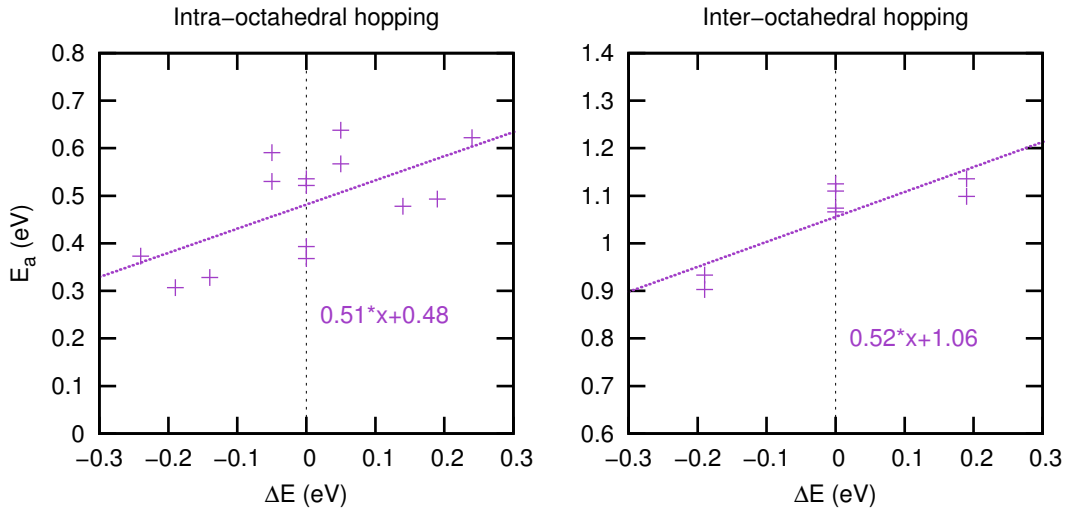

Figure 4.8: Activation energy versus reaction energy of oxygen vacancy barrier for the two kinds of mechanisms.

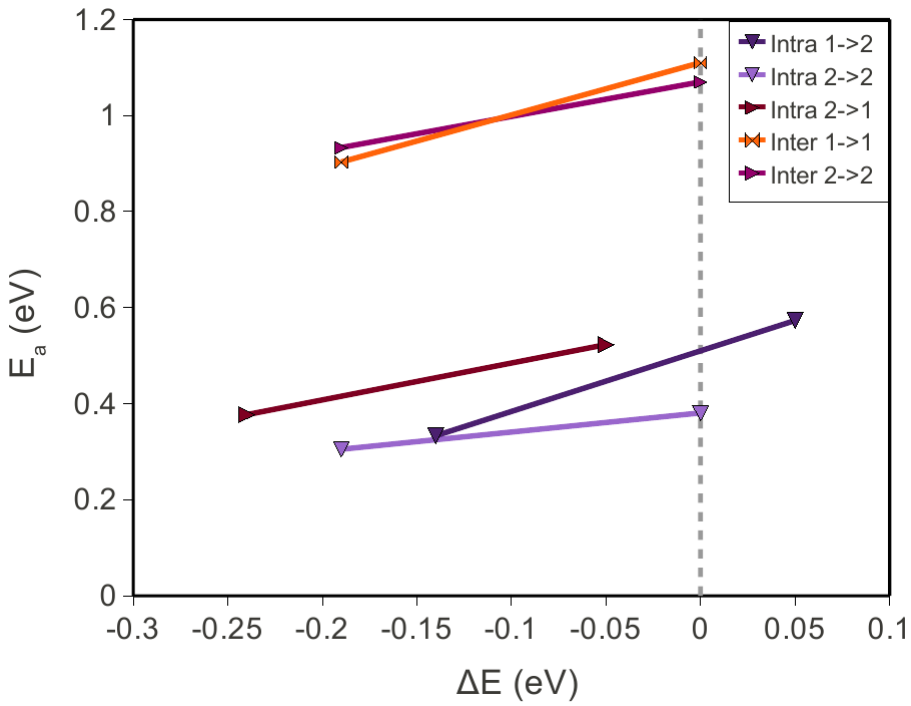

Figure 4.9: Activation energy E_a as a function of reaction energy ΔE for intra-octahedral and inter-octahedral transfer considering only two similar processes per category: $if \rightarrow jn$ and $if \rightarrow jf$.

Nevertheless, the coefficient α is close to 0.75 and not 0.5 and the values are much scattered. But the BEP principle seems to apply if we use the restricted notion of « similar » processes.

We do not recover however the first part of inequality 4.3. On the contrary, the energy barriers near a dopant($n \rightarrow n$) are found to be higher than the barriers

far from a dopant ($f \rightarrow f$). This can however be explained with exactly the same argument: during an oxygen vacancy migration, it is in fact an oxygen atom that is moving. This oxygen atom is formally charged -2 and will thus be subject to an electrostatic repulsive force from the dopant. This repulsive force is stronger for the saddle point since, it is closer to the dopant than initial and final positions (path analogous to the one of a proton in figure 4.7(a)).

In other words, **the oxygen vacancies diffuse less easily in the vicinity of a dopant, whereas protons diffuse more easily in the vicinity of a dopant.**

The fact that BEP principle does not apply perfectly to oxygen vacancy was somehow expected. Indeed, the reaction involved during an oxygen vacancy migration does not correspond to a simple bond breaking and reformation, while protonic transfers exactly match the conditions in which BEP principle was formulated.

All the intrinsic energy barrier values E_a^0 for both kinds of defects are summarised in table 4.6.

Defects	Mechanism	E_a^0 (eV)
Proton	Reorientation	–
	intra-octahedral hopping (without n↔n)	0.41
	intra-octahedral hopping (only n↔n)	0.30
	inter-octahedral hopping	0.19
Oxygen vacancy	intra-octahedral hopping	0.48
	inter-octahedral hopping	1.06

Table 4.6: Intrinsic energy barrier E_a^0 for the different diffusion mechanisms of protonic defects and oxygen vacancies.

The energy landscape of defects is much more complex in the orthorhombic structure than in cubic structure. The picture of a two-step Grotthus diffusion with a fast reorientation followed by a slow transfer [9] does not apply to our material. The reorientation, usually considered as very fast, could be in fact a limiting process here. The interoctahedral process seems to be the more efficient in hydrogen diffusion. On the contrary, for oxygen vacancy, only the intraoctahedral transfer should be considered.

All these barriers will be used as an input for the Kinetic Monte-Carlo algorithm in the following chapter.

Chapter 5

Diffusion and conduction

From all computed barriers in DFT, we want to extract a global activation energy, and to study the influence of the dopant concentration on this activation energy and on the diffusion coefficient.

Kinetic Monte-Carlo is particularly well-fitted to study a succession of events with very different transition rates, as in our case. It allows us to access macroscopic quantities using ab initio results.

Contents

Kinetic-Monte Carlo (KMC) algorithm needs very few input parameters: the main one is the transition rate for every process, modelled by:

$$\nu = \nu_0 e^{-\frac{\Delta E}{k_B T}}. \tag{5.1}$$

The definition of the transition rate given by equation 5.1 implies three parameters: the attempt frequency ν_0, the barrier height ΔE and the temperature T. The barrier heights correspond to the results of the previous chapter, the temperature can vary from one simulation to another, and the choice of the attempt frequency will be discussed in section 5.1.4.

In order to perform KMC simulations, a code has been written following the algorithm described in section 1.4.1 (chapter 1). Considering our implementation, other physical parameters can be modified in the input file: the supercell size, the dopant concentration, the proton concentration (level of hydration), the number of KMC steps, and the value of a possible applied external electric field in each direction.

5.1 Assumptions and choices

Most of the KMC computations have been performed using a $8 \times 8 \times 8$ supercell (in terms of pseudo-cubic unit cells) with periodic boundary conditions in the three directions. The compound is assumed to be either:

- dry : $[V_O^{\bullet\bullet}]=\frac{1}{2}[Gd'_{Ce}]$ and $[OH_O^{\bullet}]=0$,
- or fully hydrated : $[OH_O^{\bullet}]=[Gd'_{Ce}]$ and $[V_O^{\bullet\bullet}]=0$,

though mix of protonic defects and oxygen vacancies are possible regarding our code.

Two types of simulations were performed:

- without external electric field,
- under an external electric field.

Both types allow to access diffusion properties such as the activation energy by computing directly the diffusion coefficient (without external electric field) or through calculations of the defect mobility (under an electric field).

In order to get enough statistics to get a perfect fit, the number of steps was fixed to 10 millions KMC steps for simulations without external electric field, and 200 000 steps for simulations under an external electric field. This difference is justified by the fact that Brownian motion is predominant when there is no electric field leading to a lot of noise on the protonic mean square displacement, while an external electric field forces the proton to mainly move along it, causing a tremendous reduction of the noise. Depending on the temperature and the dopant concentration, 10 millions KMC steps can represent 30 ns to 1 ms in real time. The lower the temperature and the lower the doping rate, the longer the simulation time.

5.1.1 Assumptions on non-computed cases

Ab initio computations of BCGO always assumed that dopants are far from each other. Configurations in which two dopants are neighbours have not been computed. Therefore, our KMC simulations are valid at low doping rates. Indeed, as the doping rate increases (higher than 12.5% typically), the number of neighbouring gadolinium atoms increases as well. The transition state of a defect between two different dopants could be more stabilised and the stable sites as well: this « overtrapping » effect has not been computed in DFT, as it drastically multiplies the number of configurations to simulate.

To treat the configurations with neighbouring dopants, we made two assumptions in the case of a transition between two oxygen octahedra belonging to two different dopants:

- energy of the stable sites (initial and final positions) are identical to the one of a near region,
- the barrier height is the same as the one from a « near » site to a « far » site.

With these assumptions, we do not take into account the extra stabilisation induced by a pair of dopants contrary to Björketun et al. [29], and may thus underestimate the trapping effect at high doping rate.

5.1.2 Detailed balance principle

Due to the uncertainty on position energy (around 0.01 eV), computed barriers between two positions A and B does not necessarily obey the detailed balance relation explained in section 1.4.2:

$$E_A - E_B = \Delta E_{B\to A} - \Delta E_{A\to B}. \tag{5.2}$$

To remedy this issue, we slightly modified the barriers, so that equality 5.2 is strictly respected for every couple of positions (A,B). Whenever this equality was not true, we chose an average transition point with an energy of

$$E_{saddle} = \frac{1}{2}\left[(E_A + \Delta E_{A\to B}) + (E_B + \Delta E_{B\to A})\right] \tag{5.3}$$

and modified both barriers $\Delta E_{A\to B}$ and $\Delta E_{A\to B}$ accordingly. Following this process, all barriers were not modified by more than 0.008 eV, far below the error bar.

5.1.3 Ab initio computation of $BaCeO_3$ dielectric tensor

In this chapter, we will sometimes need the knowledge of the static dielectric constant of BCO: $\varepsilon^{\mathrm{BCO}}$. It will be requires in section 5.2.2, dedicated to the inco-

pora incorporation of electrostatic interaction between charge point defects, and section 5.3.2 treating the response to an external electric field.

Therefore, we computed the value of $\varepsilon^{\mathrm{BCO}}$ in DFT using the same exchange-correlation functional as previous calculations. In order to get this value, we performed Density Functional Perturbative Theory (DFPT) calculations [40, 138, 139], still using ABINIT code, but with norm-conserving Troullier-Martins pseudopotentials for Ba, Ce and O. Simulations were performed on a 20-atom primitive cell of BCO using a plane-wave cutoff of 60 Ha.

From these simulations, we can access to the electronic dielectric tensor $\varepsilon^{\infty}_{\alpha\beta}$, the phonon modes at the Γ point of the Brillouin Zone and the atomic Born effective charge tensors. Using these quantities, we can recover the static dielectric tensor $\varepsilon^{\mathrm{BCO}}_{\alpha\beta}$ in the harmonic approximation:

$$\varepsilon^{\mathrm{BCO}}_{\alpha\beta} = \varepsilon^{\infty}_{\alpha\beta} + \frac{4\pi}{\Omega}\sum_{\tau}\frac{S^{(\tau)}_{\alpha\beta}}{\omega^2_{\tau}}, \tag{5.4}$$

in which τ is the index of phonon modes at Γ point, $S^{(\tau)}$ is the mode-oscillator strength tensor of mode τ (deduced from the Born effective charges and phonon eigendisplacements), ω_{τ} is the phonon pulsation of mode τ and Ω is the unit cell volume.

We finally get the static dielectric constant with:

$$\varepsilon^{\mathrm{BCO}} = 1/3(\varepsilon^{\mathrm{BCO}}_{xx} + \varepsilon^{\mathrm{BCO}}_{yy} + \varepsilon^{\mathrm{BCO}}_{zz}) = 31.45. \tag{5.5}$$

5.1.4 Attempt frequency

5.1.4.1 First approximations of the prefactor

Once we have the energy barrier ΔE, the only remaining input parameters are the attempt frequencies associated to each process. Most of our computations simply used the prefactor $\nu_0 = 1 \times 10^{13}\,\mathrm{Hz}$, known to be a typical atomic vibration frequency in a crystal. This frequency is also a good average value of vibrational frequencies found for protons in perovskites [140]. This first set of prefactors, the same for every process, is labelled « **set 1** ». However this is only a rough approximation, that associates to every mechanism the same attempt frequency.

To go beyond this approximation, we should perform phonon computations, but these simulations are very costly and could not be done for each single configuration (stable site and saddle point). We will discuss these computations in the next section (5.1.4.2), but they do not give an exhaustive list of frequency for each process. However, we can use results from previous studies on similar materials: in a first time, we can try two different frequencies for hopping ($\nu_0 = 3000\,\mathrm{cm}^{-1}$) and reorientation

($\nu_0 = 1000\,\mathrm{cm}^{-1}$). This distinction comes from the fact that reorientation is based on a bending mode while hopping is based on a stretching mode [29]. This choice of prefactors is hereafter noted **« set 2 »**. Finally a third set (**« set 3 »**) of attempt frequencies can be chosen, noticing that intra-octahedral hopping are initiated by the activation of a bending mode, as shown in figure 4.3(b) in the previous chapter. It gives us the same two attempt frequencies but not for the same process: $\nu_0 = 3000\,\mathrm{cm}^{-1}$ for inter-octahedral hopping and $\nu_0 = 1000\,\mathrm{cm}^{-1}$ for reorientation and intra-octahedral hopping, in good agreement with phonon computations performed in an analogous material: In-doped $CaZrO_3$ [17].

Results obtained with these both sets would be discussed in section 5.2.3 and compare with the result obtained for the unique frequency of test 1.

The three choices of set for atomic frequencies are summed up in table 5.1.

Mechanism	Reorientation	Intra hopping	Inter hopping
Set 1	$333\,\mathrm{cm}^{-1}$	$333\,\mathrm{cm}^{-1}$	$333\,\mathrm{cm}^{-1}$
Set 2	$1000\,\mathrm{cm}^{-1}$	$3000\,\mathrm{cm}^{-1}$	$3000\,\mathrm{cm}^{-1}$
Set 3	$1000\,\mathrm{cm}^{-1}$	$1000\,\mathrm{cm}^{-1}$	$3000\,\mathrm{cm}^{-1}$

Table 5.1: Attempt frequencies ν_0 associated to each mechanism for the three sets tested.

In all cases, since the attempt frequencies of a given mechanism and the one of the reverse process are the same, the detailed balance relation is still obeyed.

5.1.4.2 Phonon computations – Transition state theory

Some phonon computations have also been performed in the same DFPT formalism, still using norm-conserving Troullier-Martins pseudopotentials (see section 5.1.3). Due to the very high computational cost, phonon calculations have been fully performed for only two protonic configurations in pure $BaCeO_3$ on a 40-atom supercell (with compensating charge background): one in a stable site (« 2c ») and one in a saddle point (« 2b–2b »). Other calculations of perturbation theory have been performed on some other configurations, but only looking at the linear response of the proton (the perturbations corresponding to atomic displacements of the other atoms are not considered). The obtained frequencies with that partial method are therefore approximate and should be taken with caution. Table 5.2 presents these calculations and compare the obtained frequencies with full-computations for the configuration « 2c » and « 2b–2b ». It appears that performing a full-computation only slightly changes the values of phonon frequencies, therefore a partial computation – applying perturbations only on the proton – is sufficient to recover very good values. Moreover,

phonon frequencies are alike for every stable position, especially for positions belonging to the same group « cus » or « hollow » type. Saddle positions for transfers seem to have the same frequency even if the mechanism implied is not the same, while a saddle point of reorientation gets very different values, as expected considering the fact that the O–H bond is not broken.

Proton positions	Phonons frequencies (cm^{-1})		
Stable positions			
1a	631	1169	3130
1d	699	885	3292
2b	669	1235	3037
2c	683	885	3303
2c (full)	696	900	3405
2d	732	930	3245
Saddle positions			
1c–1d reo	1038	3446	
1a–2d intra	1279	1615	
2b–2b inter	1161	1613	
2b–2b inter (full)	1183	1622	

Table 5.2: Phonon frequencies calculated from partial and full phonon computations « (full) » (only highest frequencies are shown in this case) for some stable sites, and for a saddle point for each mechanism.

Using the harmonic transition state theory (see section 1.4.2.2), we can compute the prefactor ν_0 :

$$\nu_0 = \frac{\prod_{i \in initial}^{n} \nu_i}{\prod_{i \in saddle}^{n-1} \nu_i}. \tag{5.6}$$

Using this equation and the values of table 5.2, we get the following values: $\nu_0 = 569\,cm^{-1}$ for reorientation, $1117\,cm^{-1}$ for intra-octahedral hopping and $1339\,cm^{-1}$ for inter-octahedral hopping. This results are close to the set 2 of frequencies we tested, despite the factor 2. Indeed, they show that both types of hopping have very close attempt frequencies while reorientation gets a much lower frequency.

5.2 Test of the methodology and the code

5.2.1 Canonical distribution recovered

In order to test our KMC implementation, we run long trajectories without external electric field: as explained in section 1.4.2, we should recover the canonical distribution when the system reaches equilibrium. Occupation probabilities were

extracted from the computations through the formula:

$$n_i^{occ} = \frac{1}{N_i^{sites}} \frac{\overline{N}_i}{N_{tot}} \tag{5.7}$$

where N_i^{sites} is the total number of sites of type i, N_{tot} is the total number of protons in the simulation, and $\overline{N}_i$ is the mean number of proton on sites of type i. n_i^{occ} is the mean fraction of protons per site of type i, it is related to the energy of site i: $n_i^{occ} \propto e^{-\frac{E_i}{k_B T}}$ for a given total number of protons. The ratio of site occupations is thus given by:

$$\frac{n_i^{occ}}{n_j^{occ}} = e^{-\frac{E_i - E_j}{k_B T}} \tag{5.8}$$

From these site occupations, we can thus recover the relative energies (the most stable positions, $1an$, is chosen as reference), using:

$$-k_B T \ln\left(\frac{n_i^{occ}}{n_{1an}^{occ}}\right) = \Delta E_i \ = (E_i - E_{1an}). \tag{5.9}$$

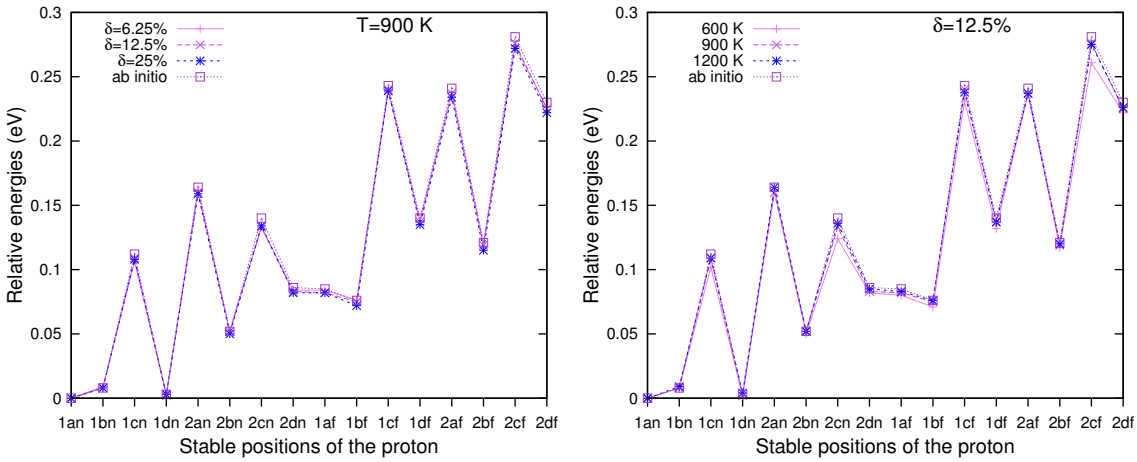

(a) Fixed temperature

(b) Fixed doping rate

Figure 5.1: Relative energies of the 16 stable protonic site from KMC simulations compared with *ab initio* values.

Figure 5.1 compares these relative energies at a fixed temperature for three doping rate: 6.25%, 12.5% and 25% (panel a) , and at a fixed doping rate of 12.5% for three temperatures : 600, 900 and 1200 K (panel b), with *ab initio* values. All the curves are a lot alike proving that all the sites are occupied with the correct probability during the KMC trajectory whatever the doping rate and the temperature. We can see that at the lowest temperature of 600 K, the agreement between the KMC curve and the DFT reference is slightly less perfect (especially for the high energy positions $2c$), this may suggest that a longer equilibration time is needed since the probability to get over a high barrier is very small.

If we look at the occurrences of the 84 kinds of events during a simulation, each of them happens at least a thousand times even in the worst case scenario with few protons and a low temperature. Moreover, we checked the distance travelled by a proton: after 10 millions KMC steps, the root mean square displacement $\sqrt{\langle r^2 \rangle}$ is at least of 70 Å (up to thousands Å) meaning that the proton has crossed at least twice the supercell boundaries (of length $8 \times 4.44\,\text{Å} = 35.52\,\text{Å}$).

Both these observations confirm that the proton is actually exploring all the positions, and that our simulation really consider long-range protonic diffusion. This is probably related to the fact that gadolinium acts as a rather shallow trap (the association energy is only of $-0.1\,\text{eV}$).

5.2.2 Influence of electrostatic interactions between charged point defects

In this section, we want to check, at least in a rough way, what we are missing when assuming no electrostatic interaction between charged defects. The *ab initio* barriers already contain the electrostatic interaction between one proton and one dopant (and their periodic images). However, in our KMC simulations, without adding an electrostatic interaction term, we cannot describe accurately space-charge regions (for instance, an inhomogeneous repartition of dopants or an accumulation of protons). In our simulations, we assume a uniform (random) distribution of defects. However, it is still useful to test the electrostatic interactions between defects because it will take into account the proton-proton repulsion, expected to lower the diffusion coefficient, and the pair of dopants, which could strengthen the trapping effect.

We will only deal with a fully-hydrated compound in this section (no oxygen vacancy in the material). Gadolinium (Gd'_{Ce}) and proton ($\text{H}_i^\bullet$) are seen as point defects with charge -1 and $+1$ respectively in a matrix of $BaCeO_3$ of permittivity $\varepsilon^{\text{BCO}} (\approx 30)$. Since we have periodic boundaries conditions in the three direction in our supercell, we used the Ewald summation method to compute the electrostatic potential at every position $\vec{r}$. (The electric field that derives from this potential is hereafter noted $\vec{E}_{def}$). We modified the energy barrier by adding the electrostatic potential at the saddle point minus the electrostatic potential at the transition point for every mechanism. However, one strong interaction is already taken into account in the DFT computation: the Gd-H attraction. For KMC calculations including electrostatic interactions, we thus used a modified set of barriers: we remove the electrostatic part of this attraction from all barriers involving a « near » site. This typically provides a decrease for « n→f » barriers of 0.04 eV and an increase of « f→n » barriers of 0.03 eV.

Ewald summation requires the static dielectric constant (previously computed in section 5.1.3) and three parameters:

- the Ewald parameter σ which determine the range separation and is usually related to the length of supercell through the equation $\sigma = \frac{L}{\sqrt{2\pi}}$,
- the highest vector in real space $\vec{n}_max$ used to compute the short-range part,
- the highest vector in reciprocal space $\vec{k}_max$ used to compute the long-range part.

We used the usual value of $\sigma = \frac{L}{\sqrt{2\pi}}$, and tried different couples ($\vec{n}_max$, $\vec{k}_max$). It appeared that the lowest possible value of these vectors: (1,1,1) is enough to recover an accuracy on Ewald energy better than 10^{-6} eV (with a sum up to vector (2,2,2) we find an accuracy of 10^{-12} eV). This implementation was tested through the computation of Madelung constant in sodium chloride NaCl.

Ewald summation has to be computed at every KMC step for all protons and possible transition states: this increases drastically the computational cost ($\approx$ 200 times higher, depending on the number of protons). Figure 5.2 presents the mean square displacement at 1200 K for a doping rate of 6.25% with and without long-range electrostatic interactions. It appears that the diffusion coefficient is reduced (by 14%) as expected considering the proton-proton repulsion. However, further computations showed that the activation energy is not affected by these electrostatic interactions.

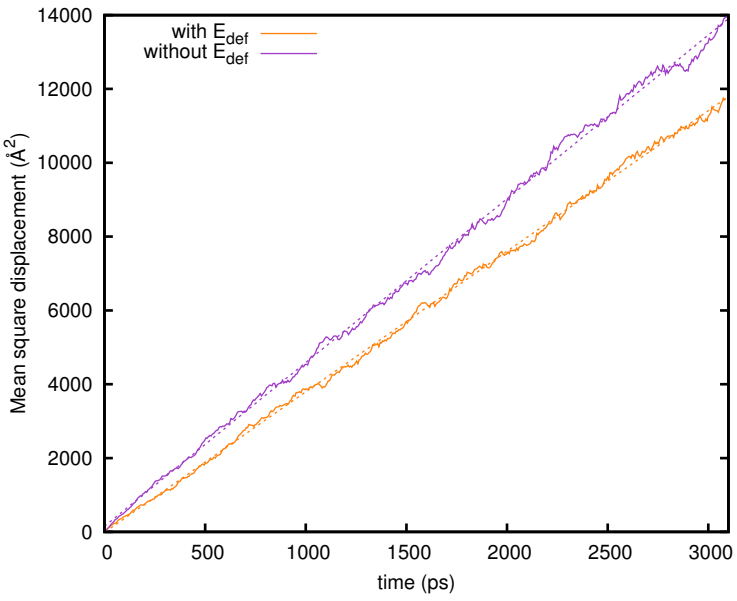

Figure 5.2: Long-range electrostatic interactions effect on the mean square displacement evolution for proton.

Considering the high computational cost due to Ewald summation, we will not take into account these interactions in the following sections.

The consideration of long-range interactions improves the accuracy of our model but elastic deformations due to the presence of several hydrogen are still missing. We cannot see a phenomenon described by Bork et al. [141] in which two protonic defects may attract each other through elastic deformation of the lattice.

5.2.3 Influence of the prefactor

We now test the three sets of attempt frequencies mentioned in section 5.1.4. In figure 5.3, we can see that the three sets give the same slope (logarithm of diffusion coefficient as a function of $\frac{1}{T}$) and so the same activation energy of 0.36 eV (for a fully-hydrated system with $\delta = 12.5\%$). The method to find the activation energy is described hereafter in section 5.3.1. The diffusion coefficient is naturally affected: almost one order of magnitude smaller for the set 1 compared to both other sets, as expected since the transition rates are also ten times smaller.

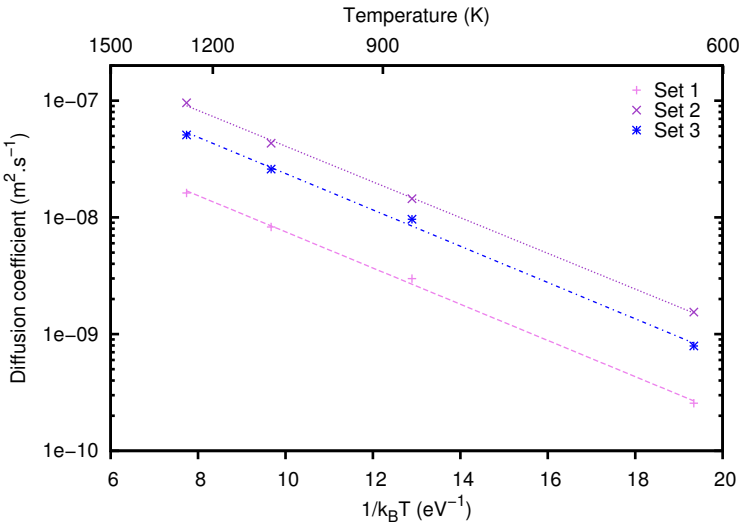

Figure 5.3: Arrhenius plots of proton diffusion coefficient for the three different set of attempt frequencies.

It appears that the choice of the attempt frequency is not of prime importance: it only induces a rescaling of the diffusion coefficient, but does not affect the activation energy. In the following, we will simply use the first set, $\nu_0 = 10^{13}$ Hz whatever the mechanism, for both kinds of defects.

5.3 Diffusion coefficient and defect mobility

Using the parameters and hypothesis mentioned above, we run KMC simulations either in the fully hydrated compound to study protonic motion, or in the dry compound to study oxygen vacancy diffusion.

In a first time, we run computations without external electric field to study the diffusion of protons and oxygen vacancy in BCGO . This allows to compute the diffusion coefficient, the mobility and the activation energy for different doping concentration. However, we also wish to test a method in which an external field is directly applied. This is an alternative way to get the defect mobility that could be extended to the study of non-linear effects in strong electric fields. In this section, the attempt frequencies are fixed to $\nu_0 = 10^{13}$ Hz for both the protonic defect and the oxygen vacancy.

5.3.1 Diffusion coefficient

Protonic defects and oxygen vacancies obey to a Brownian law when no external force is applied. Their mean square displacement is given by:

$$\langle r(t)^2 \rangle = 6Dt, \tag{5.10}$$

where $\langle r(t)^2 \rangle$ is the square of the distance between the position at $t = 0$ and the position at time t, averaged over all the protons of the simulation cell, and D is the diffusion coefficient.

Plotting $\langle r^2 \rangle$ as a function of time allows to calculate the diffusion coefficient. Finally, from an Arrhenius fit of the diffusion coefficients at different temperatures, we can extract the global activation energy E_a:

$$D = D_0 e^{-\frac{E_a}{k_B T}} \tag{5.11}$$

Note that the defect mobility μ can be recovered from the diffusion coefficient by $\mu = \frac{qD}{k_B T}$ where q is the charge of the defect.

5.3.1.1 Protonic diffusion

KMC computations were conducted for different temperatures between 500 K and 1500 K, and for different doping rates $\delta = 1/32$, $1/16$,$1/8$, $1/5$ and $1/4$. Considering the size of our supercell, the number of protons is 16, 32, 64, 108 or 128 respectively. We also performed some simulations in a bigger supercell $12 \times 12 \times 12$ for the lowest dopant concentrations, in order to get a better statistic (*e.g.* 54 protons instead of only 16).

For a given temperature and a given doping rate, four trajectories are computed and averaged to plot $\langle r(t)^2 \rangle$ and find the associated diffusion coefficient. The logarithm of D is plotted in figure 5.4 as a function of inverse temperature. Using equation 5.11, we can extract the activation energy E_a. It is found to have a value around 0.37 eV and to be rather independent of the doping rate, especially at low dopant concentration.

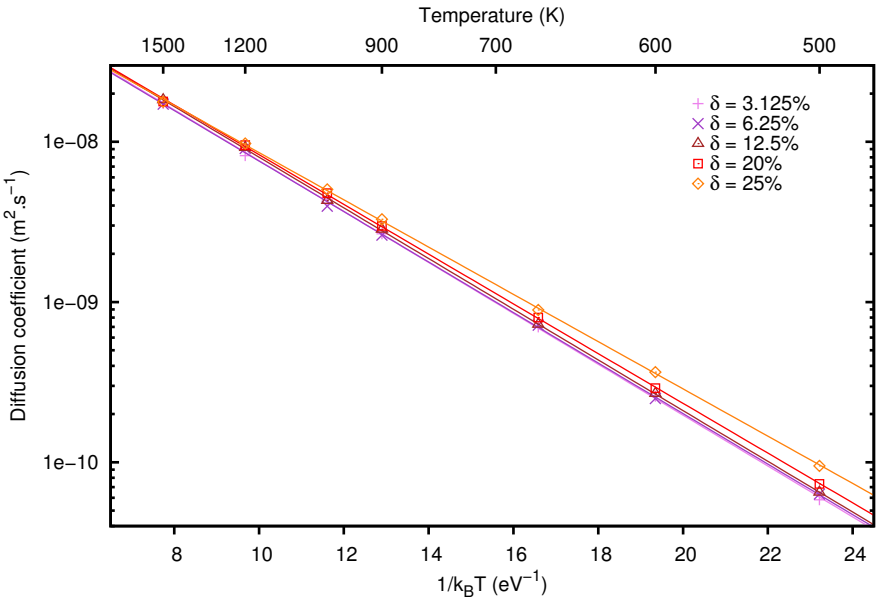

Figure 5.4: Arrhenius plot of the diffusion coefficient of protons as a function of dopant concentration.

At higher doping rate, namely 20% or 25%, the activation energy seems to decrease, with values of 0.357 and 0.340 eV respectively. But our approximations are less valid at high doping rate since DFT computations only treated the case of a proton in the neighbourhood of one dopant. At high dopant concentration, the probability of having two dopants near a proton increases. The assumptions we made in section 5.1.1 to treat these cases of several neighbouring dopants may underestimate the trapping effect of pairs of dopants. Therefore, the results for $\delta = 20\%$ or 25% should be considered with caution.

δ (%)	E_a (eV)
3.125	0.366
6.25	0.363
12.5	0.364
20	0.357
25	0.340

Table 5.3: Activation energy for protonic diffusion from KMC simulations performed with different doping rates.

δ (%)	E_a (eV)	Reference
5	0.46	[142]
10	0.45	[143]
10	0.52	[142]
15	0.56	[142]
20	0.56	[142]
30	0.55	[142]

Table 5.4: Activation energy of $BaCeO_3$ for different Gd doping concentrations, from published experimental results.

Table 5.3 shows the values of activation energy for doping rates $\leqslant 12.5\%$. Experimental values, shown in table 5.4, are found around 0.5 eV (note however that the data from Ref.[142] include oxide ion conductivity and not only protonic conductivity). This discrepancy might be explained by the approximations we made

(GGA-PBE, no quantum correction), and especially the use of static barriers instead of dynamical barriers, but also by the fact that we only consider fully-hydrated materials while experiments deal with partially hydrated materials containing many oxygen vacancies. These vacancies are obstacles to the diffusion of protons since they suppress possible oxygen sites for the proton and possess a charge +2 (repulsive for the proton). Even at low temperature, it has been found that full hydration is never reached: in Y-doped $BaCeO_3$, the maximum possible hydration is around 15% lower than the theoretical maximum [106], probably because of partial occupation of Ba-sites by yttrium dopants.

5.3.1.2 Anionic diffusion

We performed the same kind of simulations in the dry compound, which contains one oxygen vacancy for every two dopants. Using the Arrhenius equation 5.11, we can extract the activation energy. Arrhenius plots for different dopant concentrations are shown in figure 5.5.

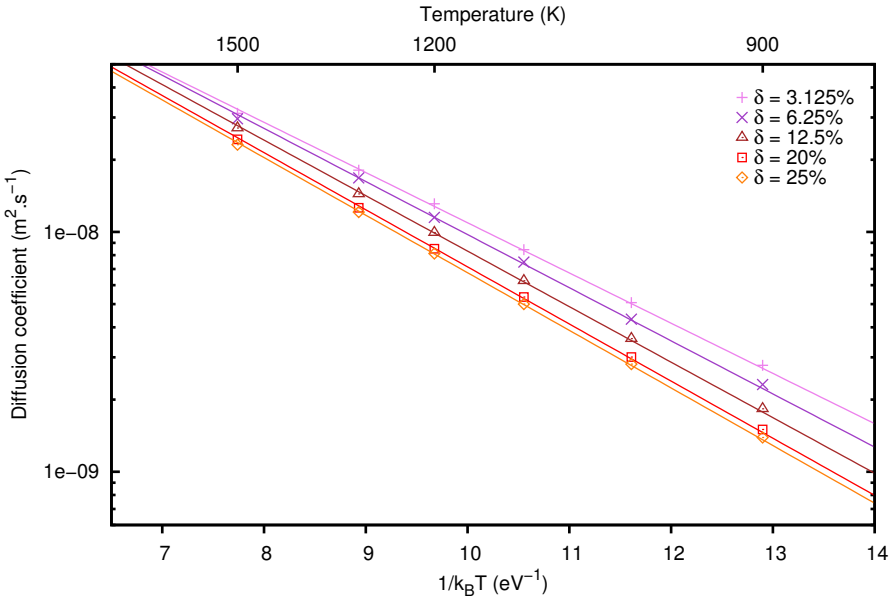

Figure 5.5: Arrhenius plot of the diffusion coefficient of oxygen vacancies as a function of doping concentration.

Contrary to the protonic case, the doping rate has a strong influence on the activation energy of oxygen vacancies (see table 5.5). The higher the doping rate, the higher (in absolute value) the activation energy. This behaviour characterises a strong trapping effect of dopants on the oxygen vacancy. This difference in behaviour between both defects was expected since the interaction energy between dopant and oxygen vacancy is twice higher as the one between Gd'_{Ce} and $H_i^{\bullet}$, and above all, the energy landscape for oxygen vacancy is much simpler. Indeed, there are only two

sites « near » and two sites « far » for the oxygen vacancy and both « near » sites have a lower energy than both « far » sites, while for the proton, some « near » sites are in fact higher in energy than other « far » sites.

δ (%)	E_a (eV)
3.125	0.482
6.25	0.510
12.5	0.533
20	0.548
25	0.553

Table 5.5: Activation energy for oxygen vacancy diffusion from KMC simulations performed with different doping rates.

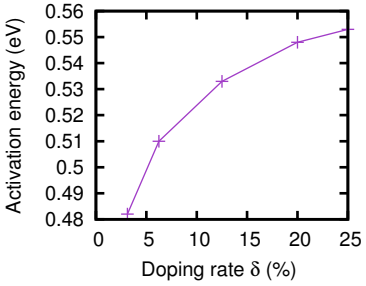

Figure 5.6: Activation energy of oxygen vacancy as a function of the dopant concentration.

These values of activation energies for the oxygen vacancy might explained the high experimental values found in table 5.4, which included oxygen ion conductivity. Furthermore, the values found are in agreement with what was previously found in other perovskites materials. Table 5.6 give some examples of activation energy found in other perovskites by molecular dynamics simulations.

Material	E_a (eV)	Reference
$LaMnO_3$	0.86	[128]
$LaCoO_3$	0.61	[128]
$LaFeO_3$	0.50	[128]
$LaCrO_3$	0.48	[128]
$LaGaO_3$	0.73	[129]

Table 5.6: Activation energy from previous molecular dynamics computations for some perovskites.

5.3.2 Simulations under finite external electric field

The previous KMC simulations performed without external field allow to get the diffusion coefficient D and the mobility μ using the relation $\mu = \frac{qD}{k_B T}$. In the present section, we propose a model to get access to the same quantities by simulations using an external (finite) electric field. Such computations provide directly the mobility μ and thus indirectly the diffusion coefficient D using the reverse relation $D = \frac{\mu k_B T}{q}$. The proposed model is described in section 5.3.2.1 and the results for protonic and anionic mobility are shown in sections 5.3.2.2 and 5.3.2.3 respectively. In particular,

we show that the diffusion coefficient we get are identical to the one computed in the previous section by more conventional KMC simulations.

5.3.2.1 Methodology

(a) KMC procedure

A mobile charge feeling a finite electric field E obeys the Nernst-Einstein law:

$$\vec{v} = \mu\vec{E} \quad \text{or} \quad \langle x \rangle = \mu E t \tag{5.12}$$

where μ the mobility of the species. This relation is valid in a linear response approach, *i.e.* in the limit of weak electric fields. The mobility μ is defined with respect to the field actually felt by the charge.

We now have to include the finite electric field E felt by the charge in the KMC procedure. We adopt the method used by Pornprasertsuk et al. [49] and Modak and Lusk [144]: for a given process, the energy barrier without field, ΔE is replaced by

$$\Delta E - q\vec{E} \cdot \vec{\Delta r}, \tag{5.13}$$

where $\vec{\Delta r}$ is the position vector separating the saddle position from the stable one. The prefactors are not modified. this approach can be justified by assuming a local equilibrium around the defect and considering that the energy landscape felt by the defect is the microscopic energy landscape without external field plus the electrostatic potential energy associated to $\vec{E}$ ($\vec{E}$ should be in fact considered as the supplement of electric field induced by the external field).

Figure 5.7 shows the effect of a constant electric field on a simple energy landscape (one dimension with only one kind of barrier). Both dashed lines in the right figure represent the limit of the simulated box: while periodic boundary conditions are applied to the system, the electric potential can not respect these conditions (it would induce a discontinuity).

(b) Electric field felt by the defects

If we consider that the defects do not interact with each other, nor with the host matrix, the electric field felt by the defect is simply the external field. In that case, the electric field $\vec{E}$ introduced in the previous section correspond to both the external electric field $\vec{E}_{ext}$ and the local electric field felt by the defect $\vec{E}_{loc}$.

However, in a dielectric medium, the local field and the external field might differ significantly. This is important if one wants to compute the conductivity from mobility values. Indeed, the mobility is defined according to equation 5.12 with respect to the local field felt by the charge, while the conductivity σ is defined with respect to the external electric field: $\vec{j} = \sigma\vec{E}_{ext}$. The relation between the mobility

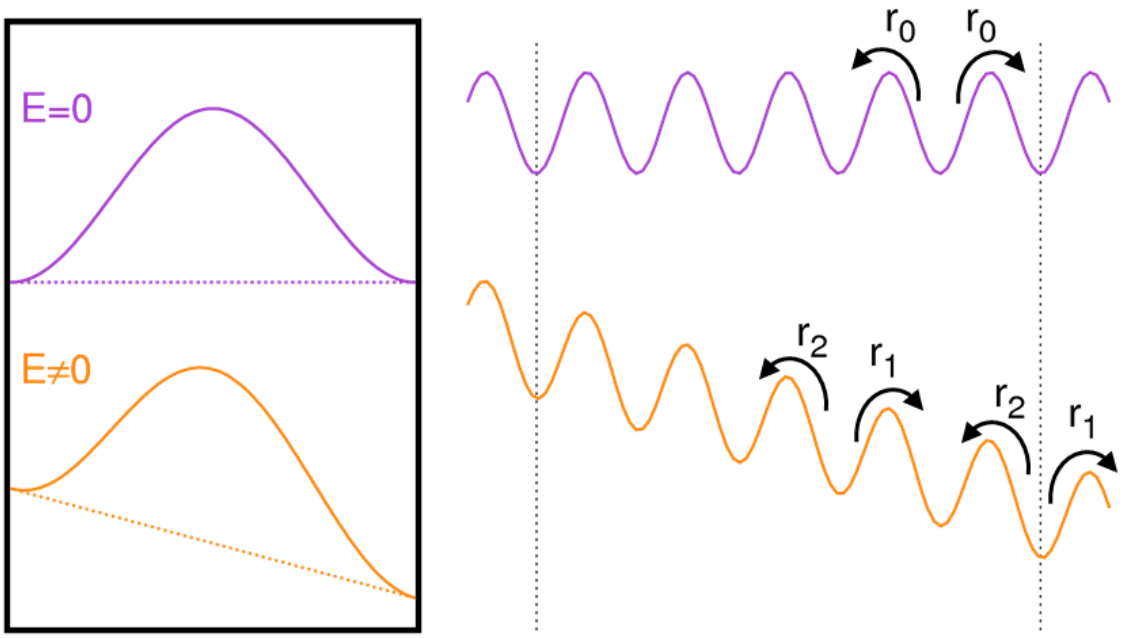

Figure 5.7: Effect of a constant electric field on a simple energy landscape with only one barrier. The transition rate r_0 without external field become two different transitions rates r_1 and r_2 when applying an external electric field, with the relation: $r_2 < r_0 < r_1$.

and the conductivity might thus be different than the usual relation $\sigma = qn\mu$ (n being the defect concentration) which assumes an equality between both electric fields. In fact, the expression of the electric current density $\vec{j} = qn\vec{v} = qn\mu\vec{E}_{loc}$ leads to the relation between conductivity and mobility:

$$\sigma = qn\mu_{eff}, \text{ where } \mu_{eff} = \mu\frac{E_{loc}}{E_{ext}}. \tag{5.14}$$

The local field $\vec{E}_{loc}$ must include the contribution coming from the surrounding matrix that become polarised by application of $\vec{E}_{ext}$. It is linked to the polarisability (and so to the dielectric permittivity) of the host material ($BaCeO_3$). It is usually divided in two terms $\vec{E}_2 + \vec{E}_3$, where $\vec{E}_2$ is called the Lorentz field [72] and is expressed with the induced polarisation by: $\vec{E}_2 = \frac{\vec{P}}{3\varepsilon_0}$. $\vec{E}_3$ is the field created by the dipoles inside the Lorentz cavity and is equal to zero in a cubic environment. Making this approximation and using $\vec{P} = \varepsilon_0(\varepsilon^{\mathrm{BCO}} - 1)\vec{E}_{ext}$, we get:

$$\vec{E}_{loc} = \vec{E}_{ext} + \frac{\vec{P}}{3\varepsilon_0} = \frac{\varepsilon^{\mathrm{BCO}} + 2}{3}\vec{E}_{ext} \tag{5.15}$$

The electric field felt by a charged defect is in fact the macroscopic field rescaled by a factor $\frac{\varepsilon^{\mathrm{BCO}}+2}{3} = 11.15$. Using equation 5.14, we can see that the conductivity is underestimated by a factor 11.15 if we assume the electric field and the external field are identical.

Neglecting the Lorentz contribution is equivalent to set $\varepsilon^{\mathrm{BCO}} = 1$ and thus $\vec{E}_{loc} = \vec{E}_{ext}$. Note that the mobility is the same whether we neglect this contribution or not, since it can be defined without the intervention of any electric field, from the diffusion coefficient: $\mu = \frac{qD}{k_B T}$. Accounting for Lorentz term, however, has effects on the conductivity, whose expression explicitly includes a contribution from the dielectric constant. The computation of σ involves the defect concentration, that we do not know (the protonic concentration depends on the H_2O partial pressure, and the oxygen vacancy concentration on the O_2 partial pressure). We will only present a fictitious maximal conductivity σ_{max} assuming a full hydration, expected to be close to the real conductivity at low temperature and high water pressure.

We can also add the interactions between charged defects $\vec{E}_{def}$, as described in section 5.2.2. The local field will simply become:

$$\vec{E}_{loc} = \vec{E}_{def} + \frac{\varepsilon^{\mathrm{BCO}} + 2}{3}\vec{E}_{ext}. \tag{5.16}$$

Owing to the computation cost, this last case will not be treated.

Since the noise due to Brownian motion is relatively smaller when an electric field is applied, the mobility (and so the diffusion coefficient) can be obtained with shorter trajectories – 200 000 KMC steps is usually enough – and with a better accuracy than when no external force is applied. We checked that we recover the results of the previous section 5.3.1 concerning the diffusion coefficient. This verification also confirms that our implementation of electric field is correct.

Moreover, we can choose the direction of the applied electric field in order to study the **anisotropy** of conduction and diffusion in Gd-doped $BaCeO_3$. This is also possible without applying an electric field but it requires much longer trajectories with a very big supercell to compensate for the noise.

5.3.2.2 Protonic

We tried different values of local electric field from 0.005 up to $0.05\,\mathrm{V\,Å^{-1}}$, which correspond to external electric field (or macroscopic field) of $4.5 \times 10^6\,\mathrm{V\,m^{-1}}$ to $4.5 \times 10^7\,\mathrm{V\,m^{-1}}$. These fields are close to the one applied by Pornprasertsuk et al. [49] ($E = 7 \times 10^5\,\mathrm{V\,m^{-1}}$) or Modak and Lusk [144] ($E = 6.79 \times 10^7\,\mathrm{V\,m^{-1}}$) on YSZ.

We first applied an electric field along the x-axis on a supercell doped with 12.5% of gadolinium. Here, we used the pseudo-cubic direction x,y and z: using the orthorhombic notations, x and y are the pseudo-cubic direction in the plane (ac) (only transfer between equatorial oxygens are possible in that plane) while z correspond to the direction of axis b (along which are the apical oxygens).

Using equation 5.12, and plotting the mean displacement versus time ($\langle r \rangle = v \times t = \mu E t$), we can extract the protonic mobility. Figure 5.8 confirms that the

mobility is not dependent of the value of the electric field – showing that we remain in the linear part of the electric response – but strongly temperature dependent. We get a protonic mobility around $5 \times 10^{-9}\,\mathrm{m\,s^{-2}\,V^{-1}}$ at 600 K, $35 \times 10^{-9}\,\mathrm{m\,s^{-2}\,V^{-1}}$ at 900 K and $82 \times 10^{-9}\,\mathrm{m\,s^{-2}\,V^{-1}}$ at 1200 K. The order of magnitude of our results is in agreement with the experimental value of $30 \times 10^{-9}\,\mathrm{m\,s^{-2}\,V^{-1}}$ obtained in Y-doped $BaCeO_3$ (10%) [145] at 1173 K.

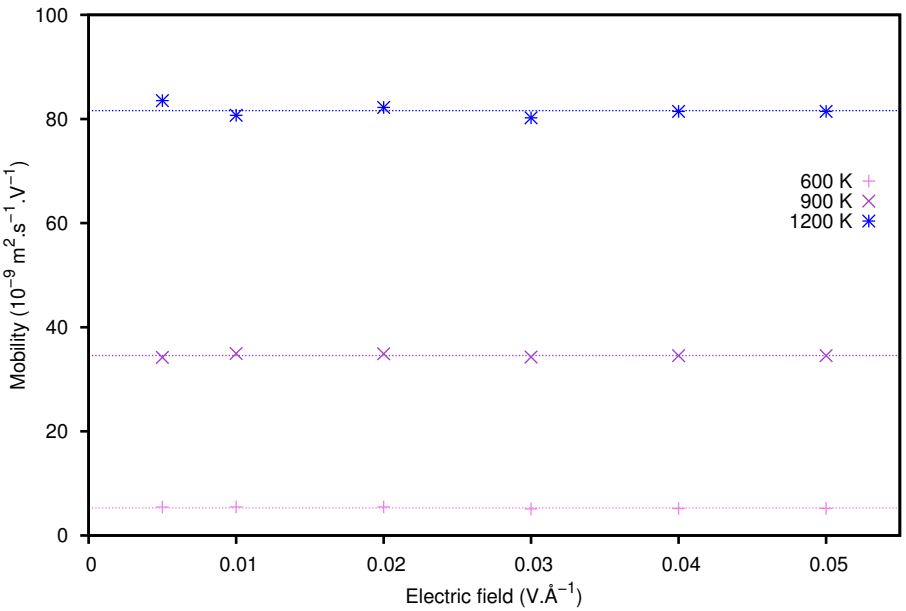

Figure 5.8: Protonic mobility as a function of local electric field (applied along x) at 600 K, 900 K and 1200 K.

From the relation $\mu = \frac{eD}{k_B T}$, we can compute the diffusion coefficient: $D = \frac{\mu k_B T}{e}$, and plot it as a function of temperature, to recover the results obtained in the previous section, in the absence of electric field. We indeed get the same values with an error lower than 10% , and around 5% at high temperature ($\geqslant 700$ K). These differences are related to the numerical uncertainties of the two approaches.

But considering our orthorhombic structure, it might be interesting to study the anisotropy of the diffusion coefficient by applying an electric field in each pseudo-cubic direction. However, the diffusion seems to be rather isotropic for the proton: figure 5.9 shows the diffusion coefficient computed when applying an electric field in each direction, for a doping rate $\delta = 12.5\%$. The protonic mobility is almost identical whatever the direction, with a slight difference for the z-axis, consistent with the fact that x and y-axis are alike in the *Pnma* structure while z-axis (corresponding to the b-axis of the orthorhombic cell) is special. We finally find an activation energy of 0.354 eV for x and y-axis, and 0.377 eV for z-axis.

Note that the protonic conductivity, obtained by $\sigma = 11.15 \times e n_H \mu$, cannot be recovered with our studies since it requires the knowledge of the concentrations of

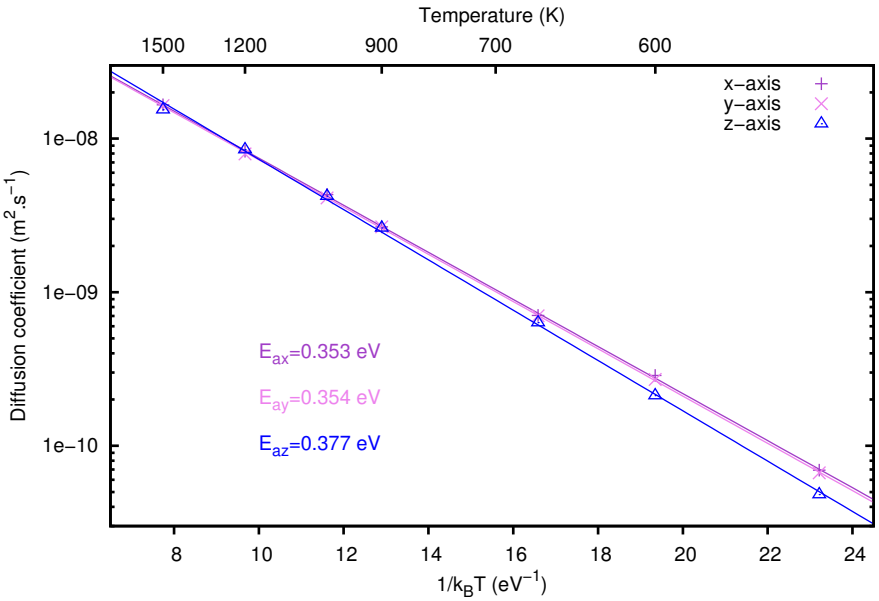

Figure 5.9: Diffusion coefficient, calculated from protonic mobility, along the a, b and c-axis as a function of temperature.

protons n_H. However, assuming a full hydration (*i.e.* n_H is equal to the dopant concentration: if $\delta = 12.5\%$, there are half a dopant per *Pnma* cell of volume 350 Å^3, $n_H = 1.166 \times 10^{22}\,\mathrm{m}^{-3}$), we get a conductivity $\sigma = 7 \times 10^{-3}\,\mathrm{S\,cm}^{-1}$ at 900 K. In Y-doped $BaCeO_3$ with a doping rate of 10%, Grimaud et al. [122] found that the protonic defect concentration can reach the doping rate (10%) at 873 K if the partial pressure of H_2O is above 0.1 bar. Under these conditions, they found a protonic conductivity around $\sigma = 0.01\,\mathrm{S\,cm}^{-1}$. Previously, Oishi et al. [146] got a similar result with $\sigma = 0.014\,\mathrm{S\,cm}^{-1}$ at the same temperature with a partial pressure of water around 0.02 bar and a very low partial pressure of oxygen ($P_{O_2} = 10^{-4}$ bar) in order to avoid a possible hole conduction. Considering the fact that, with a more realistic attempt frequency instead of $\nu_0 = 10^{13}$ Hz, we would have a mobility higher by a factor 2 or 3, our results are consistent with experiments.

5.3.2.3 Anionic

The same study can be applied to oxygen vacancies. When applying an electric field along the x-axis, we find and oxygen vacancy mobility of $3 \times 10^{-9}\,\mathrm{m\,s}^{-2}\,\mathrm{V}^{-1}$ at 600 K, $62 \times 10^{-9}\,\mathrm{m\,s}^{-2}\,\mathrm{V}^{-1}$ at 900 K and $240 \times 10^{-9}\,\mathrm{m\,s}^{-2}\,\mathrm{V}^{-1}$ at 1200 K for the dry compound with 12.5% of gadolinium. The fact that the mobility and the diffusion coefficient of oxygen vacancies are higher than the protonic ones at high temperature, may be an artefact due to the use of the same prefactor ν_0 while the attempt frequency of proton is likely to be higher than the attempt frequency of oxygen. Therefore, these values should not be compared. What can be compared with each other are:

i/ the activation energies (whatever the defects, the doping rate, the axis) since the values are not dependent of ν_0,

ii/ the diffusion coefficients (or the mobility) for the same kind of defect along different axis or for different doping rate.

Figure 5.10 shows the Arrhenius plots for an electric field applied in the three pseudo-cubic directions. Oxygen vacancy diffusion is significantly anisotropic. Indeed the activation energy along the z-axis is found around 0.61 eV while it is only of 0.51 eV along x and y-axis. This result could have been predicted when looking at the barrier energies of table 4.4: barriers between apical and equatorial oxygen (O1↔O2) are globally higher by 0.1 eV than barriers between two equatorial oxygen atoms O2.

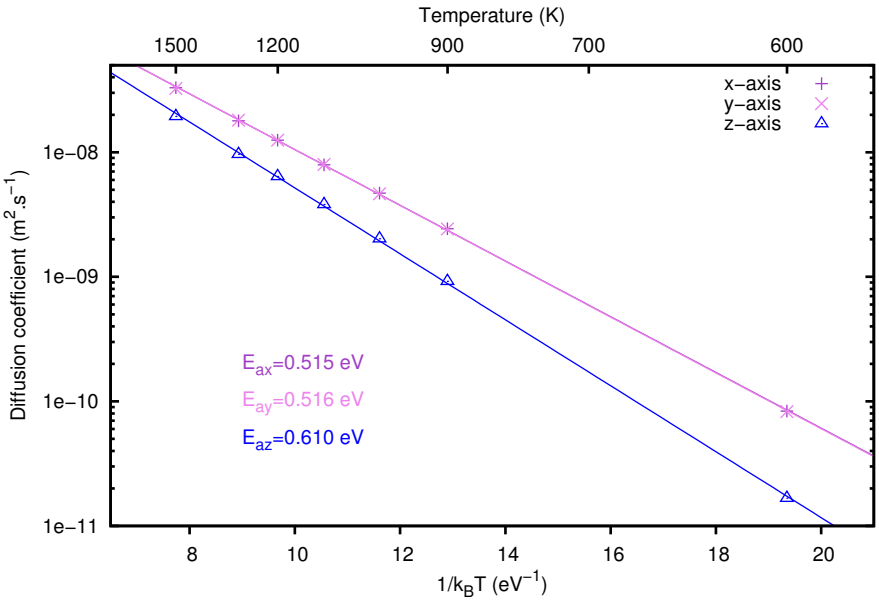

Figure 5.10: Diffusion coefficient, calculated from oxygen vacancy mobility, along the a, b and c-axis as a function of temperature.

This anisotropy obviously impacts the mobility: the values previously given were computed for an electric field along the x-axis. If we now study the conduction of oxygen vacancy along the b-axis, we find much lower values: $0.6 \times 10^{-9}\,\mathrm{m\,s^{-2}\,V^{-1}}$ at 600 K, $24 \times 10^{-9}\,\mathrm{m\,s^{-2}\,V^{-1}}$ at 900 K and $124 \times 10^{-9}\,\mathrm{m\,s^{-2}\,V^{-1}}$ at 1200 K. From these values, as we did for the protonic defect, we can compute a conductivity assuming a completely dry material: $\sigma = 11.15 \times 2en_V\mu$ (n_V is equal to half the dopant concentration). This approximation may be true for low partial pressure of O_2 and H_2O and high temperature. At 900 K, we find a conductivity of $\sigma = 5 \times 10^{-3}\,\mathrm{S\,cm^{-1}}$. With the assumptions of completely hydrated or dry materials, the only difference between protonic and anionic conductivity comes from the mobility. The mobility values for both defects are very close, but we should keep in mind that this observation is mainly due to the use of the same prefactor in both cases, while in fact, the attempt

frequencies are likely to differ by a factor 3 or more. For a zero partial pressure of water (dry compound), Grimaud et al. [122] find a conductivity at 873 K similar to the one of the protonic conductivity in the fully-hydrated case, of $\sigma = 0.01\,\mathrm{S\,cm^{-1}}$.

5.4 Discussion

In this section, we will discuss only the behaviour of protonic defects, which is very peculiar regarding previous models: the two-state model of Hempelmann [116] and some suggestions made by Kreuer [9] to correct it.

5.4.1 Discrepancy with respect to the two-state model [116]

The two-state model of Hempelmann is illustrated in figure 5.11 (for $SrCeO_3$ doped with ytterbium). The dopant are considered as trap with an escaping time τ_0 while the energy barriers « far » from dopants are associated to another time τ_1.

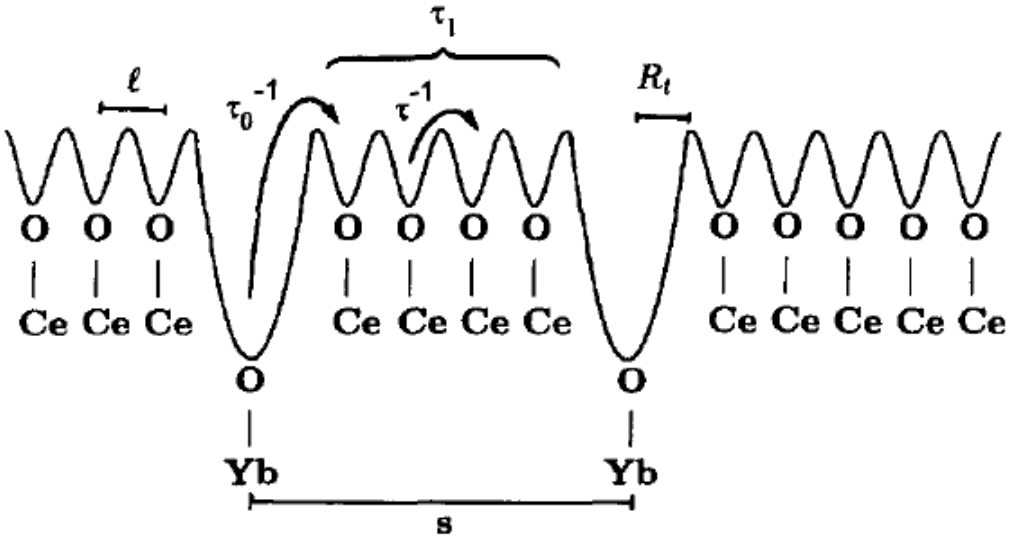

Figure 5.11: Two-state model of Hempelmann applied to Yb-doped $SrCeO_3$, figure taken from Ref. [116]

From this representation, it clearly appears that this model cannot match our simulations since the energy landscape for protons has been found to be much more complex. This model is probably good for cubic perovskites, but in an orthorhombic structure:

i/ even in the absence of dopant, the stable sites are not alike they can differ in energy up to 0.2 eV.;

ii/ near the dopant, the same difference in energy can be observed, even though there is a global decrease of the energy landscape.

In fact, the presence of dopant has a double effect on perovskites with orthorhombic structure:

- the most stable sites of the energy surface ($1a$, $1b$, $1d$, $2b$, $2d$) are even more stabilised by $\approx 0.1\,\text{eV}$ and are likely to behave as traps;
- the less stable sites, with high energy ($1c$, $2a$, $2c$), are lowered to the energy of the most stable sites of the primitive surface, but not enough to create traps. Some obstacle to protonic diffusion have been removed thanks to the introduction of a dopant.

It is thus probable the two-state model does no apply to the present case.

Indeed, according to this model, when increasing the dopant concentration, we should have a decrease of the diffusion coefficient but an activation energy kept constant. We found an activation energy rather constant (though slightly decreasing), but the diffusion coefficient is not clearly decreasing.

5.4.2 Discussion with respect to Kreuer's hypothesis [9]

The vision of Kreuer is a bit different from Hempelmann's model: he suggests that the proton-dopant interaction is not local but delocalised over the material leading to a global increase in the basicity of all oxygen atoms. This assumption explains why an increase of hydration enthalpy with the doping rate is usually observed in perovskites, even at low doping rate.

However, his hypothesis is also based on the assumption that dopants behave as traps for the proton: it is perfect to represent a cubic perovskite but should not apply to an orthorhombic system for the same reason mentioned above (creation of traps but also removal of obstacles). In his experimental result, he found an increase of the absolute value of activation energy with the doping rate. However, for the proton, we observe the contrary: the absolute value of activation energy is rather constant – and even seems to slightly decrease – when increasing the doping rate.

At low doping rate – below 12.5% – the activation energy and the diffusion coefficient seem rather constant. It appears that protonic diffusion is relatively independent on the dopant concentration from 3.125% to 12.5%. This surprising result can be explained by the two opposite effects induced by dopant: the creation of trap for the most stable protonic positions, and the removal of obstacles that constituted the highest-energy positions. The global effect of dopant on the long-range diffusion is a compensation between both phenomena and result in an invariance of the diffusion coefficient and the activation energy.

At high doping rate, we are probably missing the strong trapping effect created by pair of dopants. When $\delta \geqslant 12.5\%$, the regions near the dopant are likely to connect to each other creating diffusion path of lower energy around the dopants. This vision is consistent with the behaviour we observed: an increase of the diffusion coefficient and a decrease of the absolute value of activation energy. But we are not treating correctly the case of neighbouring dopants. Between two dopants, the proton sites could be drastically stabilised [29] with a much lower energy than near only one dopant. For instance, Björketun et al. [29] chose to represent the effect of a pair of dopant by doubling the association energy. Besides, the influence of a pair of dopants could extend beyond the 1st coordination shell.

However, the fact that the absolute value of activation energy increases with dopant concentration is not that obvious either when looking at experimental values showed in table 5.4. Indeed, if the activation energy seems to increase slightly at "low" doping rate, it seems to reach a plateau around 15%.

Furthermore, another computational study, using the same KMC technique we employed, by Bilić and Gale [132] find similar results on In-doped $CaZrO_3$, an orthorhombic perovskite. Indeed, they found a slightly higher (almost equal) protonic diffusion coefficient in the doped material compared to the pure one and concluded that dopant-proton trapping is weak and short-ranged. This result on another orthorhombic perovskite is in agreement with figure 5.4: the diffusion coefficient is constant – if not slightly increasing – when the doping rate increases.

Kinetic Monte-Carlo simulations have shown that gadolinium could be a very interesting dopant in $BaCeO_3$: thanks to its weak attraction power, and the complex energy landscape of the orthorhombic structure, gadolinium atoms act like shallow traps on the protons. BCGO keeps good diffusion and conduction properties when the doping rate increases, and confirms to be a possible electrolyte for PCFC.

Chapter 6

About quantum effects

So far, quantum effects in nuclei have been completely ignored. And yet, compounds containing hydrogen are known to have a high Debye temperature. Indeed, the O–H bond is usually associated with a frequency of 3000 cm^{-1} leading to a Debye temperature of approximately 4000 K. Below this temperature, and so at the working temperature of a fuel cell, quantum effects might be significant.

This chapter will simply give an introduction to the treatment of quantum effects with qualitative results. First, two rough approaches to get an order of magnitude of quantum effects will be presented, then some preliminary results obtained with PIMD computations will be displayed.

Contents

6.1 Zero-point effects - Tunnelling

The quantum nature of nuclei is expected to modify the « classical » energy barrier between two stable positions because zero-point effects affect differently the energy of the stable and saddle positions. If the barrier is lowered, the density of probability in the classically forbidden region increases inducing a tunnelling current. Zero-point motions and tunnelling current are thus two manifestations of the same phenomenon.

In order to get a first approximation of these effects, we will use very simple models and calculate the modified energy barrier and the tunnelling current.

6.1.1 Zero-point energy

Zero-point effects are expected to increase the energy of stable positions so that some sites of high energy such as 1c may become unstable.

The first idea to get zero-point energy associated to a protonic position is to consider the O–H bond as an harmonic oscillator (harmonic approximation). More generally, we can assume that the forces applied on the proton by other atoms of the crystal can also be modelled by a N-dimensional oscillator with N frequencies $\{\omega_i\}$. With this assumption, the ground state energy is simply given by:

$$E_0 = \sum_i \frac{\hbar\omega_i}{2}. \tag{6.1}$$

This method has been previously used on $BaZrO_3$ by [15].

If we use the results obtained by phonon computations presented in table 5.2, we can calculate the zero-point energy for some stable positions and saddle point. From these modifications, we can deduce the new energy barrier including zero-point effects.

Mechanism	Stable site	E_0	Saddle point	E_0	ΔE_0	ΔE
reorientation	1d	0.30	1d–1c	0.28	-0.02	0.06
intra hopping	1a	0.31	1a–2d	0.18	-0.13	0.50
inter hopping	2b	0.31	2b–2b	0.17	-0.13	0.16

Table 6.1: Zero-point energies for some protonic positions, computed from phonon frequencies.E_0 is the zero point energy for stable and saddle positions. ΔE is the energy barrier without zero-point effects associated to a mechanism, and ΔE_0 is the change on the energy barrier due to quantum effects. All energy values are given in eV.

Table 6.1 shows the zero-point energy for some protonic positions and an example of « quantum » barrier for each mechanism. It appears that the modification of the barrier due to zero-point motion is very significant, especially in the case of

inter-octahedral hopping. For reorientation, the modification is rather low, even if it represents one third of the barrier height in the case of 1d–1c. This value of 0.02 eV is likely to be recovered for other reorientations with much higher energy (up to 0.50 eV). This slight impact of quantum effects on reorientation is expected since the O–H bond is not broken during the process and is responsible for the highest frequencies.

On the contrary the protonic transfer should be significantly affected by zero-point corrections. Indeed, the frequencies in the stable positions are very different from the frequencies in the saddle point leading to a large modification of the barrier of 0.13 eV. This is particularly high with respect to the barrier height of inter-octahedral hopping, around 0.20 eV, while intra-octahedral hopping have energy barriers around 0.40 eV. However, as explained in the paragraph on approximations (see section 4.3.1) made on the barriers, the use of a generalised gradient approximation as exchange-correlation functional strongly underestimates the energy of a proton equally shared by two oxygens [131] by ≈ 0.10 eV to 0.15 eV. Therefore, trying to correct this error will lead an increase of the barrier by 0.10 eV to 0.15 eV. On the other hand, the quantum effects will lead to a decrease of the barrier by 0.13 eV. Both effects might thus compensate, but one should keep in mind that there is a huge uncertainty on the value of the barrier for transfer, especially in the case of inter-octahedral transfer.

These contribution of zero point effects for transfer and reorientation of -0.13 eV and -0.02 eV are very similar to the one found in $BaZrO_3$ by Sundell et al. [15], with values of -0.12 eV and -0.04 eV respectively. These large impact on transfer barriers and weak influence on reorientation have also been found by PIMD in $BaZrO_3$ by Zhang et al. [64].

6.1.2 Tunnelling effect

As a first approximation, we can model the barrier of a proton transfer with a very simple one-dimensional squared barrier shown in figure 6.1. Let us take the case of the lowest barrier and the smallest distance to cross: the inter-octahedral hopping (such as the transition $2b \rightarrow 2b$). The average barrier height is around 0.2 eV, and the distance between the initial and final position is around 0.8 Å.

We can solve analytically the Schrödinger equation $H\phi = E\phi$ for a 1D particle in this energy landscape. Using notations of figure 6.1 to distinguish the three zones along the z-axis, for a proton of mass m and energy E, we have:

$$\begin{cases} \phi_1(z) = & Ae^{ikz} + & Be^{-ikz} \\ \phi_2(z) = & Ce^{\beta z} + & De^{-\beta z} \\ \phi_3(z) = & Fe^{ik(z-a)} + & Ge^{-ik(z-a)} \end{cases} \tag{6.2}$$

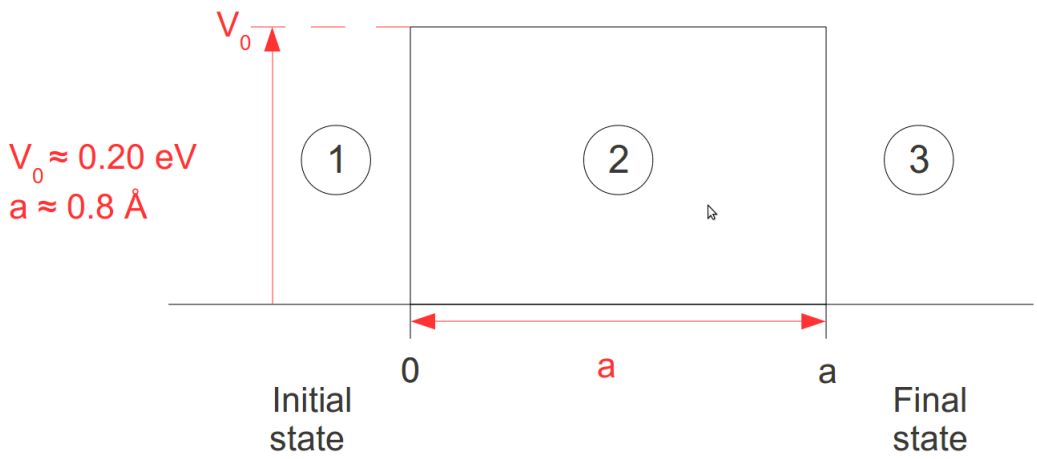

Figure 6.1: Model for a barrier of protonic inter-octahedral hopping.

where $k = \frac{\sqrt{2mE}}{\hbar}$ and $\beta = \frac{\sqrt{2m(V_0-E)}}{\hbar}$.

If we set down $\varepsilon = \frac{E}{V_0}$ and $\sigma = \frac{2mV_0a^2}{\hbar^2}$, the transmission coefficient is given by:

$$T(\varepsilon) = \left[1 + \frac{\sinh^2\sqrt{\sigma(1-\varepsilon)}}{4\varepsilon(1-\varepsilon)}\right]^{-1}. \tag{6.3}$$

As done by Sundell et al. [15] on $BaZrO_3$, we can take for the energy E the difference in zero point effects. For an inter-octahedral transfer, we have $E = 0.13\,\text{eV}$, leading to a transmission factor $T(\varepsilon) = 3 \times 10^{-4} = 0.03\%$. This value may seems rather small but it is not negligible. Furthermore, the transmission coefficient is very sensitive to the ratio $\frac{E}{V_0}$. If we take the barrier height of $2b - -2b$ inter-octahedral transfer (0.16 eV), we find a diffusion coefficient ten times higher: $T(\varepsilon) = 0.27\%$. The tunnel current is also sensitive to the width of the barrier, and hence it could be much higher in perovskites with a smaller lattice constant and/or a larger distortion (both effects leading to a smaller value of a).

6.2 PIMD approach

We performed some Path-Integral Molecular Dynamics simulations still using ABINIT code[147] on a charged *Pnma* cell of $BaCeO_3$ with one hydrogen atom. This 21-atom cell is treated in the Born-Oppenheimer approximation: at each step, the electronic structure is first optimized with DFT, then the nucleus positions in the different beads are moved. As we explained in chapter 1, the key parameter is the Trotter number P that determine the number of beads to use in order to recover the quantum partition function. Our computations were performed in the canonical ensemble NVT, using Langevin thermostat. This thermostat adds another

input parameter: the friction mass. Several values were tested in order to get the best possible convergence on temperature (*i.e.* a small relaxation time, and small fluctuations).

We chose to use 16 imaginary time slices (or « beads »), as used by Zhang et al. [64] in an analogous material $BaZrO_3$, at 600 K. The Trotter number is dependent on the temperature, the product $P \times T$ should be kept constant to get the same discretisation: *e.g.* we should use 32 time slices at 300 K. Trajectories of ≈ 5000 steps have been performed using a time step $\delta t = 20$ a.u $= 5$ fs.

Figure 6.2 shows the density probability of finding an hydrogen and its bonding oxygen in a plane (xOy) (it is the plane in which the reorientation process occurs). It is hard to distinguish the quantum fluctuations from thermal fluctuations: the density includes the positions of the 16 images (or beads) during 4000 steps of PIMD. The proton is obviously much more delocalised than the oxygen, but it could be simply due to the thermal fluctuations. Considering the two peaks of protonic density, we can deduce that during this 4000 steps a reorientation process has probably happened.

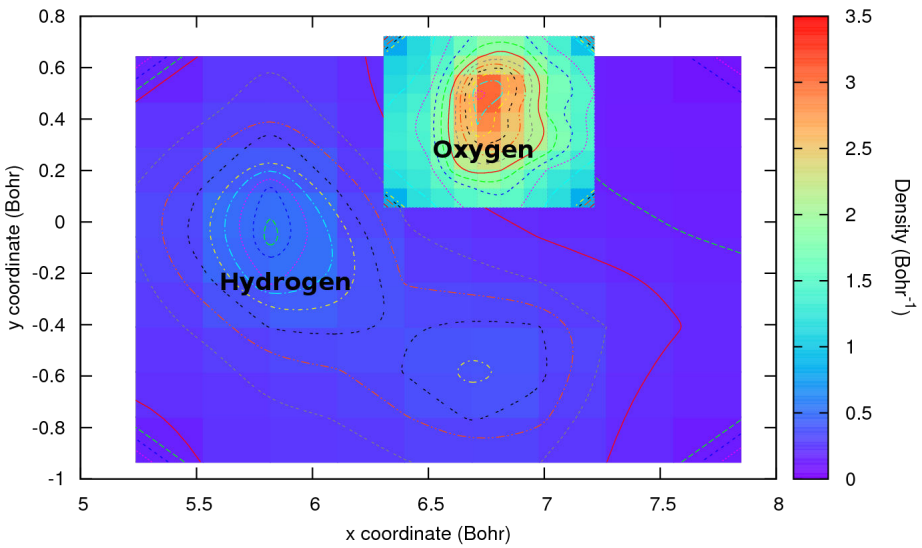

Figure 6.2: Density of presence (per Bohr) of one oxygen and one proton in a plane (xOy).

In order to really get an idea of quantum fluctuations, we can compute the spatial extension of the wave packet for each kind of atoms. It is related to the distance between images of a same particle though the relation:

$$d = \sqrt{\frac{1}{P}\sum_{i=1}^{P} |\vec{r_c} - \vec{r_i}|^2}, \tag{6.4}$$

where $\vec{r_c}$ is the position of the centroid (centre of mass of all beads associated to one atom), and $\vec{r_i}$ the position of a specific bead.

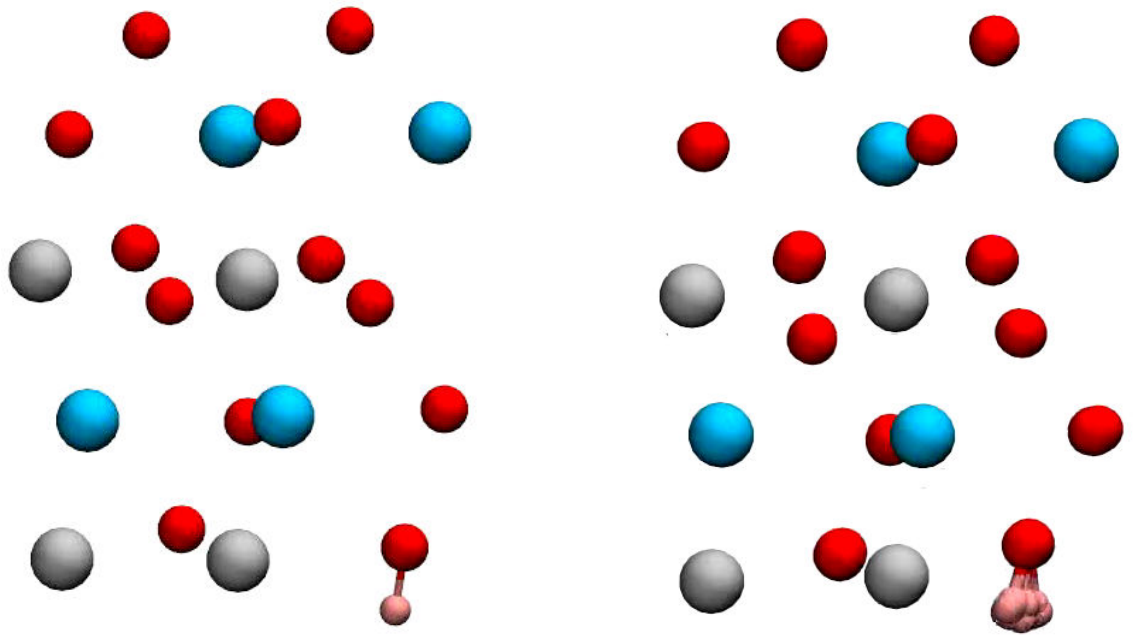

(a) P=1 (b) P=16

Figure 6.3: Frames of PIMD simulations using a *Pnma* cell of 20 atoms with one bead (classical) and 16 beads.

Figure 6.3 compares two frames of PIMD simulations: one using only one imaginary time slice, equivalent to a classical molecular dynamics simulation, and the other using sixteen imaginary time slices. The uncertainty on hydrogen positions appears clearly, and can also be slightly observed on oxygen. Heavy atoms, barium and cerium, have their sixteen images at the same point suggesting that quantum effects are not significant for them.

Using equation 6.4, we compute the spatial extension of the wave packet for each atom averaged over 4000 PIMD steps, and find the following values:

$$d_{barium} = 0.017\,\text{Å},\ d_{cerium} = 0.016\,\text{Å},\ d_{oxygen} = 0.048\,\text{Å} \text{ and } d_{hydrogen} = 0.157\,\text{Å}$$

The extension of hydrogen is ten times higher than the one of heavy atoms but it is still rather small compared to the distance between two stable sites ($\approx 0.8\,$Å). Hence, the covering of two wave packets in different protonic sites is expected to be very small.

Unfortunately, considering the huge computational cost necessary to get quantitative effects, we did not go further so far. It indeed requires to perform several path integral molecular dynamics simulations under constraints for different configurations along the minimum energy path. This method have been previously used once on $BaZrO_3$ by Zhang et al. [64]. They have found that adding quantum effects of nuclei turn the reorientation process into the rate-limiting step below 600 K. This is

consistent with what was predicted by our rough approaches: the reorientation being less affected by quantum effects than the transfer, its barrier is almost kept identical while the transfer barriers may be significantly lowered.

Qualitative results of quantum effects of nuclei has been presented in hydrated $BaCeO_3$. It appears that adding zero-point energy does not affect a lot the reorientation process, but considerably lowers the barrier for transfers (up to 65%). However, this huge change may be partly compensated by the underestimation of the barrier made in GGA. Quantum effects could still suppress some stable positions of high energy such as 1c *and hence, they can have a significant impact on the energy landscape. PIMD simulations confirm the quantum character of the dynamics of H^+ (with respect to other atoms). Further computations are needed to determine precisely quantitative changes induced by zero-point effects.*

Conclusion

In this thesis, we have presented a study of protonic and anionic diffusion in an orthorhombic perovskite: Gd-doped $BaCeO_3$. This material is of particular interest as an electrolyte for Protonic Ceramic Fuel Cell. It should thus verify some conditions: to have an insulating character, to be hydrated at the working temperature of fuel cell and to have a good protonic conduction. The main interest of this study was to analyse the influence of the gadolinium dopant on proton diffusion since dopant are usually considered as trap. They are necessary to increase the number of water molecules that the material can incorporate but they often deteriorate the diffusion. One purpose of the study was to examine how that gadolinium affects the properties of the various defects.

The first step of the study was to determine the stable positions of defects in the doped material, for oxygen vacancy and hydrogen (protonic defect). It appears that in such orthorhombic structure, the energy landscape is very complex, with eight different positions without considering the dopant interaction. We finally simplify this energy surface in the doped material to a 16 minima landscape. For the oxygen vacancy, we only kept four different positions. From these DFT computations, we also checked that Gd-doped $BaCeO_3$ was an insulator whether it is hydrated or dry. Furthermore, the thermodynamics conditions of stability of the hydrated state were carefully studied to answer the second necessary condition to be an electrolyte for fuel cell.

In a second time, all the barriers between two stable positions were computed using the algorithm of String Method. This was the main time-consuming step, since it requires the optimisation of 10 or 19 images for more than forty different paths. Contrary to cubic perovskites, the reorientation does not appear as a very fast process in orthorhombic perovskites, but with a very wide range of values from 0.02 eV up to 0.54 eV. The barrier height of transfers are less scattered: intra-octahedral transfer are found around 0.4 eV while inter-octahedral transfer have lower barriers around 0.2 eV. It is really hard to determine which mechanism is the rate-limiting step since

one mechanism (reorientation, inter- or intra-octahedral transfer) can be associated to very different barriers.

After these long computations, the energy barriers were used as an input for Kinetic Monte-Carlo simulations. The results of these simulations allow to calculate the activation energy through an Arrhenius fit of diffusion coefficient versus temperature. An activation energy around 0.37 eV was found for the proton. Both diffusion coefficient and activation energy seem rather independent of the doping rate. For the oxygen vacancy, on the contrary, the absolute value of activation energy (≈ 0.5 eV) increases and the diffusion coefficient decreases with the doping rate. This suggests that gadolinium dopant really behave as traps with respect to the oxygen vacancies, while their influence on protonic diffusion is more complex and non trivial. The weak attraction exerted by the dopant on the proton constitutes a good characteristic of gadolinium, considering its possible application as a dopant in an electrolyte for fuel cell.

Simulations under electric field were also performed to determine the defects mobility. Besides the mobility, these computations provide a simple way to study the anisotropy of diffusion in Gd-doped $BaCeO_3$. While protonic diffusion seems rather isotropic, it appears that oxygen vacancies move more easily in the (ac) plane than along the b-axis.

Finally, in a very qualitative manner, quantum effects of nuclei have been approached by several methods: calculations of zero-point energies from phonon computations, and path-integral molecular dynamics simulations. The quantum effects might change the landscape with the eventual suppression of one stable position but should not drastically affect the barriers and hence the mechanisms of protonic diffusion.

This work could be extended in several directions. For instance, it would be interesting to get quantitative results of quantum effects of nuclei performing path-integral molecular dynamics under constraints, though it may not be worth the computational amount of time required.

Concerning the Monte-Carlo simulations, they could be extended following two different trails:

- a grand-canonical Monte-Carlo algorithm, simulating the material BCGO in contact with water, should provide the protonic concentration at thermodynamic equilibrium as a function of the temperature and water partial pressure. This concentration, associated with the diffusion coefficient, allows to determine

the conductivity of a material. It strongly depends on the temperature, and can drop suddenly at high temperature. It is thus fundamental to determine this concentration to be sure to have a good conductivity at the operating temperature of a fuel cell.

- Kinetic Monte-Carlo simulations under an alternative electric field provide informations on capacitive effects. It could be important if the distribution of dopant is not homogeneous in the material creating space-charged zone. Nyquist plots can be drawn from such simulations in order to determine the capacitance associated to these zones.

Another very interesting perspective is the study of grain boundaries effects. Indeed, we have only studied a single crystal but practically, the electrolyte is made of numerous grains. The conductivity in grain boundaries is known to be a limiting factor in $BaZrO_3$, and hence cannot be neglected. Moreover, the grain boundaries might create space charged zones with an accumulation of defects. Many recent numerical studies are now focussing on the grain boundaries effects.

Appendix A

Expression of exchange-correlation functional

A.1 LDA Functional

A.1.1 VWN correlation

To get the common local density approximation exchange-correlation functional, we must had to the Slater exchange described in equation 1.20 the local correlation of Vosko, Wilk and Nusair. The VWN correlation energy per electron is written as:

$$\varepsilon_c(r_s) = \frac{A}{2}\left(\ln\frac{x^2}{X(x)} + \frac{2b}{Q}\arctan\frac{Q}{2x+b} - \frac{bx_0}{X(x_0)}\left[\ln\frac{(x-x_0)^2}{X(x)} + \frac{2(b+2x_0)}{Q}\arctan\frac{Q}{2x+b}\right]\right)$$

with

$$x = r_s^{1/2}, \qquad X(x) = x^2 + bx + c, \qquad Q = (4c - b^2)^{1/2}$$

and the parameters $A = 0.0621814$, $b = 3.72744$, $c = 12.9352$ et $x_0 = -0.10498$.

A.2 GGA functional (PBE)

A.2.1 PBE exchange

The exchange energy of a GGA functional can be written as:

$$E_x^{GGA} = \int n\varepsilon_x^{hom}[n]F_x[s]d^3r$$

where F_x is the enhancement factor and $s = \frac{|\nabla n|}{2k_F n}$ the reduced gradient (with $k_F = (3\pi^2 n)^{1/3}$).

But we can also present the GGA exchange functional as a correction to the LDA:

$$E_x^{GGA} = E_x^{LDA} + \Delta E_x^{GGA} = \int \left(\varepsilon_x^{LDA} + \varepsilon_x^{GGA}\right) n(\vec{r})d^3r.$$

For PBE exchange, then enhancement factor is rather simple:

$$F_x[s] = 1 + \kappa - \frac{\kappa}{1 + \frac{\mu s^2}{\kappa}}$$

where both parameters $\kappa = 0.804$ and $\mu = \beta(\pi^2/3) \simeq 0.21951$ have been determined in order to respect some physical constraints – the choice of κ allows to satisfy the Lieb-Oxford bound, and the choice of μ allows to recover the linear response of LSDA when $s \to 0$.

A.2.2 PBE correlation

The PBE correlation energy is written as:

$$E_c^{PBE} = \int d^3r \, n(\varepsilon_c^{hom}(r_s, \zeta) + H(r_s, \zeta, t))$$

où $t = s/phi$, $\phi(\zeta) = [(1+\zeta)^{2/3} + (1-\zeta)^{2/3}]/2$ is the spin polarisation factor, et $k_s = \sqrt{4k_F/\pi a_0}$ is the wave vector of Thomas-Fermi. ε_c^{hom} represents the correlation ernergy per electron of the homogeneous electron gas, and H is the gradient contribution:

$$H = \gamma\phi^3 \ln\left(1 + \frac{\beta}{\gamma}t^2\left[\frac{1 + At^2}{1 + At^2 + A^2t^4}\right]\right)$$

où $A = \frac{\beta}{\gamma}\left[\exp\left(-\frac{\varepsilon_c^{hom}}{\gamma\phi^3}\right) - 1\right]^{-1}$, $\beta = 0.066725$ et $\gamma = 0.031091$.

Appendix B

Thermodynamics stability of Gd-doped $BaCeO_3$

In this appendix, we want to examine the stability of dry BCGO compound with respect to pure elements in their metallic state and their oxides, in order to find the thermodynamics conditions in which BCGO is stable. We use the same method of grand potential computation as in section 3.4: $\Omega = E^f - \sum_j N_j \Delta\mu_j$.

The grand potential of pure barium cerate is given by:

$$\Omega = E^f_{BaCeO_3} - \Delta\mu_{Ba} - \Delta\mu_{Ce} - 3\Delta\mu_O,$$

with $E^f_{BaCeO_3}$ the formation energy of BCO:

$$E^f_{BaCeO_3} = E_{BaCeO_3(bulk)} - E_{Ba(s)} - E_{Ce(s)} - \frac{3}{2}E_{O_2(g)}.$$

To determine where BCGO can be stable, we have to find a zone in the space ($\Delta\mu_O$,$\Delta\mu_{Ce}$,$\Delta\mu_{Ba}$,$\Delta\mu_{Gd}$) where the grand potential of $BaCe_{1-\delta}Gd_\delta O_{3-\delta/2}$ is lower than that of the elementary metals, gases and their related oxides. This space cannot be easily represented though, so we will try to reduce the space to two dimensions.

We can first eliminate one of the variables, for instance $\Delta\mu_{Ba}$, using the relation of formation energy:

$$E^f_{BCGO} = \Delta\mu_{Ba} + (1-\delta)\Delta\mu_{Ce} + \delta\Delta\mu_{Gd} + \left(3 - \frac{\delta}{2}\right)\Delta\mu_O. \tag{B.1}$$

The prevention of formation of metals, gases and binary oxides leads to several conditions: chemical potentials of Ba, Ce, Gd and O must be smaller in $BaCe_{1-\delta}Gd_\delta O_{3-\delta/2}$ than in other phases: $\mu_j < E_j$ for each species j:

$$\Delta\mu_O < 0, \Delta\mu_{Ce} < 0, \Delta\mu_{Gd} < 0, \Delta\mu_{Ba} < 0, \tag{B.2}$$

$$\Delta\mu_{Ba} + \Delta\mu_O < E^f_{BaO}, \tag{B.3}$$

$$\Delta\mu_{Ce} + 2\Delta\mu_O < E^f_{CeO_2}, \tag{B.4}$$

$$2\Delta\mu_{Gd} + 3\Delta\mu_O < E^f_{Gd_2O_3}, \tag{B.5}$$

Combining equations (B.1)–(B.5), we finally get four conditions between $\Delta\mu_{Gd}$, $\Delta\mu_{Ce}$ and $\Delta\mu_O$:

- No precipitation of Ba:

$$\delta\Delta\mu_{Gd} \geqslant E^f_{BCGO} - (1-\delta)\Delta\mu_{Ce} - \left(3 - \frac{\delta}{2}\right)\Delta\mu_O \tag{B.6}$$

- No precipitation of BaO:

$$\delta\Delta\mu_{Gd} \geqslant E^f_{BCGO} - E^f_{BaO} - (1-\delta)\Delta\mu_{Ce} - \left(2 - \frac{\delta}{2}\right)\Delta\mu_O \tag{B.7}$$

- No precipitation of CeO_2:

$$\Delta\mu_{Ce} \leqslant E^f_{CeO_2} - 2\Delta\mu_O \tag{B.8}$$

- No precipitation of Gd_2O_3:

$$\Delta\mu_{Gd} \leqslant \frac{E^f_{Gd_2O_3}}{2} - \frac{3}{2}\Delta\mu_O \tag{B.9}$$

	Formation enthalpy (eV/f.u.)	
	GGA [our work]	Exp.
H_2O	-2.50	
BaO	-5.06	-5.78 [148]
CeO_2	-10.42	-11.30 [149]
Ce_2O_3		-18.58 [83]
Gd_2O_3	-17.39	-18.94 [83]
$BaCeO_3$	-15.97	-17.52 [103]
dry	-15.64	-17.18 [150]
oxidized	-15.69	
hydrated	-15.88	

Table B.1: Formation enthalpies of binary oxides, of BCO and BCGO ($\delta = 0.125$).

To avoid an unclear 3D diagram, we plot the precipitation lines of all binary oxides and pure elements in the plane $\Delta\mu_{Gd} = -5\ eV$ in figure B.1 using the enthalpy values of table B.1 from our work and from experiments (the doping rate δ is equal to 12.5%), and using the equations B.6–B.9. The stability zone of BCGO is represented by hatched area. The choice of another $\Delta\mu_{Gd} = c$ plane lead to a diagram with the same shape but shifted to lower values of $\Delta\mu_O$, and higher values of $\Delta\mu_{Ce}$ as we increase $\Delta\mu_{Gd}$ (when looking at the inequality B.9, it is obvious that an increase in $\Delta\mu_{Gd}$ requires a decrease in $\Delta\mu_O$).

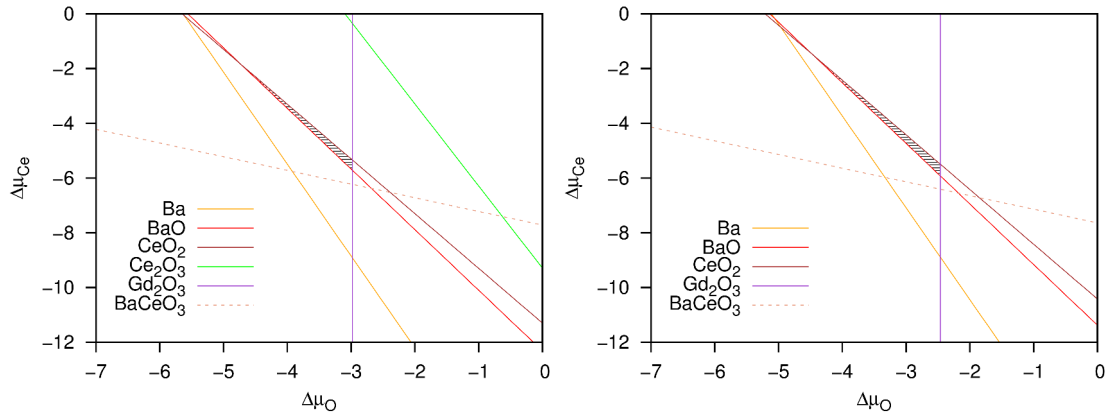

(a) Experiments (b) Simulations

Figure B.1: Thermodynamics stability diagram as a function of O and Ce chemical potentials, in the plane $\Delta\mu_{Gd} = -5\ eV$. Hatched area corresponds to the stable zone of BCGO (without considering the precipitation of $BaCeO_3$).

If we now add the condition of the non-formation of $BaCeO_3$:

$$\Delta\mu_{Ba} + \Delta\mu_{Ce} + 3\Delta\mu_O < E^f_{BCO}, \tag{B.10}$$

that we can rewrite using condition B.1 as:

$$\delta\Delta\mu_{Gd} \geqslant E^f_{BCGO} - E^f_{BCO} + \delta\Delta\mu_{Ce} + \frac{\delta}{2}\Delta\mu_O, \tag{B.11}$$

we find a contradiction between this inequality combined with equations B.7 and B.9. Indeed combining the two inequalities B.7 and B.9 on one side, and inequalities B.9 and B.11 on the other side by eliminating $\Delta\mu_{Gd}$, we get the two following relations between $\Delta\mu_{Ce}$ and $\Delta\mu_O$:

$$(1-\delta)\Delta\mu_{Ce} \geqslant E^f_{BCGO} - E^f_{BaO} - \frac{\delta}{2}E^f_{Gd_2O_3} - 2(1-\delta)\Delta\mu_O, \tag{B.12}$$

$$\delta\Delta\mu_{Ce} \leqslant -E^f_{BCGO} + E^f_{BCO} + \frac{\delta}{2}E^f_{Gd_2O_3} - 2\delta\Delta\mu_O. \tag{B.13}$$

Finally, if we calculate: $\frac{-1}{1-\delta}\times$inequality B.12$+\frac{1}{\delta}\times$inequality B.13, we eliminate $\Delta\mu_{Ce}$ and $\Delta\mu_O$, and finally get a condition on δ:

$$\delta\left(E^f_{BaO} + \frac{E^f_{Gd_2O_3}}{2}) - E^f_{BaCeO_3}\right) \geqslant E^f_{BCGO} - E_{BCO}. \tag{B.14}$$

Using the values of table B.1, we found a condition on δ: $\delta \geqslant 0.149$. However, δ is equal to 12.5% for the given value of E^f_{BCGO} leading to the contradiction. We also tested the formation enthalpy value of BCGO for $\delta = 25\%$, and find the new condition $\delta \geqslant 0.30$. Therefore, BCGO is not stable whatever the values of chemical potentials, using both experimental and simulations values for the formation energies.

This apparent contradiction with the effective existence of BCGO in experiments may be explained by kinetics: BCGO with Gd and Ce disordered on the B-sublattice is probably stable in the high-temperature conditions in which the compound is synthesised, due to the high configurational entropy associated to the disorder on the B-site. This stability could be lost at low temperature (order-disorder transition as in binary mixtures) and the system should separate into a $BaCeO_3$ phase and a Gd_2O_3 phase. Nevertheless the B-sublattice configuration (Gd and Ce) is probably frozen and kinetically blocked since the diffusion of Ce/Gd atoms involves very high activation energy that cannot be crossed at low temperature.

Bibliography

[1] W. R. Grove. On a new voltaic combination. *Philosophical Magazine and Journal of Science*, 13:430, 1838. URL http://www.tandfonline.com/doi/abs/10.1080/14786443808649618?journalCode=tphm14#.UiCY5tfmjw0.

[2] A. Becquerel. Note sur une pile voltaïque d'une grande énergie, construite par M. Grove. Compte-rendu 8, *Académie des sciences*, 1839. URL http://gallica.bnf.fr/ark:/12148/bpt6k2967c/f573.image.

[3] Space application of hydrogen and fuel cells. URL www.nasa.gov/topics/technology/hydrogen/hydrogen_2009.html.

[4] C. Darras. *Modélisation des systèmes hybrides photovoltaïque/hydrogène : Application site isolé, micro-réseau, et connexion au réseau électrique dans le cadre du projet PEPITE (ANR PAN-H)*. PhD thesis, Université de Corse-Pascal Paoli, 2011.

[5] Projet myrte : l'énergie solaire à la demande. *Le Point*. URL www.lepoint.fr/societe/projet-myrte-l-energie-solaire-a-la-demande-13-01-2012-1418700_23.php.

[6] Piles à combustible : c'est pour aujourd'hui ou pour demain? URL www.technique-ingenieur.fr/actualite/environnement-securite-energie-thematique_191/piles-a-combustible-c-est-pour-aujourd-hui-ou-pour-demain-article_81834/.

[7] L'hydrogène naturel: une contribution au mix énergétique ? IFPEN étudie le potentiel des sources d'hydrogène naturel à terre. *Communiqués de Presse*, 11 Avril 2013. URL www.ifpenergiesnouvelles.fr/actualites/communiques-de-presse/l-hydrogene-naturel-une-contribution-au-mix-energetique-ifpen-etudie-le-potentiel-des-sourdes-d-hydrogene-naturel-a-terre.

[8] H. Iwahara, T. Esaka, H. Uchida, and N. Maeda. Proton conduction in sintered oxides and its application to steam electrolysis for hydrogen production. *Solid State Ionics*, 3–4:359–363, 1981. URL http://www.sciencedirect.com/science/article/pii/0167273881901132.

[9] K. D. Kreuer. Aspects of the formation and mobility of protonic charge carriers and the stability of perovskite-type oxides. *Solid State Ionics*, 125(1-4):285–302, 1999. URL http://www.sciencedirect.com/science/article/B6TY4-3XH3HBH-18/2/cdaecbb176b79baf75a57dfc8fe6281a.

[10] K.D. Kreuer. Proton-conducting oxides. *Annual Review of Materials Research*, 33(1):333–359, 2003. URL http://www.annualreviews.org/doi/abs/10.1146/annurev.matsci.33.022802.091825?journalCode=matsci.

[11] K. D. Kreuer. Mechanisms of proton conduction in perovskite-type oxides. In Tatsumi Ishihara, editor, *Perovskite Oxide for Solid Oxide Fuel Cells*, Fuel Cells and Hydrogen Energy, pages 261–272. Springer US, 2009. URL http://dx.doi.org/10.1007/978-0-387-77708-5_13.

[12] T. Norby and Y. Larring. Concentration and transport of protons in oxides. *Current Opinion in Solid State and Materials Science*, 2(5):593–599, 1997. URL http://www.sciencedirect.com/science/article/pii/S1359028697800514.

[13] T. Norby. Solid-state protonic conductors: principles, properties, progress and prospects. *Solid State Ionics*, 125(1-4):1–11, 1999. URL http://www.sciencedirect.com/science/article/B6TY4-3XH3HBH-2/2/9d5fdeae6606b1e1fdb4ac68336a7e95.

[14] T. Norby. Proton conductivity in perovskite oxides. In Tatsumi Ishihara, editor, *Perovskite Oxide for Solid Oxide Fuel Cells*, Fuel Cells and Hydrogen Energy, pages 217–241. Springer US, 2009. URL http://dx.doi.org/10.1007/978-0-387-77708-5_11.

[15] P. G. Sundell, M. E. Björketun, and G. Wahnström. Density-functional calculations of prefactors and activation energies for H diffusion in $BaZrO_3$. *Physical Review B*, 76(9):094301, 2007. URL http://prb.aps.org/abstract/PRB/v76/i9/e094301.

[16] É. Bévillon and G. Geneste. Hydration properties of $BaSn_{0.875}M_{0.125}O_{3-\delta}$ substituted by large dopants (M=In, Y, Gd, and Sm) from first principles. *Physical Review B*, 77:184113, 2008. URL http://prb.aps.org/abstract/PRB/v77/i18/e184113.

[17] A. Bilić and J. D. Gale. Proton mobility in the In-Doped $CaZrO_3$ perovskite oxide. *Chemistry of Materials*, 19(11):2842–2851, 2007. URL http://pubs.acs.org/doi/abs/10.1021/cm070291b.

[18] P. Goudochnikov and A. J. Bell. Correlations between transition temperature, tolerance factor and cohesive energy in 2+:4+ perovskites. *J. Phys.: Condens. Matter*, 19:176201, 2007. URL http://iopscience.iop.org/0953-8984/19/17/176201.

[19] W. Münch, K. D. Kreuer, St. Adams, G. Seifert, and J. Maier. The relation between crystal structure and the formation and mobility of protonic charge carriers in perovskite-type oxides: A case study of Y-doped $BaCeO_3$ and $SrCeO_3$. *Phase Transitions*, 68(3):567–586, 1999. URL http://www.tandfonline.com/doi/abs/10.1080/01411599908224535#.UiCdE9fmjw0.

[20] R.A. Davies, M.S. Islam, and J.D. Gale. Dopant and proton incorporation in perovskite-type zirconates. *Solid State Ionics*, 126(3–4):323–335, 1999. URL http://www.sciencedirect.com/science/article/pii/S0167273899002441.

[21] M. S. Islam, R. A. Davies, and J. D. Gale. Proton migration and defect interactions in the $CaZrO_3$ orthorhombic perovskite: A quantum mechanical study. *Chemistry of Materials*, 13(6):2049–2055, 2001. URL http://pubs.acs.org/doi/abs/10.1021/cm010005a.

[22] C. Shi, M. Yoshino, and M. Morinaga. First-principles study of protonic conduction in In-doped $AZrO_3$ (A=Ca, Sr, Ba). *Solid State Ionics*, 176(11–12):1091–1096, 2005. URL http://www.sciencedirect.com/science/article/pii/S0167273805000020.

[23] M. A. Gomez, M. A. Griffin, S. Jindal, K. D. Rule, and V. R. Cooper. The effect of octahedral tilting on proton binding sites and transition states in pseudo-cubic perovskite oxides. *The Journal of Chemical Physics*, 123(9):094703, 2005. URL http://jcp.aip.org/resource/1/jcpsa6/v123/i9/p094703_s1.

[24] J. Hermet, F. Bottin, G. Dezanneau, and G. Geneste. Thermodynamics of hydration and oxidation in the proton conductor Gd-doped barium cerate from density functional theory calculations. *Physical Review B*, 85:205137, 2012. URL http://prb.aps.org/showrefs/PRB/v85/i20/e205137.

[25] J. Hermet, M. Torrent, F. Bottin, G. Dezanneau, and G. Geneste. Hydrogen diffusion in the protonic conductor $BaCe_{1-x}Gd_xO_{3-\frac{x}{2}}$ from density functional

theory. *Physical Review B*, 87:104303, 2013. URL http://prb.aps.org/showrefs/PRB/v87/i10/e104303.

[26] M. A. Gomez, S. Jindal, K. M. Fletcher, L. S. Foster, N. Dufie A. Addo, D. Valentin, C. Ghenoiu, and A. Hamilton. Comparison of proton conduction in $KTaO_3$ and $SrZrO_3$. *The Journal of Chemical Physics*, 126(19):194701, 2007. URL http://link.aip.org/link/?JCP/126/194701/1.

[27] W Münch, K.-D Kreuer, G Seifertli, and J Majer. A quantum molecular dynamics study of proton diffusion in $SrTiO_3$ and $CaTiO_3$. *Solid State Ionics*, 125 (1–4):39–45, 1999. URL http://www.sciencedirect.com/science/article/pii/S0167273899001563.

[28] W. Münch, K.D. Kreuer, G. Seifert, and J. Maier. Proton diffusion in perovskites: comparison between $BaCeO_3$, $BaZrO_3$, $SrTiO_3$, and $CaTiO_3$ using quantum molecular dynamics. *Solid State Ionics*, 136-137(0):183–189, 2000. URL http://www.sciencedirect.com/science/article/pii/S0167273800003040.

[29] M. E. Björketun, P. G. Sundell, G. Wahnström, and D. Engberg. A kinetic Monte Carlo study of proton diffusion in disordered perovskite structured lattices based on first-principles calculations. *Solid State Ionics*, 176(39–40):3035–3040, 2005. URL http://www.sciencedirect.com/science/article/pii/S0167273805005023. Selected Papers from the 12th International Conference on Solid State Proton Conductors (SSPC-12).

[30] É. Bévillon, A. Chesnaud, Y. Wang, G. Dezanneau, and G. Geneste. Theoretical and experimental study of the structural, dynamical and dielectric properties of perovskite $BaSnO_3$. *Journal of Physics: Condensed Matter*, 20(14):145217, 2008. URL http://iopscience.iop.org/0953-8984/20/14/145217/.

[31] T.E. Karakasidis and C.A. Charitidis. Multiscale modeling in nanomaterials science. *Materials Science and Engineering: C*, 27:1082 – 1089, 2007. URL http://www.sciencedirect.com/science/article/pii/S0928493106002074. EMRS 2006 Symposium A: Current Trends in Nanoscience - from Materials to Applications.

[32] K. N. Grew and W. K.S. Chiu. A review of modeling and simulation techniques across the length scales for the solid oxide fuel cell. *Journal of Power Sources*, 199 (0):1 – 13, 2012. URL http://www.sciencedirect.com/science/article/pii/S0378775311019598.

[33] J. C. Slater. A simplification of the Hartree-Fock method. *Physical Review*, 81: 385, 1951. URL http://link.aps.org/doi/10.1103/PhysRev.81.385.

[34] W. Kohn and L. J. Sham. Self-Consistent equations including exchange and correlation effects. *Physical Review*, 140:A1133, 1965. URL http://link.aps.org/doi/10.1103/PhysRev.140.A1133.

[35] P. Hohenberg and W. Kohn. Inhomogeneous electron gas. *Physical Review*, 136: B864, 1964. URL http://link.aps.org/doi/10.1103/PhysRev.136.B864.

[36] S.H. Vosko, L. Wilk, and M. Nusair. Accurate spin-dependent electron liquid correlation energies for local spin density calculations: a critical analysis. *Canadian Journal of Physics*, 58:1200–1211, 1980. URL http://rparticle.web-p.cisti.nrc.ca/rparticle/AbstractTemplateServlet?calyLang=eng&journal=cjp&volume=58&year=1980&issue=8&msno=p80-159.

[37] A. D. Becke. Density-functional exchange-energy approximation with correct asymptotic behavior. *Physical Review A*, 38:3098, 1988. URL http://pra.aps.org/abstract/PRA/v38/i6/p3098_1.

[38] C. Lee, W. Yang, and R. G. Parr. Development of the Colle-Salvetti correlation-energy formula into a functional of the electron density. *Physical Review B*, 37: 785, 1988. URL http://link.aps.org/doi/10.1103/PhysRevB.37.785.

[39] J. P. Perdew, K. Burke, and M. Ernzerhof. Generalized Gradient Approximation made simple. *Physical Review Letters*, 77:3865–3868, 1996. URL http://link.aps.org/doi/10.1103/PhysRevLett.77.3865.

[40] X. Gonze, B. Amadon, P.-M. Anglade, J.-M. Beuken, F. Bottin, P. Boulanger, F. Bruneval, D. Caliste, R. Caracas, M. Côté, T. Deutsch, L. Genovese, Ph. Ghosez, M. Giantomassi, S. Goedecker, D.R. Hamann, P. Hermet, F. Jollet, G. Jomard, S. Leroux, M. Mancini, S. Mazevet, M.J.T. Oliveira, G. Onida, Y. Pouillon, T. Rangel, G.-M. Rignanese, D. Sangalli, R. Shaltaf, M. Torrent, M.J. Verstraete, G. Zerah, and J.W. Zwanziger. ABINIT: First-principles approach to material and nanosystem properties. *Computer Physics Communications*, 180(12):2582–2615, 2009. URL http://www.sciencedirect.com/science/article/B6TJ5-4WTRSCM-3/2/20edf8da70cd808f10fe352c45d0c0be.

[41] Neil W. Ashcroft and N. David Mermin. *Physique des solides*. 2002.

[42] D. R. Hamann, M. Schlüter, and C. Chiang. Norm-conserving pseudopotentials. *Physical Review Letters*, 43:1494–1497, 1979. URL http://link.aps.org/doi/10.1103/PhysRevLett.43.1494.

[43] G P Kerker. Non-singular atomic pseudopotentials for solid state applications. *Journal of Physics C: Solid State Physics*, 13(9):L189, 1980. URL http://stacks.iop.org/0022-3719/13/i=9/a=004.

[44] D. Vanderbilt. Soft self-consistent pseudopotentials in a generalized eigenvalue formalism. *Physical Review B*, 41:7892–7895, 1990. URL http://link.aps.org/doi/10.1103/PhysRevB.41.7892.

[45] P. E. Blöchl. Projector augmented-wave method. *Physical Review B*, 50 (24):17953–17979, 1994. URL http://prb.aps.org/abstract/PRB/v50/i24/p17953_1.

[46] W. E, W. Ren, and E. Vanden-Eijnden. String method for the study of rare events. *Physical Review B*, 66:052301, 2002. URL http://link.aps.org/doi/10.1103/PhysRevB.66.052301.

[47] Weinan E, Weiqing Ren, and Eric Vanden-Eijnden. Simplified and improved string method for computing the minimum energy paths in barrier-crossing events. *The Journal of Chemical Physics*, 126(16):164103, 2007. URL http://link.aip.org/link/?JCP/126/164103/1.

[48] K. Reuter. *First-Principles Kinetic Monte Carlo Simulations for Heterogeneous Catalysis: Concepts, Status, and Frontiers*, chapter 3, pages 71–111. Wiley-VCH, 2009.

[49] R. Pornprasertsuk, J. Cheng, H. Huang, and F. B. Prinz. Electrochemical impedance analysis of solid oxide fuel cell electrolyte using kinetic Monte Carlo technique. *Solid State Ionics*, 178:195–205, 2007. URL http://www.sciencedirect.com/science/article/pii/S0167273807000045.

[50] Karsten Reuter and Matthias Scheffler. First-principles kinetic Monte Carlo simulations for heterogeneous catalysis: Application to the CO oxidation at $RuO_2(110)$. *Physical Review B*, 73:045433, 2006. URL http://prb.aps.org/abstract/PRB/v73/i4/e045433.

[51] C. C. Battaile, D. J. Srolovitz, and J. E. Butler. A kinetic monte carlo method for the atomic-scale simulation of chemical vapor deposition: Application to diamond. *Journal of Applied Physics*, 82(12):6293–6300, 1997. URL http://jap.aip.org/resource/1/japiau/v82/i12/p6293_s1.

[52] Bernard Diu, Claudine Guthmann, Danielle Lederer, and Bernard Roulet. *Physique statistique*. 1996.

[53] E. P. Wigner. *Z. Phys. Chem. Abt. B*, 19:203, 1932.

[54] H. Eyring. The activated complex in chemical reactions. *Journal of Chemical Physics*, 3:107–115, 1935. URL http://jcp.aip.org/resource/1/jcpsa6/v3/i2/p107_s1.

[55] P. Hänggi, P. Talkner, and M. Borkovec. Reaction-rate theory : fifty years after Kramers. *Reviews of Modern Physics*, 62:251–341, 1990. URL http://adsabs.harvard.edu/abs/1990RvMP...62..251H.

[56] D. Chandler and P. G. Wolynes. Exploiting the isomorphism between quantum theory and classical statistical mechanics of polyatomic fluids. *The Journal of Chemical Physics*, 74(7):4078, 1981. URL http://jcp.aip.org/resource/1/jcpsa6/v74/i7/p4078_s1.

[57] R. P. Feynman. *Statistical Mechanics*, chapter 3. Benjamin, 1972.

[58] R. P. Feynman and A. R. Hibbs. *Quantum Mechanics and Path Integrals*. McGraw-Hill, New York, 1965.

[59] M. E. Tuckerman, D. Marx, M. L. Klein, and M. Parrinello. Efficient and general algorithms for path integral Car–Parrinello molecular dynamics. *The Journal of Chemical Physics*, 104(14):5579–5588, 1996. URL http://link.aip.org/link/?JCP/104/5579/1.

[60] D. Marx and M. Parrinello. Ab initio path integral molecular dynamics: Basic ideas. *The Journal of Chemical Physics*, 104(11):4077–4082, 1996. URL http://link.aip.org/link/?JCP/104/4077/1.

[61] D. M. Ceperley. Path integrals in the theory of condensed helium. *Reviews of Modern Physics*, 67(2):279–355, 1995. URL http://rmp.aps.org/abstract/RMP/v67/i2/p279_1.

[62] B. Chen, I. Ivanov, M. L. Klein, and M. Parrinello. Hydrogen bonding in water. *Physical Review Letters*, 91(21):215503, 2003. URL http://prl.aps.org/abstract/PRL/v91/i21/e215503.

[63] J. A. Morrone and R. Car. Nuclear quantum effects in water. *Physical Review Letters*, 101(1):17801, 2008. URL http://prl.aps.org/abstract/PRL/v101/i1/e017801.

[64] Q. Zhang, G. Wahnström, M. E. Björketun, S. Gao, and E. Wang. Path integral treatment of proton transport processes in $BaZrO_3$. *Physical Review Letters*,

101(21):215902, 2008. URL http://prl.aps.org/abstract/PRL/v101/i21/e215902.

[65] H. F. Trotter. On the product of semi-groups of operators. *Proceedings of the American Mathematical Society*, 10:545–551, 1959. URL http://www.jstor.org/discover/10.2307/2033649?uid=3738016&uid=2&uid=4&sid=21102567986521.

[66] N. Holzwarth, A. Tackett, and G. Matthews. A projector augmented wave (paw) code for electronic structure calculations, part i:AtomPAW for generating atom-centered functions. *Computer Physics Communications*, 135 (3):329–347, 2001. URL http://www.sciencedirect.com/science/article/pii/S0010465500002447.

[67] G. Kresse and J. Hafner. First-principles study of the adsorption of atomic H on Ni (111), (100) and (110). *Surface Science*, 459:287–302, 2000. URL http://www.sciencedirect.com/science/article/pii/S003960280000457X.

[68] D. E. Jiang and E. A. Carter. Diffusion of interstitial hydrogen into and through bcc Fe from first principles. *Physical Review B*, 70:064102, 2004. URL http://prb.aps.org/abstract/PRB/v70/i6/e064102.

[69] K. P. Huber and G. Hertzberg. *Molecular Spectra and Molecular Structure IV: Constants of Diatomic Molecules*. Van Norstrand Reinhold, New York, 1979.

[70] J. Paier, R. Hirschl, M. Marsman, and G. Kresse. The Perdew-Burke-Ernzerhof exchange-correlation functional applied to the G2-1 test set using a plane-wave basis set. *Journal of Chemical Physics*, 122:234102, 2005. URL http://jcp.aip.org/resource/1/jcpsa6/v122/i23/p234102_s1.

[71] B. Amadon, F. Jollet, and M. Torrent. γ and β cerium: LDA+U calculations of ground-state parameters. *Phys. Rev. B*, 77:155104, 2008. URL http://prb.aps.org/abstract/PRB/v77/i15/e155104.

[72] C. Kittel. *Introduction to solid state physics*. Wiley, 7th edition, 1996. URL http://books.google.com/books?id=-wBRAAAAMAAJ.

[73] D. Belger, Z. Hüsges, E. Voloshina, and B. Paulus. The role of electron correlations in the binding properties of Ca, Sr, and Ba. *Journal of Physics: Condensed Matter*, 22(27):275504, 2010. URL http://iopscience.iop.org/0953-8984/22/27/275504/.

[74] F. Jona and P. M. Marcus. Structure of barium in three phases under pressure. *Europhysics Letters*, 74:83, 2006. URL http://iopscience.iop.org/0295-5075/74/1/083.

[75] P. Söderlind, O. Eriksson, B. Johansson, and J. M. Wills. Electronic properties of f -electron metals using the generalized gradient approximation. *Physical Review B*, 50:7291–7294, 1994. URL http://link.aps.org/doi/10.1103/PhysRevB.50.7291.

[76] M. Heinemann and W. M. Temmerman. Magnetic structures of hcp bulk gadolinium. *Physical Review B*, 49(6):4348–4351, 1994. URL http://prb.aps.org/abstract/PRB/v49/i6/p4348_1.

[77] L. Liu and W. A. Bassett. Effect of pressure on the crystal structure and the lattice parameters of BaO. *Journal of Geophysical Research*, 77(26):4934–4937, 1972. URL http://onlinelibrary.wiley.com/doi/10.1029/JB077i026p04934/abstract;jsessionid=38F474C0EF17A56E70C1BABCABA162B3.d02t01?systemMessage=Wiley+Online+Library+will+be+disrupted+on+31+August+from+10%3A00-12%3A00+BST+%2805%3A00-07%3A00+EDT%29+for+essential+maintenance.

[78] S. T. Weir, Y. K. Vohra, and A. L. Ruoff. High-pressure phase transitions and the equations of state of BaS and BaO. *Physical Review B*, 33(6):4221–4226, 1986. URL http://prb.aps.org/abstract/PRB/v33/i6/p4221_1.

[79] R. G. Amorim, M. Veríssimo-Alves, and J. P. Rino. Energetics of phase transitions in BaO through DFT calculations with norm-conserving pseudopotentials: LDA vs. GGA results. *Computational Materials Science*, 37(3):349–354, 2006. URL http://www.sciencedirect.com/science/article/pii/S0927025605002995.

[80] L. Gerward, J. Staun Olsen, L. Petit, G. Vaitheeswaran, V. Kanchana, and A. Svane. Bulk modulus of CeO_2 and PrO_2—an experimental and theoretical study. *Journal of Alloys and Compounds*, 400(1-2):56–61, 2005. URL http://www.sciencedirect.com/science/article/pii/S0925838805003403.

[81] S. Fabris, S. de Gironcoli, S. Baroni, G. Vicario, and G. Balducci. Taming multiple valency with density functionals: A case study of defective ceria. *Physical Review B*, 71(4):041102, 2005. URL http://prb.aps.org/abstract/PRB/v71/i4/e041102.

[82] N. Hirosaki, S. Ogata, and C. Kocer. Ab initio calculation of the crystal structure of the lanthanide Ln_2O_3 sesquioxides. *Journal of Alloys and Compounds*, 351 (1-2):31–34, 2003. URL http://www.sciencedirect.com/science/article/B6TWY-47HC558-5/2/d904ca808c39990365f9d13c7e27d899.

[83] M. Zinkevich. Thermodynamics of rare earth sesquioxides. *Progress in Materials Science*, 52(4):597–647, 2007. URL http://www.sciencedirect.com/science/article/B6TX1-4MD9G0W-1/2/a7cad855b2b8eee88687acf41517733d.

[84] G. Jomard, F. Amadon, B.and Bottin, and M. Torrent. Structural, thermodynamic, and electronic properties of plutonium oxides from first principles. *Physical Review B*, 78:075125, 2008. URL http://link.aps.org/doi/10.1103/PhysRevB.78.075125.

[85] L. Petit, A. Svane, Z. Szotek, and W. M. Temmerman. First-principles study of rare-earth oxides. *Physical Review B*, 72(20):205118, 2005. URL http://prb.aps.org/abstract/PRB/v72/i20/e205118.

[86] R. M. Moon and W. C. Koehler. Magnetic properties of Gd_2O_3. *Physical Review B*, 11(4):1609–1622, 1975. URL http://prb.aps.org/abstract/PRB/v11/i4/p1609_1.

[87] L. Ning, Y. Zhang, Z. Cui, M. I. Trioni, and G. P. Brivio. Density functional theory study of magnetic coupling in the $Gd_{12}O_{18}$ cluster. *The Journal of Physical Chemistry A*, 112(51):13650–13654, 2008. URL http://pubs.acs.org/doi/abs/10.1021/jp807015b.

[88] A. Ayuela, N. H. March, and D. J. Klein. Optimized geometry of the cluster Gd_2O_3 and proposed antiferromagnetic alignment of f-electron magnetic moment. *The Journal of Physical Chemistry A*, 111(40):10162–10165, 2007. URL http://pubs.acs.org/doi/abs/10.1021/jp0745790.

[89] H. Pedersen and L. Ojamäe. Towards biocompatibility of RE_2O_3 nanocrystals - water and organic molecules chemisorbed on Gd_2O_3 and Y_2O_3 nanocrystals studied by quantum-chemical computations. *Nano Letters*, 6(9):2004–2008, 2006. URL http://pubs.acs.org/doi/abs/10.1021/nl061185w.

[90] H. B. Lal and K. Gaur. Electrical conduction in non-metallic rare-earth solids. *Journal of Materials Science*, 23:919–923, 1988. URL http://dx.doi.org/10.1007/BF01153989.

[91] B. Mercier, G. Ledoux, C. Dujardin, D. Nicolas, B. Masenelli, P. Melinon, and G. Bergeret. Quantum confinement effect on gd_2o_3 clusters. *The Journal of Chemical Physics*, 126(4):044507, 2007. URL http://link.aip.org/link/?JCP/126/044507/1.

[92] Bruno Mercier. *PROPRIÉTÉS de LUMINESCENCE et EFFETS de CONFINEMENT dans Gd_2O_3 : Eu^{3+} : Études de Nanocristaux issus de différentes voies de synthèse*. PhD thesis, Universite Claude Bernard - Lyon I, Juillet 2005.

[93] F. Grosse, T. Watahiki, and W. Braun. Rare earth oxide alloys and stacked layers: An ab initio study. *Thin Solid Films*, 518(16):4747–4749, 2010. URL http://www.sciencedirect.com/science/article/B6TW0-4Y1NV12-4/2/a7b0d1287e0890432c0960379cbe663c. Proceedings of the EMRS 2009 Spring Meeting Symposium H: Synthesis, Processing and Characterization of Nanoscale Multi Functional Oxide Films II.

[94] A.V. Prokofiev, A.I. Shelykh, and B.T. Melekh. Periodicity in the band gap variation of Ln_2X_3 (X = O, S, Se) in the lanthanide series. *Journal of Alloys and Compounds*, 242(1-2):41–44, 1996. URL http://www.sciencedirect.com/science/article/B6TWY-3YMWS1X-51/2/03071cfb9386f89161059bb1701aeeb3.

[95] F. X. Zhang, M. Lang, J. W. Wang, U. Becker, and R. C. Ewing. Structural phase transitions of cubic Gd_2O_3 at high pressures. *Physical Review B*, 78(6):064114, 2008. URL http://prb.aps.org/abstract/PRB/v78/i6/e064114.

[96] K.S. Knight. Structural phase transitions, oxygen vacancy ordering and protonation in doped $BaCeO_3$: results from time-of-flight neutron powder diffraction investigations. *Solid State Ionics*, 145(1-4):275–294, 2001. URL http://www.sciencedirect.com/science/article/pii/S0167273801009523. Proceedings of the 10th International Conference on Solid State Protonic Conductors.

[97] A. V. Kuzmin, V. P. Gorelov, B. T. Melekh, M. Glerup, and F. W. Poulsen. Phase transitions in undoped $BaCeO_3$. *Solid State Ionics*, 162-163:13–22, 2003. URL http://www.sciencedirect.com/science/article/pii/S0167273803002479. Proceedings of the Eleventh International Conference on Solid State Protonic Conductors.

[98] Z. Zhang, J. Koppensteiner, W. Schranz, J. B. Betts, A. Migliori, and M. A. Carpenter. Microstructure dynamics in orthorhombic perovskites. *Physical Review*

B, 82:014113, 2010. URL http://link.aps.org/doi/10.1103/PhysRevB.82.014113.

[99] A M Glazer. The classification of tilted octahedra in perovskites. *Acta Crystallographica Section B Structural Crystallography and Crystal Chemistry*, 28(11):3384–3392, 1972. URL http://scripts.iucr.org/cgi-bin/paper?S0567740872007976.

[100] J. Bennett and A. Rappe. First principles modeling of $BaCeO_3$: Stabilization of O vacancies. In *APS Meeting Abstracts*, page 38003, March 2008. URL http://adsabs.harvard.edu/abs/2008APS..MARB38003B.

[101] J. Li, U. G. Singh, J. W. Bennett, K. Page, J. C. Weaver, J.P. Zhang, T. Proffen, A. M. Rappe, S. Scott, and R. Seshadri. $BaCe_{1-x}Pd_xO_{3-\delta}$ ($0 \leq x \leq 0.1$):Redox Controlled Ingress and Egress of Palladium in a Perovskite. *Chemistry of Materials*, 19:1418–1426, 2007. URL http://pubs.acs.org/doi/abs/10.1021/cm062500i.

[102] J. Zhang, Y. Zhao, H. Xu, B. Li, D. J. Weidner, and A. Navrotsky. Elastic properties of yttrium-doped $BaCeO_3$ perovskite. *Applied Physics Letters*, 90 (16):161903, 2007. URL http://dx.doi.org/doi/10.1063/1.2723679.

[103] E. H. P. Cordfunke, A. S. Booij, and M. E. Huntelaar. The thermochemical properties of $BaCeO_3$(s) and $SrCeO_3$(s) from T=(5 to 1500) K. *The Journal of Chemical Thermodynamics*, 30(4):437–447, 1998. URL http://www.sciencedirect.com/science/article/pii/S0021961497903025.

[104] Y. Yuan, J. Zheng, X. Zhang, Z. Li, T. Yu, J. Ye, and Z. Zou. $BaCeO_3$ as a novel photocatalyst with 4f electronic configuration for water splitting. *Solid State Ionics*, 178(33-34):1711–1713, 2008. URL http://www.sciencedirect.com/science/article/pii/S0167273807003530.

[105] M. Shishkin and T. Ziegler. Structural, electronic, stability and reduction properties of perovskites surfaces: The case of rhombohedral $BaCeO_3$. *Surface Science*, 606:1078–1087, 2012. URL http://www.sciencedirect.com/science/article/pii/S0039602812000921.

[106] F. Cordero, F. Trequattrini, F. Deganello, V. La Parola, E. Roncari, and A. Sanson. Effect of doping and oxygen vacancies on the octahedral tilt transitions in the $baceo_3$ perovskite. *Phys. Rev. B*, 82:104102, 2010. URL http://link.aps.org/doi/10.1103/PhysRevB.82.104102.

[107] B.T Melekh, V.M Egorov, Yu.M Baikov, N.F Kartenko, Yu.N Filin, M.E Kompan, I.I Novak, G.B Venus, and V.B Kulik. Structure, phase transitions and optical properties of pure and rare earth doped $BaCeO_3$, $SrCeO_3$ prepared by inductive melting. *Solid State Ionics*, 97(1-4):465–470, 1997. URL http://www.sciencedirect.com/science/article/B6TY4-3SPKWSK-38/2/1e486e3244e93812a41c56fa013be1cf.

[108] M. Khandelwal, A. Venkatasubramanian, T.R.S. Prasanna, and P. Gopalan. Correlation between microstructure and electrical conductivity in composite electrolytes containing Gd-doped ceria and Gd-doped barium cerate. *Journal of the European Ceramic Society*, 31(4):559–568, 2011. URL http://www.sciencedirect.com/science/article/pii/S0955221910004954.

[109] R. D. Shannon. Revised effective ionic radii and systematic studies of interatomic distances in halides and chalcogenides. *Acta Crystallographica Section A*, 32(5):751–767, 1976. URL http://dx.doi.org/10.1107/S0567739476001551.

[110] E. Gorbova, V. Maragou, D. Medvedev, A. Demin, and P. Tsiakaras. Influence of sintering additives of transition metals on the properties of gadolinium-doped barium cerate. *Solid State Ionics*, 179(21-26):887–890, 2008. URL http://www.sciencedirect.com/science/article/B6TY4-4SK4X6X-1/2/e9576cf9984d9ae56def4f629b127d5e. Solid State Ionics 16: Proceedings of the 16th International Conference on Solid State Ionics (SSI-16), Part I.

[111] K.D. Kreuer, A. Fuchs, and J. Maier. HD isotope effect of proton conductivity and proton conduction mechanism in oxides. *Solid State Ionics*, 77(0):157–162, 1995. URL http://www.sciencedirect.com/science/article/pii/016727389400265T.

[112] C.R.A. Cherry, M. Islam, M.S. Gale, and J.D. Catlow. Computational studies of protons in perovskite-structured oxides. *Journal of Physical Chemistry*, 99(40):14614–14618, 1995. URL http://pubs.acs.org/doi/abs/10.1021/j100040a007.

[113] E. Matsushita and T. Sasaki. Theoretical approach for protonic conduction in perovskite-type oxides. *Solid State Ionics*, 125(1-4):31–37, 1999. URL http://www.sciencedirect.com/science/article/pii/S0167273899001551.

[114] R. Glöckner, M.S. Islam, and T. Norby. Protons and other defects in $BaCeO_3$: a computational study. *Solid State Ionics*, 122(1-4):145–156, 1999. URL http://www.sciencedirect.com/science/article/pii/S0167273899000703.

[115] T. Tauer, R. O'Hayre, and J. W. Medlin. A theoretical study of the influence of dopant concentration on the hydration properties of yttrium-doped barium cerate. *Solid State Ionics*, 204–205:27–34, 2011. URL http://www.sciencedirect.com/science/article/pii/S0167273811005029.

[116] R. Hempelmann. Hydrogen diffusion mechanism in proton conducting oxides. *Physica B: Condensed Matter*, 226:72–77, 1996. URL http://www.sciencedirect.com/science/article/pii/0921452696002517.

[117] Y. Yamazaki, F. Blanc, Y. Okuyama, L. Buannic, J. C. Lucio-Vega, C. P. Grey, and S. M. Haile. Proton trapping in yttrium-doped barium zirconate. *Nature Materials*, 12:647–651, 2013. URL http://www.nature.com/nmat/journal/v12/n7/abs/nmat3638.html.

[118] K.D. Kreuer. On the development of proton conducting materials for technological applications. *Solid State Ionics*, 97(1-4):1–15, 1997. URL http://www.sciencedirect.com/science/article/B6TY4-3SPKWSK-13/2/a5173aa7ca1a7eb8e89162538746749d.

[119] Y. Yamazaki, C.K. Yang, and S. M. Haile. Unraveling the defect chemistry and proton uptake of yttrium-doped barium zirconate. *Scripta Materialia*, 65 (2):102–107, 2011. URL http://www.sciencedirect.com/science/article/pii/S135964621000864X.

[120] É. Bévillon, G. Dezanneau, and G. Geneste. Oxygen incorporation in acceptor-doped perovskites. *Physical Review B*, 83(17):174101, 2011. URL http://prb.aps.org/abstract/PRB/v83/i17/e174101.

[121] D.K. Lim, M.B. Choi, K.T. Lee, H.S. Yoon, E. D. Wachsman, and S.J. Song. Non-monotonic conductivity relaxation of proton-conducting $BaCe_{0.85}Y_{0.15}O_3$ upon hydration and dehydration. *International Journal of Hydrogen Energy*, 36: 9367–9373, 2011. URL http://www.sciencedirect.com/science/article/pii/S0360319911011001.

[122] A. Grimaud, J.-M. Bassat, F. Mauvy, P. Simon, A. Canizares, B. Rousseau, M. Marrony, and J.-C. Grenier. Transport properties and in-situ raman spectroscopy of $BaCe_{0.9}Y_{0.1}O_{3-\delta}$ as a function of water partial pressures. *Solid State Ionics*, 191:24–31, 2011. URL http://www.sciencedirect.com/science/article/pii/S0167273811001767.

[123] S.-J. Song, E. D. Wachsman, S. E. Dorris, and U. Balachandran. Defect chemistry modeling of high-temperature proton-conducting cerates. *Solid*

State Ionics, 149:1–10, 2002. URL http://www.sciencedirect.com/science/article/pii/S0167273802001479.

[124] D. R. Lick. *CRC Handbook of Chemistry and Physics, 85th edition*, 2004-2005.

[125] B. Merinov and W. Goddard III. Proton diffusion pathways and rates in Y-doped $BaZrO_{sub3}$ solid oxide electrolyte from quantum mechanics. *The Journal of Chemical Physics*, 130(19):194707, 2009. URL http://link.aip.org/link/?JCP/130/194707/1.

[126] K. Rasim. *Conductivité protonique et structures locales par simulations ab initio d'oxydes utilisés comme électrolyte dans les piles à combustibles*. PhD thesis, Université de Nantes, Mars 2011.

[127] W. Münch, G. Seifert, K.D. Kreuer, and J. Maier. A quantum molecular dynamics study of proton conduction phenomena in $BaCeO_3$. *Solid State Ionics*, 86-88, Part 1:647–652, 1996. URL http://www.sciencedirect.com/science/article/pii/0167273896002299.

[128] M. Cherry, M.S. Islam, and C.R.A. Catlow. Oxygen ion migration in perovskite-type oxides. *Journal of Solid State Chemistry*, 118(1):125 – 132, 1995. URL http://www.sciencedirect.com/science/article/pii/S0022459685713205.

[129] M. S. Khan, M. S. Islam, and D. R. Bates. Dopant substitution and ion migration in the $LaGaO_3$-based oxygen ion conductor. *The Journal of Physical Chemistry B*, 102(17):3099–3104, 1998. URL http://pubs.acs.org/doi/abs/10.1021/jp972819d.

[130] M.W. Ammann, J.P. Brodholt, and D.P. Dobson. DFT study of migration enthalpies in $MgSiO_3$ perovskite. *Physics and Chemistry of Minerals*, 36(3):151–158, 2009. URL http://link.springer.com/article/10.1007/s00269-008-0265-z.

[131] V. Barone and C. Adamo. Proton transfer in the ground and lowest excited States of malonaldehyde: A comparative density functional and post-Hartree-Fock study. *Journal of Chemical Physics*, 105(24):11007–11019, 1996. URL http://jcp.aip.org/resource/1/jcpsa6/v105/i24/p11007_s1.

[132] A. Bilić and J. D. Gale. Simulation of proton diffusion in In-doped $CaZrO_3$. *Solid State Ionics*, 179(21–26):871–874, 2008. URL http://www.sciencedirect.com/science/article/pii/S0167273808000957.

[133] M. E. Björketun, P. G. Sundell, and G. Wahnström. Effect of acceptor dopants on the proton mobility in $BaZrO_3$: A density functional investigation. *Physical Review B*, 76(5):054307, 2007. URL http://prb.aps.org/abstract/PRB/v76/i5/e054307.

[134] É. Bévillon, J. Hermet, G. Dezanneau, and G. Geneste. How dopant size influences the protonic energy surface in acceptor-doped barium stannate. *submitted to Journal of Materials Chemistry A*, 2013.

[135] W. Münch, G. Seifert, K.D. Kreuer, and J. Maier. A quantum molecular dynamics study of the cubic phase of $BaTiO_3$ and $BaZrO_3$. *Solid State Ionics*, 97 (1–4):39–44, 1997. URL http://www.sciencedirect.com/science/article/pii/S0167273897000854.

[136] R. P. Bell. The theory of reactions involving proton transfers. *Proceedings of The Royral Society A*, 154:414–429, 1936. URL http://www.jstor.org/discover/10.2307/96510?uid=3738016&uid=2&uid=4&sid=21102568421751.

[137] M. G. Evans and M. Polanyi. Inertia and driving force of chemical reactions. *Transactions of the faraday society*, 34:11–24, 1938. URL http://pubs.rsc.org/en/content/articlelanding/1938/tf/tf9383400011/unauth.

[138] X. Gonze. First-principles responses of solids to atomic displacements and homogeneous electric fields: Implementation of a conjugate-gradient algorithm. *Physical Review B*, 55:10337–10354, 1997. URL http://link.aps.org/doi/10.1103/PhysRevB.55.10337.

[139] X. Gonze and C. Lee. Dynamical matrices, Born effective charges, dielectric permittivity tensors, and interatomic force constants from density-functional perturbation theory. *Physical Review B*, 55:10355–10368, 1997. URL http://link.aps.org/doi/10.1103/PhysRevB.55.10355.

[140] N. Bork, N. Bonanos, J. Rossmeisl, and T. Vegge. Simple descriptors for proton-conducting perovskites from density functional theory. *Physical Review B*, 82: 014103, 2010. URL http://prb.aps.org/abstract/PRB/v82/i1/e014103.

[141] N. Bork, N. Bonanos, J. Rossmeisl, and T. Vegge. Thermodynamic and kinetic properties of hydrogen defect pairs in $SrTiO_3$ from density functional theory. *Phys. Chem. Chem. Phys.*, 13:15256–15263, 2011. URL http://pubs.rsc.org/en/Content/ArticleLanding/2011/CP/c1cp20406h.

[142] N. Bonanos, B. Ellis, K.S. Knight, and M.N. Mahmood. Ionic conductivity of gadolinium-doped barium cerate perovskites. *Solid State Ionics*, 35:179–188, 1989. URL http://www.sciencedirect.com/science/article/pii/0167273889900283.

[143] K.D. Kreuer, E. Schönherr, and J. Maier. Proton and oxygen diffusion in $BaCeO_3$ based compounds: A combined thermal gravimetric analysis and conductivity study. *Solid State Ionics*, 70–71, Part 1(0):278–284, 1994. URL http://www.sciencedirect.com/science/article/pii/0167273894903239.

[144] A. U. Modak and M. T. Lusk. Kinetic Monte Carlo simulation of a solid-oxide fuel cell: I. Open-circuit voltage and double layer structure. *Solid State Ionics*, 176:2181–2191, 2005. URL http://www.sciencedirect.com/science/article/pii/S0167273805002614.

[145] H. Iwahara, T. Mori, and T. Hibino. Electrochemical studies on ionic conduction in Ca-doped $BaCeO_3$. *Solid State Ionics*, 79:177–182, 1995. URL http://www.sciencedirect.com/science/article/pii/016727389500058E. Proceedings of the 20th Commemorative Symposium on Solid State Ionics in Japan.

[146] M. Oishi, S. Akoshima, K. Yashiro, K. Sato, J. Mizukashi, and T. Kawada. Defect structure analysis of B-site doped perovskite-type proton conducting oxide $BaCeO_3$ Part 2: The electrical conductivity and diffusion coefficient of $BaCe_{0.9}Y_{0.1}O_{3-\delta}$. *Solid State Ionics*, 179:2240–2247, 2008. URL http://www.sciencedirect.com/science/article/pii/S0167273813002907.

[147] Grégory Geneste, Marc Torrent, Fran çois Bottin, and Paul Loubeyre. Strong isotope effect in phase ii of dense solid hydrogen and deuterium. *Phys. Rev. Lett.*, 109:155303, Oct 2012. doi: 10.1103/PhysRevLett.109.155303. URL http://link.aps.org/doi/10.1103/PhysRevLett.109.155303.

[148] Slowinski Stanitski Masterton. *Chemical Principles*. CBC College Publishing, 1983.

[149] L. V. Gurvich. *Thermodynamic Properties of Individual Substances*, volume vols. 1-4. Nauka, Moskow, 1982-1987.

[150] N. I. Matskevich and T. A. Wolf. The enthalpies of formation of $BaCe_{1-x}RE_xO_{3-\delta}$ (RE = Eu, Tb, Gd). *The Journal of Chemical Thermodynamics*, 42(2):225–228, 2010. URL http://www.sciencedirect.com/science/article/pii/S0021961409002055.

Contents

Index